Study of the bifurcation behavior of the flow around a 2D Ahmed body applied to active flow control systems

O. Crespo

Technische Universiteit Delft

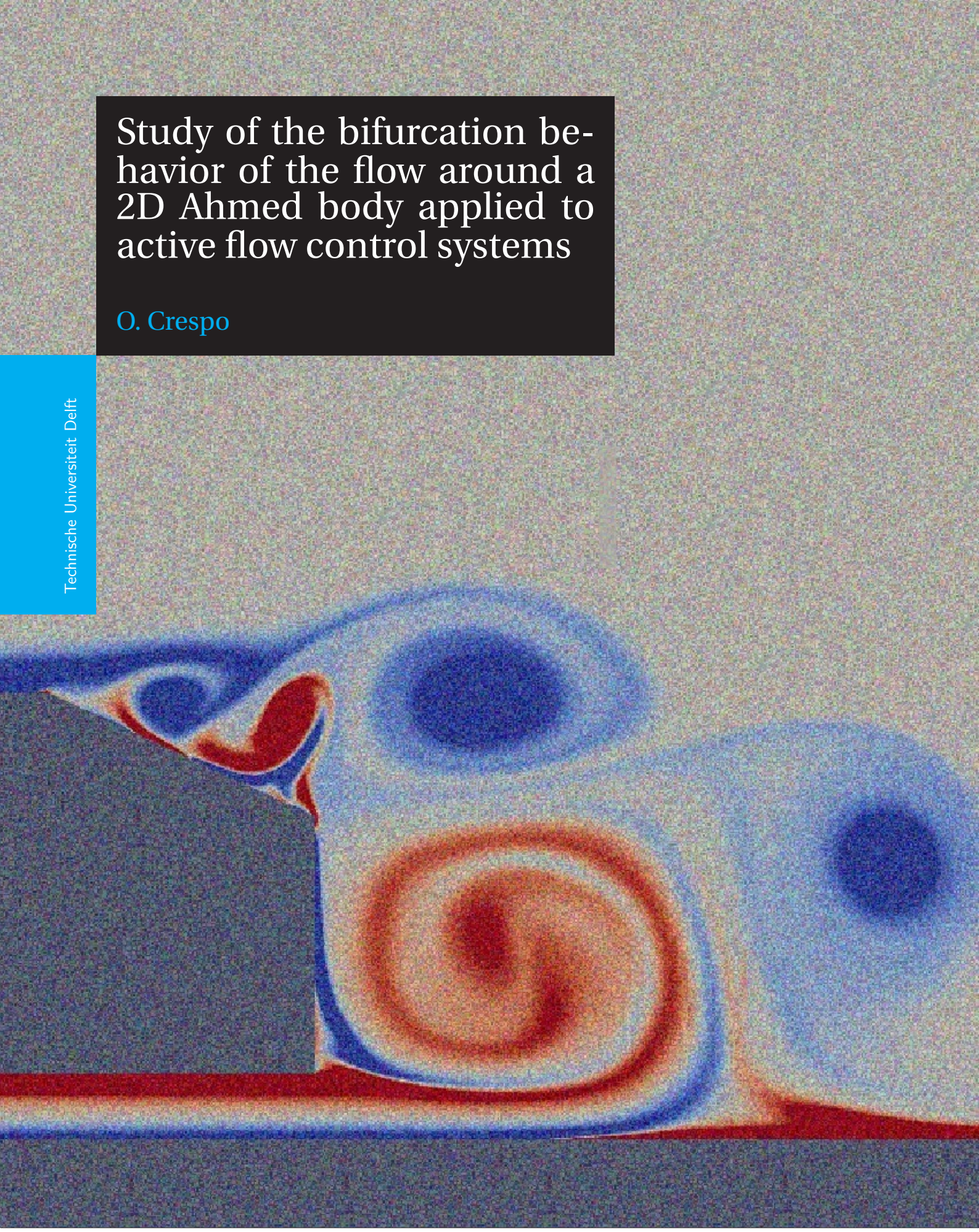

TU Delft Delft University of Technology

Challenge the future

STUDY OF THE BIFURCATION BEHAVIOR OF THE FLOW AROUND A 2D AHMED BODY APPLIED TO ACTIVE FLOW CONTROL SYSTEMS

by

O. Crespo

to obtain the degree of Master of Science in Aerodynamics
at the Delft University of Technology,
to be defended publicly on Thursday March 29, 2018 at 1:30 PM.

Student number:	4513975	
Project duration:	June 20, 2017 – March 29, 2018	
Thesis committee:	Prof. dr. ir. B. W. van Oudheusden	TU Delft, supervisor
	Prof. dr. ir. A. W. van Zuijlen	TU Delft
	Prof. dr. ir. C. Simao Ferreira	TU Delft
	Prof. dr. F. Mellibovsky	UPC, supervisor

An electronic version of this thesis is available at `http://repository.tudelft.nl/`.

TU Delft Delft University of Technology

LIST OF ABBREVIATIONS

Abbreviation	Meaning
2D	two-dimensional
3D	three-dimensional
ALD	Attached Low Drag
BC	Boundary Conditions
CFL	Courant–Friedrichs–Lewy condition
c-pilar	Rear window pillar of a sedan-like vehicle
HD	High Drag
MSc	Master of Science
NS	Navier-Stokes
NVS	Natural vortex shedding
RSB	Reflectional Symmetry Breaking
RSP	Reflectional Symmetry Preserving
SLD	Separated Low Drag
SS	Steady state
SW	Standing Wave
TU Delft	Technische Universiteit Delft
UPC	Universitat Politècnica de Catalunya

LIST OF SYMBOLS

Symbol	Meaning
ϵ	Perturbation
λ	Eigensolution of the system
μ	Dynamic viscosity
ν	Kinematic viscosity
ρ	density
τ	Characteristic time scale
ϕ	Slant angle
ω	Angular frequency
A	Area
C_μ	Jet momentum coefficient
C_D	Drag coefficient
C_L	Lift coefficient
C_p	Pressure coefficient
C_v	Vortex drag coefficient
C^*	Ground clearance $C^* = h/H$
D	Diameter
A_R	Aspect ratio $A_R = W/H$
f	Frequency
f_{Str}	Natural vortex shedding frequency
f_{AFC}	Actuation frequency
$\tilde{f}$	Non dimensional frequency $\tilde{f} = f/f_{Str}$
h	Model height from groud
H	Height of the model
H_1	Height of the top boundary condition
L	Length
L_1	Inlet distance
L_2	Outlet distance
p	Pressure
P_{order}	Polynomial order of expansion
Re	Reynolds number
r	radial distance
St	Strouhal number
t	Time
$\mathbf{u}$	Velocity
u	x axis velocity
v	y axis velocity
w	z axis velocity
W	Width of the model
x^*	Fixed point solution
y^+	Non-dimensional wall distance

ACKNOWLEDGMENTS

Two and a half years have already passed and I am approaching the end of my student life. Looking back, i can only say that choosing Delft was an excellent decision both from the academic and personal points of view. For this reason I want to thank all the people that I have met during this period which I have enjoyed so much, and for how much I have had the opportunity to learn. But even more specially I would like to thank all the people that have helped me during this project, both personally and academically.

First of all I would like to thank professor Fernando Mellibovsky for accepting me as his student in Universitat Politècnica de Catalunya. He has been a fantastic supervisor, offered me the opportunity to learn from his experience and introduced me to a field in which I had no prior knowledge. Thank you for everything you have taught me during these months, thank you for your patience, and above all, thank you for your generosity, without you this project would have not been possible.

Secondly, I would like to thank professor Bas van Oudheusden for giving me the opportunity to perform this project under his supervision from TU Delft, his constant support, and his sincere opinions on my work. Thank you for supporting this project, thank you for your comments, and thank you for guiding me when distance was an issue.

Third I want to thank my father Daniel, and my mother Trinitat for all the support that they have given me during all my life. My studies in Delft would never have been possible without them, and having me back in Barcelona has not been easy for them. Thank you for your patience, thank you for your support and thank you for your unconditional love.

I would also like to thank my girlfriend, Mònica, for helping me in the difficult times in which I was worried or doubtful of my capabilities. She has always tried to cheer me up, and that is something priceless. Thank you for everything you have done for me.

I would also like to thank the physics department of Universitat Politècnica de Catalunya in campus nord for allowing me to develop this thesis in their facilities, but also and more specially for welcoming me in their group, and counting me as one more. Thank you for being so kind to me, and sorry for stealing your sitting places, our conversations were a most welcome and interesting break.

Finally, i would like to thank Anna Ramolini and Víctor de la Mora for sharing with me this wonderful experience in Delft with me. Thank you Anna for being my best friend and for sharing everything, i don't think I would have been able to finish this Master or this thesis without you. Thank you Víctor, for taking the challenge of going to Delft together and for all the great times we have shared in Rijswijk and Delft.

O. Crespo
Delft, February 2018

ABSTRACT

The transitional regime is possibly the least known of all three possible types of flow regimes, being laminar and turbulent the most common flow states. This can be due to the fact that it is constrained to a small range of Reynolds numbers, it is not usually found in industrial applications and it exhibits dynamics that can drastically change with small variations of Reynolds or other relevant quantities. In the transitional regime the flow fields transition from an ordered state to a non-periodic (chaotic) unordered state. The study of this regime makes use of specific tools that were developed in the field of stability analysis. The transitional regime is interesting because it shares some features with the turbulent regime, especially in the case of bluff body wakes, and can be fully understood. This type of wakes are dominated by a periodic shedding of vortices and are particularly interesting due to the wide range of industrial applications in which they can be observed (automotive, architecture, etc.).

In this master thesis the study of bluff body wakes in the automotive field is proposed. With this purpose the study of the Ahmed body (a paradigmatic case of bluff body wake applied to the automotive field) is selected. In the study of this problem the focus is usually put in drag reduction at high Reynolds numbers, which is the main goal in industrial applications. With this goal in mind, active flow control systems have been successfully applied both in the case of periodic excitation and constant suction. However, the exact mechanisms by which this drag reduction is achieved in the case of periodic actuation are somewhat unclear, and several explanations exist. Furthermore, it is unclear which actuation frequencies are best, and two methodologies are often used: actuation at frequencies of the order of the vortex shedding frequency and actuation at frequencies one order above. Both methodologies produce good results, and drag reductions of up to 15% can be obtained.

Stability studies usually require to perform a large number of simulations in which a parameter is varied until its relevant values are found. Additionally, modeling of the turbulent scales cannot be applied as in the transitional regime it would contaminate the results. For this reason a direct numerical simulation of all the relevant scales is proposed. Unfortunately the cost of performing such computations on a 3D domain is not possible, and for this reason a 2D approach is proposed. Since the centerline region of the wake in the 3D case presents a mostly 2D topology, some similarities to the 3D case are expected.

In this work the the study of the transitional regime of the Ahmed body problem was performed. A first model was designed which shows an early separation on the front region, which prevents active flow control. Furthermore, the overall wake topology does not resemble the higher Reynolds 3D cases. For this reason a second model was designed.

The second model features a constant suction that prevents the early separation of the boundary layer at the front part of the roof. In this model, destabilization of the wake occurs through a period doubling cascade. When further increasing the Reynolds number the solution re-stabilizes into a periodic flow field of period 2. This behavior supports the period doubling cascade hypothesis, as it is also observed in other period doubling cascades such as the logistic map. From the study of this model 2 characteristic frequencies were selected for application in active flow control: the vortex shedding frequency and one half of this frequency. Additionally, two more frequencies were selected: twice the vortex shedding frequency, and a non harmonic multiple of the vortex shedding frequency.

In the last part of this thesis the study of the application of AFC at three actuation frequencies ($0.5 \times f_{Str}$, f_{Str}, $2 \times f_{Str}$) in the transitional regime is presented. Results show that actuation at frequencies that are lower than the natural vortex shedding frequency fail to resonate with the flow natural instabilities, while those equal or greater than the natural vortex shedding frequencies are successful. When actuation is successful, new types of periodic solutions and large drag reductions can be observed. However, this also produces the effect of greatly increasing lift, which is in general not desirable. Drag reduction with this type of actuation is comparable to constant suction, but without requiring a constant mass flux, which is a clear advantage. The study of the new types of solutions allowed to determine two key properties: first of all, drag is associated to the rear base vortex frequency; second, the periodic solutions are generated when the top and bottom vortices become frequency locked and are destroyed through period doubling cascades. Actuation is therefore observed to produce changes to the flow that accelerate vortex shedding, reducing the intensity of the shed vortices and showing lower drag.

LIST OF FIGURES

CONTENTS

1

INTRODUCTION

The first goal of this thesis is to study the stability of the different flow states present in the transitional regime of the Ahmed body problem. The second goal of this thesis is to determine the impact of Active Flow Control (AFC) on the stability of the different flow states that have been observed.

The study of the problem will be performed using DNS with the spectral elements code Nektar++. This project is possible thanks to the collaboration between TU Delft and Universitat Politècnica de Catalunya (UPC) and will be supervised by both universities. This project will be performed in the UPC facilities under the supervision of the Physics department and evaluated by the Aerodynamics department of TU Delft.

1.1. CONTEXT

Most ground transportation vehicles cannot be exclusively designed under aerodynamic considerations and therefore exhibit bluff body wakes. To study the bluff body wakes of ground transportation-like vehicles Ahmed [3] proposed the Ahmed body geometry. It features a front region where the wake remains attached to the body and a rear region where the wake separates as it would in a bluff body. The Ahmed body geometry is always studied in presence of ground effects. Ground clearance (C^*) is defined as:

$$C^* = \frac{h}{H} \tag{1.1}$$

The rear region presents a slant angle that was varied from 0 degrees to 35 degrees [3]. Three configurations of the Ahmed body have become common in literature:

- Square Ahmed $\phi = 0°$
- $\phi = 25°$
- $\phi = 35°$

The reasoning behind the choice of these angles can be due to two main considerations. On the one hand, these angles are appropriate for the study of the wake topology. On the other hand, it could be related to the fact that most of the current automobiles have adopted these angles. A diagram of the Ahmed body is presented in Figure 1.1.

This geometry has become a paradigmatic case of the study of bluff body wakes, especially at high Reynolds, and is usually studied for two slant angles: $\phi = 25$ deg or $\phi = 35$ deg. In this study the slant angle of study will correspond to $\phi = 25$ deg. The study of this model by Lienhart [4] showed that three different types of wake states can be experimentally observed. The type of wake state that can be observed is mostly dependent on the slant angle and Reynolds number at which the problem is simulated.

1.1.1. AHMED BODY WAKE TOPOLOGY

This section is an overview of the most relevant flow features of the Ahmed body geometry which have been observed. Most of the drag of the vehicle is associated to the separated wake: according to [2] the contribution of the rear wake to the total drag typically exceeds 60%. The Ahmed body wake can present three main wake

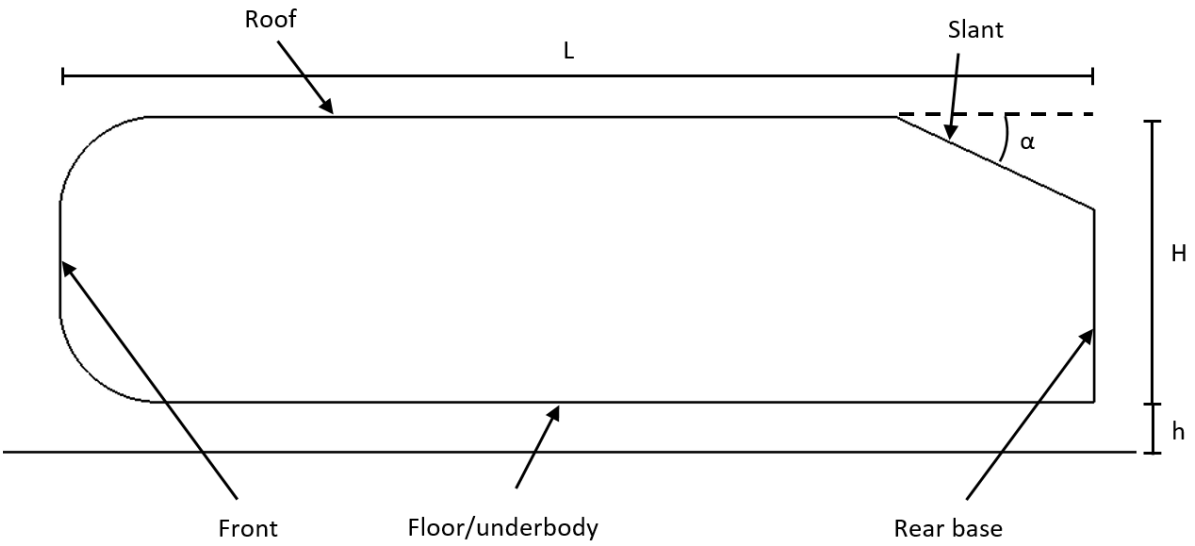

Figure 1.1: Ahmed body geometry for a slant angle of 25 deg

states: attached wake, partially separated wake and fully separated wake. These states are interesting because they present very different types of flow features and global forces.

1. Attached wake:
   The flow follows follows the Ahmed body contour as if it were a streamlined body. Drag contribution of the slant region is low due to the fact that it is mainly determined by friction. At the end of the slant the flow separates, and vortex shedding occurs at the rear base only. This is an extreme case that can be referred to as the Attached Low Drag scenario (ALD). It is the scenario that presents lowest drag.

2. Partially separated wake:
   In this case the wake separates but reattaches at some point over the slant. A recirculation bubble is generated immediately next to the slant, the size of which is determined by the distance between the start of the slant and the reattachment point. The larger this bubble is the larger the drag contribution of the slant will be. This case can present the highest drag of the three scenarios if the separation bubble is large. This case can be referred to as the High Drag scenario (HD). Streamlines of this state are shown in Figure 1.2a.

3. Fully separated wake:
   In this case the wake separates at the start of the slant and never reattaches (the separation bubble bursts). Vortex shedding occurs at the start of the slant and the vortices are directly shed into the wake. This case presents higher drag than the first scenario, since a pressure drag contribution is added. This case can be referred to as the Separated Low Drag scenario (SLD). Streamlines of this state are shown in Figure 1.2b

The Ahmed body presents a sharp edge at the start of the slant, forcing in general the wake to separate. It is therefore difficult to observe a flow such as the one described in the ALD scenario. In 3D simulations this scenario can be observed for low slant angles as it is favored by the slant side vortices (which induce a vertical negative velocity on the slant), however in 2D this scenario is very uncommon.

On the other hand the SLD scenario is also not common in general due to the interaction of the unsteady vortices that are being shed from the bottom of the Ahmed body rear base. Therefore it is more common to observe partial reattachments of the boundary layer on the slant during the vortex shedding process. Therefore the high drag scenario occurs frequently during the vortex shedding process.

To improve the Ahmed body performance it is therefore crucial to modify the vortex shedding process. In this work the geometry is assumed to be fixed, and flow control is achieved through suction or blowing (active flow control).

The three different wake states present clearly different drag values (see Figure 1.3). The lowest drag scenario is the ALD (B in the figure), its drag being 15% lower than the SLD scenario. The HD scenario is 30% higher than the ALD scenario.

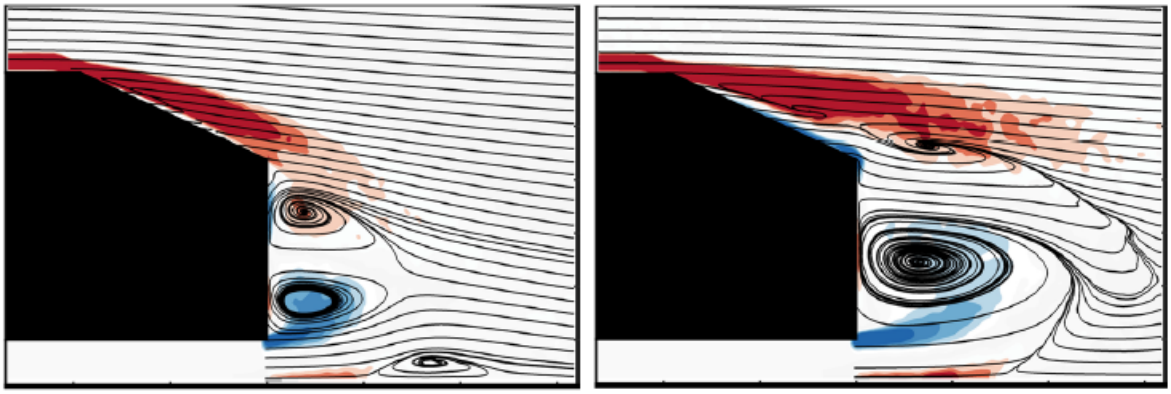

(a) Wake in the centerline for the HD configuration (b) Wake in the centerline for the SLD configuration

Figure 1.2: Comparison of the wake on the center-plane. Figures reproduced from [2]

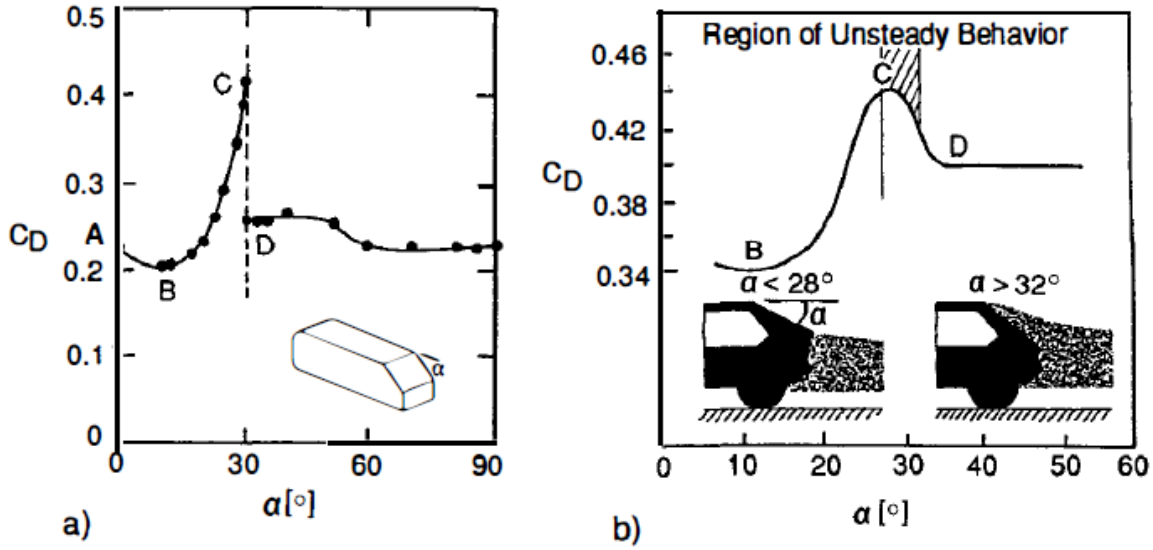

Figure 1.3: Drag coefficient as a function of the slant angle. Figure reproduced from [1]

3D EFFECTS

Although the flow in the center region of the slant is mostly 2-D, the three dimensional nature of the wake cannot be neglected. Venning [2] tested different aspect ratios and determined that increasing the aspect ratio had the same effect on the mid-section of the wake as increasing the slant angle (see Figure 1.4). This behavior can be explained under the following reasoning: as the aspect ratio increases so does the distance from the center-line to the c pillar vortices. These vortices are responsible for the reattachment of the wake in the center-line. If the vortices are at a larger distance, then the induced velocity at the center-line is reduced ($u_{induced} \propto 1/r$).

One of the most interesting conclusions that can be obtained from this article is that the wake topology on the center plane shares a common topology with different aspect ratios. Low aspect ratio bodies will present reattachment on the rear slant more easily than high aspect ratio bodies, but the destabilization of the wake follows the same path: first the wake will partially separate, producing a separation bubble, then the flow will completely separate at the start of the slant.

The reason for this similarity is that the flow on the center region of the slant is mostly 2-dimensional. This can be observed both in Figure 3.8 (velocity contours and separation regions). The reader can clearly observe that wake influence is very strong at the edges $0.8 < |y/W| < 1$, but much smaller in the center region.

In this project the simulations that are performed are 2-D to reduce the computational cost, as many simulations have to be run for long time intervals. The validity of the results is limited to the center region of the body and will fail to represent the effect of the lateral vortices. 3D simulations can be proposed as future

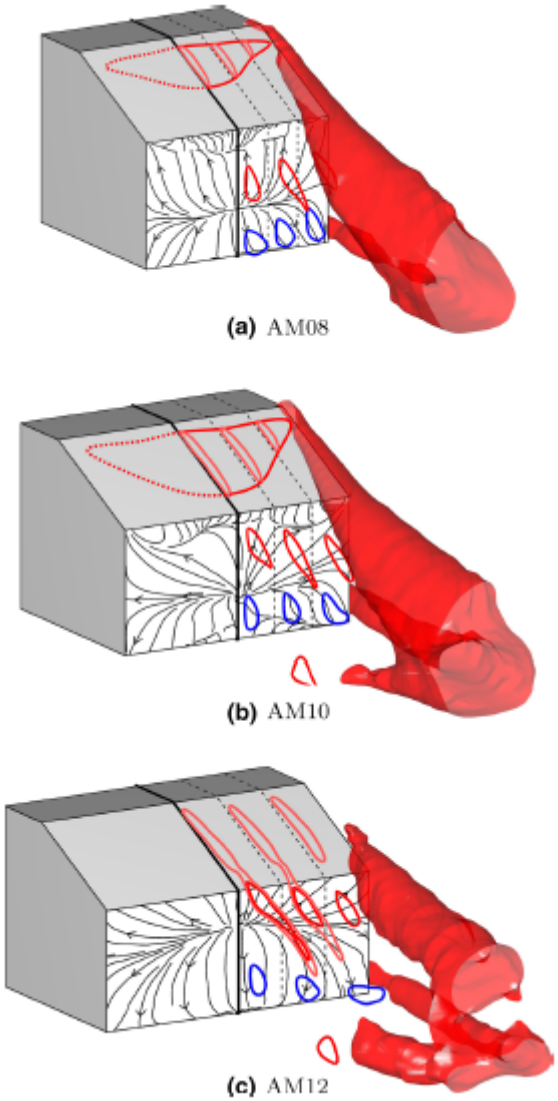

Figure 1.4: Wake profiles for increasing aspect ratios. Figure reproduced from [2]

work, but larger computational resources would be required.

The contribution of the wake of a bluff body to the total drag is usually higher than 60% [2]. Therefore, the reduction of the wake can lead to large reductions of the drag coefficient of the order of 15% by active flow control [5], [6] and up to 25% by passive flow control. Recently active flow control has received great attention as it can avoid some of the inconveniences passive flow control struggles against (aesthetics, increased model size, etc.) However, active flow control requires a great understanding of the flow to produce optimal results.

1.1.2. DRAG REDUCTION STRATEGIES

Drag reduction strategies in general target to modify the vortex shedding process in such a way that drag is reduced. Drag is selected as the most relevant quantity because it is the most important factor that affects road vehicle performance (reduction of consumption is currently a major target in industry). [1] The goal of this study is not to simply study the improvements in performance of the vehicle, but instead to determine how the flow has been altered. However it would not be wise to disregard the performance. In fact, having an indicator of which flow states are more desirable is a good way of focusing the study. Additionally most of the relevant literature is focused towards this goal, which allows for a better comparison.

Vortex shedding can be described as a periodic behavior of the flow on the rear region of a bluff body. In the case of the Ahmed body this behavior is asymmetric, as the geometry is not symmetric. In the slant region the flow separates and reattaches periodically. This generates a vorticity that is shed to the flow. At the bottom region the behavior is also periodic, as the flow is fully separated at the 90º corner. The general wake dynamics is greatly determined by this phenomenon starting from the first flow instabilities to the highly turbulent behavior.

3 main drag reduction strategies have been described in literature for the Ahmed body: vortex shedding suppression, vortex pushing and vortex synchronization.

1. Vortex shedding suppression:
   The separation bubble is eliminated, therefore increasing the static pressure at the wall. Pressure drag can be computed as the difference between the front contribution and the rear contribution $D = \int_\Gamma P ds = |\int_{\Gamma front} P_{front} ds| - |\int_{\Gamma rear} P_{front} ds|$. This has been achieved by several authors such as Auburn [7], Tounsi [8], among many others.

2. Vortex pushing:
   The separated recirculation bubble or shed vortices are pushed away from the wall. By pushing the vortices away the induced velocity on the surface has less impact on the near wall velocity field. This leads to an increase on the static pressure. This has been achieved by Barsotti [9], Aider [10] or [11].

3. Vortex synchronization:
   The top and bottom vortices are forced to shed in a synchronous fashion. When this occurs, the size of the shed vortices is reduced to one half, which reduces the induced velocity at the wall and increases base pressure. This has been achieved by Pastoor [5], but in the case of a square Ahmed body.

These strategies try to explain the main relation between drag reduction and wake topology. In practice it is complicated to obtain one of the cases, instead the reduction can be explained as a combination of these effects.

1.1.3. APPLICATION OF ACTIVE FLOW CONTROL (AFC)

When analyzing the performance of active flow control systems the jet momentum coefficient C_μ is the most used non-dimensional quantity. Most active flow control systems have a linear behavior from 0 actuation to the saturation point, after which increasing C_μ does not produce any improvement in the performance of the control system. C_μ is usually defined as:

$$C_\mu = \frac{\bar{I}_j}{\frac{1}{2}\rho_0 u_0^2 A_0} \tag{1.2}$$

Where ρ_0 and u_0 are the free-stream conditions, A_0 the reference height $\bar{I}_j$ is the time averaged momentum:

[1] However the lift balance of the vehicle can also be a key aspect in the performance of the vehicle, especially in the area of racing.

$$\bar{I_j} = \frac{1}{\tau}\rho_{AFC} A_{AFC} \int_0^\tau u_j^2(t) dt \tag{1.3}$$

Since the jet fluid is the same as the free-stream fluid, $\rho_{AFC} = \rho_0$, A_{AFC} is the actuation length and the velocity profile depends on the type of actuation.

To characterize active flow control through periodic excitation the Strouhal number is also used. It describes the non-dimensional frequency of a certain phenomena or actuation.

$$Str = \frac{fH}{U_0} \tag{1.4}$$

There are two main strategies in the application of AFC: flow control using a frequency of the order of the natural vortex shedding frequency and flow control using a frequency that is much larger than the that of the vortex shedding. Examples in literature include: Kourta [12], who studied actuation at frequencies of the order of 1 to 8 times the natural vortex shedding frequency, Bruneau [13] who studied actuation at half the natural vortex shedding frequency or [14] who did the same but at much larger frequencies. In this project the first strategy has been selected. The goal is to force the solution to bifurcate to a new flow state. It is assumed that it is more likely that the flow can adapt to a new solution that has a periodicity of the same order as the natural frequency of the problem than if the forcing frequency is an order of magnitude larger. On the other hand, however, high frequency excitation of the flow has also been used effectively to trigger new flow states and reduce drag. This strategy can be studied in future work.

1.1.4. REQUIREMENTS

In order to successfully implement active flow control, it should be implemented on an attached boundary layer on the verge of separation. Locating the separation point on streamlined bodies can be a challenge, however in the case of bluff bodies it is usually determined by a sharp edge. For this reason the actuation locations on the Ahmed body are limited. The most common actuation point by far is on the roof immediately before the start of the slant. Alternatively the lower part of the rear surface has also been proposed, but has been studied to a lower extent. In this study the first option has been chosen as it is the "standard" in AFC studies on the Ahmed body.

1.2. SIMULATION AND ANALYSIS OF THE MODEL

The equations that govern the motion of fluids are the Navier-Stokes equations. This set of non-linear differential equations cannot be solved analytically for most of the cases of interest. However they allow for two main types of solutions: laminar solutions in which the flow shows orderly motion and turbulent solutions, which exhibit a chaotic motion associated to a large range of time and length scales. In between these two regimes, the transitional region is observed, in which complex but ordered behaviors are can be found. The transitional regime is rich in different types of solutions as several bifurcations (or drastic changes in the behavior of the solution) are usually observed. For this reason several periodic states are often reported in this regime, which separate the fully laminar steady solutions from the first chaotic pre-turbulent states. The study of this regime allows to develop a greater understanding of how the wake shall develop, and how to define strategies to control it, that will hopefully be efficient at high Reynolds numbers. Due to the non-linear nature of the N-S equations the study of these transitions requires the tools developed in the field of dynamical systems and bifurcations. These tools allow to characterize the transitions based on the linear instabilities of the solutions and study the growing complexity of the new solutions that appear.

1.3. RESEARCH OBJECTIVES

Two main goals were established in the literature study prior to the start of this MSc thesis:

1. To characterize the transition from laminar to pre-turbulent chaotic flow of the Ahmed body wake
2. To determine the effect of active flow control on the transitional regime

To summarize the objectives of this work, a series of research questions have been established. For the first part, the main research question can be stated as:

- What are the main characteristics of the Ahmed body flow in the transitional regime?

This task can be split to two more precise questions:

1. Which wake states can be observed experimentally using DNS of the flow?

2. Are these wake states representative of the high Reynolds behavior?

It is important to note that if the second subquestion is answered negatively, then the model must be rebuild. Having established a representative model of the study target a second research question can be defined:

- How does periodic actuation affect the transitional regimes?

This can be again reduced to more specific questions:

1. Is it possible to trigger different flow states using AFC?

2. Are these states related to the ones observed in the previous part of this work?

3. Which states are more desirable?

4. Is it possible to control which state is triggered?

5. What is the efficiency of the flow control?

The target of this work is to provide a reasonable answer to these questions.

1.4. STRUCTURE OF THE REPORT

This report is structured in three main parts. In the first part the baseline Ahmed configuration is presented: the numerical setup of the problem, boundary conditions and meshing are described, a validation of the model is performed and the results are presented. The temporal evolution and Cl-Cd curves of the different types of solutions are studied at different Reynolds, and the bifurcation scheme of the model is described. Unfortunately the conclusion of this section is that the model does not present the desired flow features due to early separation, and therefore a suction is applied to correct this situation. This part is structured in two chapters: The baseline Ahmed body configuration and Bifurcation analysis for the baseline model.

The modified Ahmed body configuration is presented in the second part of this thesis. It features a description of the changes that have been applied to the original model, a validation of the new flow fields and a study of the new bifurcation scheme. The new model is found to bifurcate at higher Reynolds, which requires a higher mesh density, but presents the expected flow features. Additionally, the variation of the types of flow solutions is found to be small along the transitional regime, which allows to reduce the study of the problem to a significant Reynolds number. This part is structured in two chapters: The modified Ahmed body configuration and Bifurcation analysis for the modified model.

Having determined the new bifurcation scheme of the new model, AFC is applied near the new separation point at a representative Reynolds of the transitional regime. The flow control methodology and necessary changes to the model are described, the problem is validated and the results are presented: different actuation frequencies and amplitudes are compared to both the baseline case (flow without rear actuation) and constant suction. Periodic solutions are found at certain combinations of frequency and amplitude actuations, and the mechanisms by which this occurs are studied. Great attention is put on the changes to the global forces, as they are the most relevant quantities. This part is structured in a single chapter: Application of AFC.

Finally, conclusions are drawn, and recommendations for further work are proposed.

2

THEORETICAL BACKGROUND

2.1. STUDY OF COMPLEX DYNAMICAL SYSTEMS

A dynamical system can be described as a certain model whose time evolution is described by a mathematical model [15]. Dynamical systems may be time-continuous or time-discrete. The former are governed by differential equations, while the latter respond to the iteration of maps (difference equations). The NS equations are the set of non-linear equations that describe the motion of fluids. Non-linear dynamics can become extremely complex in some situations, as the solutions can exhibit completely different forms depending on the value of certain parameters. It is common knowledge that the Navier Stokes equations can present laminar behavior when the Reynolds number is low, turbulent behavior if it is high, natural convection if the Rayleigh number is high, among many others. One of the tools that have been developed to study the behavior of such systems is stability analysis. Stability theory allows to determine the values of a relevant parameter (in the present study *Re*) at which a certain system will experience qualitative changes in its behavior (bifurcations).

The study of bifurcations allows to determine the different qualitative behaviors of the system. This is particularly interesting for flow control, as some states have beneficial properties (for instance low drag) while others do not. The goal is then to determine how a certain beneficial state can be favored in an efficient fashion.

Unfortunately the study of the stability of non-linear systems is complex and dependent of the particular case. To overcome this problem several methods exist: linear stability analysis, weakly non-linear stability analysis, etc. Linear stability analysis is preferred in this work as it provides the most relevant information regarding the stability of the system while keeping a more simple approach than other methods.

In this chapter the application of linear stability theory to the NS equations will be described. The discussion will include the linearization of the NS equations, the most relevant stability analysis tools, and relevant literature regarding the study of the transitional regime applied to bluff body wakes.

2.2. WHY LINEARIZED SYSTEMS?

A linear system is a system that verifies superposition, i.e. scaling of actions results in proportional effects and addition of actions in addition of their individual effects.

Linear systems have an extremely simple behavior that is easy to analyze. Most dynamical systems are however nonlinear, and this introduces a degree of complexity that renders a global analysis unfeasible. Linearization around particular solutions allows for a local analysis that remains valid sufficiently close to the solution around which the system has been linearized.

In stability analysis the focus is placed in the study of certain points that present drastic changes in the behavior of the solution. This implies that the distance from the bifurcation at which a completely new behavior of the system can be observed is small. Therefore the linearized system will offer a good approximation of the qualitative changes in the system at the bifurcation point.

2.3. LINEARIZATION OF THE NS EQUATIONS

In the previous section the interest of studying the linearized version of complex non-linear equations has been discussed. in this section the linearization of the NS equations will be discussed. The NS equations can

be written as:

$$\partial_t \mathbf{u} + (\mathbf{u}\cdot\nabla)\,\mathbf{u} = -\nabla p + \nu\nabla^2\mathbf{u} \tag{2.1}$$

$$\nabla\cdot\mathbf{u} = 0 \tag{2.2}$$

And some boundary conditions. Assuming that a steady solution exists (u_0, p_0):

$$(\mathbf{u}_0\cdot\nabla)\,\mathbf{u}_0 = -\nabla p_0 + \nu\nabla^2\mathbf{u}_0 \tag{2.3}$$

$$\nabla\cdot\mathbf{u}_0 = 0 \tag{2.4}$$

Equation 2.3 is a constrained non-linear system of equations. The constraint comes form the fact that the continuity equation is not a dynamical system, instead it only projects the velocity field to a divergence free space.

A perturbation can be applied to the solution $\mathbf{u} = \mathbf{u}_0 + \epsilon\mathbf{u}'$ $\mathbf{p} = \mathbf{p}_0 + \epsilon\mathbf{p}'$, where $\epsilon << 1$. Substituting and simplifying using eq 2.1 and 2.2:

$$\partial_t\mathbf{u}' + \epsilon\left(\mathbf{u}'\cdot\nabla\right)\mathbf{u}_0 + \epsilon\,(\mathbf{u}_0\cdot\nabla)\,\mathbf{u}' + \epsilon^2\left(\mathbf{u}'\cdot\nabla\right)\mathbf{u}' = -\epsilon\nabla p' + \epsilon\nu\nabla^2\mathbf{u}' \tag{2.5}$$

$$\nabla\cdot\mathbf{u}' = 0 \tag{2.6}$$

Neglecting the high order terms:

$$\partial_t\mathbf{u}' + \left(\mathbf{u}'\cdot\nabla\right)\mathbf{u}_0 + (\mathbf{u}_0\cdot\nabla)\,\mathbf{u}' = -\nabla p' + \nu\nabla^2\mathbf{u}' \tag{2.7}$$

$$\nabla\cdot\mathbf{u}' = 0 \tag{2.8}$$

With homogeneous boundary conditions. This does not depend on the type of boundary condition. Equations 2.7 and 2.8 represent the linearized system of equations, which can be decoupled in the basis of eigenmodes.

Then it is possible to seek for a solution that will only amplify (or decay) the perturbations in time but does not alter them in any other way. $\mathbf{u}' = \sum_j \tilde{\mathbf{u}}_j e^{\lambda_j t}$ and $p' = \sum_j \tilde{p}_j e^{\lambda_j t}$. Since the system is linear each equation can be decoupled:

$$\lambda\partial_t\tilde{\mathbf{u}}e^{\lambda t} + (\tilde{\mathbf{u}}\cdot\nabla)\,\mathbf{u}_0 e^{\lambda t} + (\mathbf{u}_0\cdot\nabla)\,\tilde{\mathbf{u}}e^{\lambda t} = -\nabla\tilde{p}e^{\lambda t} + \nu\nabla^2\tilde{\mathbf{u}}e^{\lambda t} \tag{2.9}$$

$$\nabla\cdot\tilde{\mathbf{u}}e^{\lambda t} = 0 \tag{2.10}$$

In this step a small abuse of the notation has been applied. Since the equations are solved on a finite grid the solution $\mathbf{u}'$ is defined at N grid location points. The linear system is therefore now a system of equations of $3\times N+1$ equations and $3\times N+1$ unknowns: 3 components of velocity and pressure on N grid points. Simplifying:

$$\lambda\partial_t\tilde{\mathbf{u}} + (\tilde{\mathbf{u}}\cdot\nabla)\,\mathbf{u}_0 + (\mathbf{u}_0\cdot\nabla)\,\tilde{\mathbf{u}} = -\nabla\tilde{p} + \nu\nabla^2\tilde{\mathbf{u}} \tag{2.11}$$

$$\nabla\cdot\tilde{\mathbf{u}} = 0 \tag{2.12}$$

Defining the linear operator of velocity as $L_u(x) \equiv \nu x$, the linear operator of pressure as $L_p y \equiv -\nabla y$, the divergence operator as $kx \equiv -\nabla\cdot x$ and the linearized non-linear term as: $D_u N(u_0)x \equiv -\left[(u_0\cdot\nabla)\,x + (x\cdot\nabla)\,u_0\right]$

The system can be rewritten in matricial form:

$$\begin{bmatrix} D_u N(u_0) + L_u & L_p \\ k & 0 \end{bmatrix}\begin{bmatrix}\tilde{\mathbf{u}}\\ \tilde{p}\end{bmatrix} = \lambda\begin{bmatrix}\tilde{\mathbf{u}}\\ 0\end{bmatrix} \tag{2.13}$$

Which is an eigenvalue problem with eigenvalues λ and eigenvectors $(\tilde{\mathbf{u}}, \tilde{p})^T$.

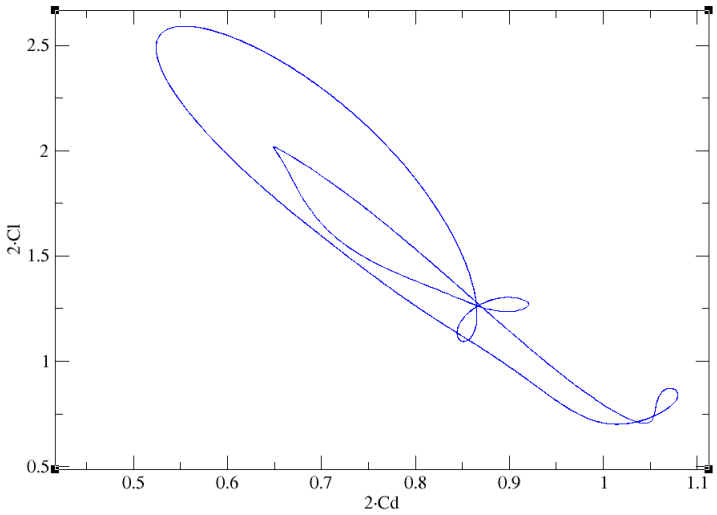

Figure 2.1: Example of a 2D map of the aerodynamic coefficients

It is useful to give a physical interpretation of the eigenvalues and eigenvectors of the system. The eigenvectors were introduced as a certain solution that grew or decayed exponentially in time $\tilde{\mathbf{u}} = e^{\lambda t}$. The eigendirection is then the direction in which a perturbation would grow or decay exponentially without changing its shape (the velocity and pressure field distribution). In the discretized 3D solution, each eigenvector consists in a velocity field and there are as many eigenvectors as nodes the discrete system has. These eigenvector velocity fields can then be understood as the perturbation fields that would produce an exponential growth of growth rate λ. It is customary then to order them in such a way that $Re(\lambda_1) > Re(\lambda_2) > ... > Re(\lambda_i) > ... > Re(\lambda_N)$, where N is the number of discrete equations of the system.

Linear systems allow to study the bifurcations of steady solutions. Unfortunately once the solution becomes unstable the bifurcations of the unsteady solution can be different. It can sometimes occur that the secondary bifurcations of the linear system are similar to the bifurcation of the unsteady solution. However in general this is only an approximation. A better alternative to trying to infer the stability of the original steady solution is to directly simulate the unsteady solution bifurcations. This is more computationally expensive, but since the Reynolds number is low, it can be accomplished.

2.4. REPRESENTATION OF THE SOLUTIONS

Mapping is a very powerful tool for studying the different types of solutions that a dynamical system presents. In this work it has been used to project the solution into a lower dimensional space (2D), for ease of representation. Using this method a steady solution is represented as a point and a periodic solution is represented as a closed loop. This method is commonly used in the field of stability analysis. Two main types of mappings exist: continuous and discrete.

In this work continuous maps have been extensively used to determine the properties of the different types of solutions. These kind of maps are extremely useful when studying periodic solutions. The non dimensional coefficients of lift C_l and drag C_d of the body have been chosen as the most relevant variables to map the solution on a 2D space.

However in some cases the use of continuous maps is not the most useful procedure. In these cases the use of discontinuous maps can provide additional information of the different types of solutions. In this work discrete maps such as Poincaré sections have also been used in the advent of quasi-periodic solutions to overcome the limitations of continuous maps.

2.4.1. CL-CD MAP

One of the most simple maps that can be applied to a certain flow solution is the Cl-Cd map. This map is also one of the most useful ways of classifying the types of solutions as it allows to determine whether a solution is steady, periodic, quasi-periodic or chaotic. A solution is steady if for all times the solution is mapped into a single point. In fluid dynamics steady solutions are only observed for extremely low Reynolds numbers, and represent extremely simple laminar flow states. A solution is periodic if it can be mapped in the parameter

space as a closed curve after one period. In fluid dynamics periodic solutions are often found in the first stages of the transitional regime when vortex shedding is observed. A solution is quasi periodic if its map wounds on a torus (doughnut) densely. Its dynamics respond to two incommensurate frequencies. Finally a solution is chaotic when, independently of the number of periods, it does not close on itself. The number of periods required to determine if a solution is quasi-periodic or chaotic can be large (order 10^2). An example of this kind of representation can be found in figure 2.1.

The choice of Cl and Cd as the representative quantities is motivated by the fact that they are usually regarded as the most relevant quantities in the study of aerodynamic problems. However, in the study of the different types of solutions any quantity that can be extracted from the problem could potentially have been used. Examples of other quantities that could have been used can include point-wise quantities such as the horizontal and vertical velocity at a point located in the wake, pressure drag vs pressure lift, etc. The choice of the lift and drag coefficients has three main advantages: they are integral quantities (and therefore are less subject to local effects), they are computed in the region of interest, and they are the most commonly used quantities in the study of these kind of problems (making them more comparable to other studies).

2.4.2. POINCARÉ MAPS

The Poincaré map is a dynamical system that that maps the system's phase space trajectory with a Poincaré section from one crossing to the next (see Figure 4.1). This type of representation can be described as a discrete map: it represents the solution only at discrete time instants. The Poincaré section is a mapping of the points on S to itself. The Poincaré map can be written as:

$$\mathbf{x}_{k+1} = P(\mathbf{x}_k) \tag{2.14}$$

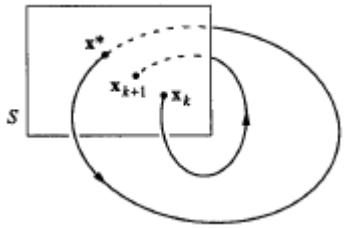

Figure 2.2: Diagram of a Poincaré map. Figure reproduced from [16]

The goal of the Poincaré map is to reduce the study of a limit cycle of a continuous time dynamical system to the study of a fixed point of a discrete time dynamical system. It provides useful information of the time evolution of a solution under the action of a dynamical system. It is a useful tool in determining if a solution exhibits periodic or quasi periodic behavior (for instance after a great number of periods): the Poincaré map of a closed 1 period orbit will always be a fixed point on a map. If the closed orbit closes every two cycles then the the Poincaré map will show two points and so on. If the flow does not exhibit any periodicity the map will show infinite points. The Poincaré map is useful for the study of the destabilization of periodic orbits.

2.5. BIFURCATIONS

A bifurcation is defined as a sudden change in the qualitative behavior of a certain system under a small change of a relevant parameter [16], [17]. In the case of study the NS equations present two distinct solutions: laminar and turbulent. At extremely low Reynolds numbers laminar flow presents a steady ordered behavior. On the other hand turbulent flow presents chaotic unsteady oscillations. Therefore there has to be at least one critical point in which the behavior of the system dramatically changes. In fact this cannot occur in a single step, instead several bifurcations must occur [18] [19].

Bifurcations can be related to the creation or destruction of fixed points, periodic orbits, quasi periodic orbits or to the change of stability of these types of solutions. In complex systems the study of bifurcations is usually performed through the study of their maps. Two main types of mapping methods can be used: discrete and continuous maps. The study of bifurcations must therefore include the qualitative changes for both types of dynamical systems. A thorough analysis of the advent of these bifurcations has shown that this can only occur in a limited number of ways. This will be further explained in Section 2.5.2. To introduce the study that is presented in this thesis, it is necessary to introduce two theorems, the center manifold theorem

and the normal form theorem. These fundamental laws describe the basis of what will be presented along this document.

2.5.1. CENTER MANIFOLD THEOREM

The center manifold theorem states that at a bifurcation point the dynamics of a system are governed by the evolution of a certain critical mode, while all other modes are forced to follow [16], [20]. It also states that a manifold is stable if the real part of all eigenmodes of the (linearized) system are negative and unstable if the real part of all eigenmodes are positive. This implies that the system will go through a bifurcation when the real part of the first eigenmode changes sign. Close to the bifurcation point the system can be approximated as the linearized system. Therefore the center manifold theorem states that sufficiently close to the bifurcation point the stability of the system is defined by the eigenvalue problem defined by the Jacobian of the linearized system.

According to the center manifold theorem, if a system is stable the real part of all the eigenvalues of the linearized system should be negative. Then its stability will change when its first eigenvalue becomes 0.

This theorem provides the tools to determine the stability of the system after a bifurcation occurs. Furthermore, the study of the bifurcation can be reduced to the study of only the nodes that become positive. Generically, only as many eigenvalues can be made to change stability simultaneously as control parameters has the system. The key to understanding the stability of the system is to study the mode that will change sign.

In linear systems the growth of an positive eigenvalue near a bifurcation is exponential. In non-linear systems this will only occur during the initial transient, and when the solution is sufficiently far away from the stable solution the second, third and all other orders will take control of the system, avoiding a blowup.

2.5.2. NORMAL FORM THEOREM

The normal form theorem is a powerful tool in the classification of bifurcations. The main concept behind it is that the ways in which a system can bifurcate are limited and depend on the dimension of the system. Intuitively the normal fold theorem states that sufficiently close to the critical point the way in which the bifurcation occurs is always similar to one of the prototypical cases. Then it is possible to determine the normal form of a bifurcation. Some of the most common bifurcations can be saddle-node, pitchfork, Hopf, Neimark-Sacker or period doubling. The application of the normal form theorem allows to study these types of bifurcations independently of the problem of study, and the results of the study of the prototypical bifurcations simplify the study of the stability of any problem.

It is important to note that the normal form theorem only accounts for the linear and minimal non-linear terms that describe the nonlinear dynamics of the system close to the bifurcation point. This implies that in some cases it can conclude that there is no stable solution, leading to a blowup. In reality higher order terms take control of the system when the distance form the bifurcation is large, preventing the blowup scenario. However, in the classification of bifurcation points, the normal form theorem allows to describe accurately the behavior of the system.

2.5.3. PROTOTYPICAL BIFURCATIONS OF CONTINUOUS MAPS

Continuous maps are those maps that represent the solution for all time instants. These maps are usually used to simplify those solutions which present a complex spatial distribution, as they reduce the order of the representation. Continuous maps are particularly useful in the study of solutions which present a simple temporal evolution such as steady and periodic orbits. The study of the types of bifurcations that these maps can present can be reduced to the study of the most relevant prototypical bifurcations. In this work two types of bifurcations of continuous maps have been studied: saddle node and hopf bifurcations.

SADDLE NODE BIFURCATION

The saddle node bifurcation is one of the basic ways in which fixed points can be created or destroyed, and occurs when a real eigenvalue becomes unstable. It can be observed when by varying the control parameter two fixed points collide, annihilating each other. A fixed point stable solution is destroyed, leading to a blowup of the linear system. A graphical representation of this bifurcation is presented in figure 2.3: a stable fixed point (black dot) collides with an unstable fixed point (white dot) for a value of the parameter equal to 0, both annihilate and for values of $\mu < 0$ no fixed point can be found. Saddle node bifurcations account for brusque changes in the behavior of a certain solutions. A simple example of a saddle node bifurcation is the problem in which a ball is placed on a slope. Assume a slope such as the one presented in figure 2.4. Depending on the

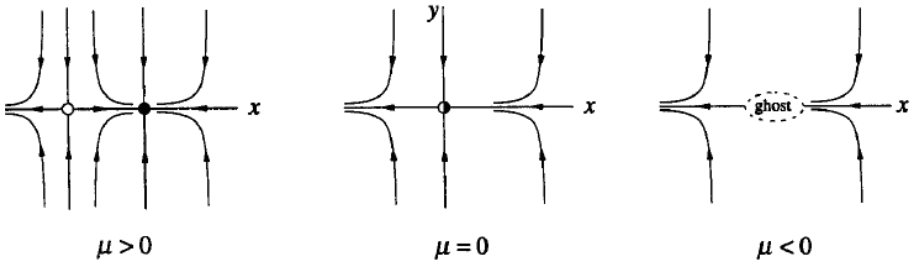

Figure 2.3: Representation of a saddle node bifurcation

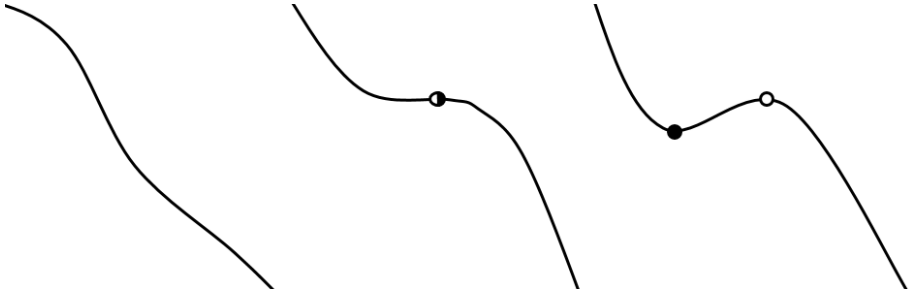

Figure 2.4: Slope problem bifurcation

slope, there can be 1 marginally stable node, a pair of stable-unstable locations or none. Another example of saddle node bifurcation is the straight leveled flight problem. Taking thrust as the main parameter of study three types of solutions can be obtained: for insufficient thrust it is impossible to maintain horizontal flight and no solution can be found. If exactly the minimum thrust is applied, then the solution is unstable, making the aircraft very difficult to pilot. Finally when additional thrust is applied, then parasitic drag dominates the problem and one stable solution can be found.

HOPF BIFURCATION

A Hopf bifurcation is a bifurcation of an equilibrium point of a dynamical system in which at the critical point the modes that become unstable are purely imaginary. This generates a family of closed fixed point curves, which are also known as limit cycles. Two types of Hopf bifurcations have been described: sub-critical and supercritical, depending on the stability of the periodic orbit. Stable fixed points destabilize through supercritical bifurcations, becoming unstable and generating stable limit cycles. This is represented in figure 2.5a. The limit cycle behaves as an orbit when time tends to infinity, as all nearby trajectories are attracted by it. On the other hand, unstable fixed points, destabilize through supercritical bifurcations, creating unstable limit cycles which repel all trajectories. This type of limit cycles divide the phase space into two basins of attraction (the new fixed point and infinity) as shown in figure 2.5b. Hopf bifurcations are the basic way in which periodic solutions are born. A good example of a Hopf bifurcation can be found in the cylinder wake at the onset of vortex shedding, presented in figure 2.6. The flow transitions from a steady solution to a solution in which the wake is periodic locally, and then the instability becomes large, forcing the whole wake to oscillate periodically. Another example of a Hopf bifurcation can be found in the field of aero-elasticity in the case of flutter: under some conditions a wing can begin to oscillate periodically due to the aerodynamic forces, leading to a dangerous scenario in which the structure can fail due to fatigue.

2.5.4. PROTOTYPICAL BIFURCATIONS OF DISCRETE MAPS

Discrete maps can be used to simplify the study of solutions which present complex temporal evolutions. To do so, the temporal evolution is reduced to a number of discrete points. The study of these dynamical systems can be reduced to the study of their prototypical bifurcations. The two most relevant prototypical bifurcations of these maps for this work have been described: Neimark-Sacker and period doubling.

NEIMARK-SACKER BIFURCATION

A Neimark-Sacker bifurcation is a bifurcation in which a discrete dynamical system with a fixed point destabilizes, generating a closed curve of fixed solutions. This type of bifurcation is similar to the Hopf bifurcation

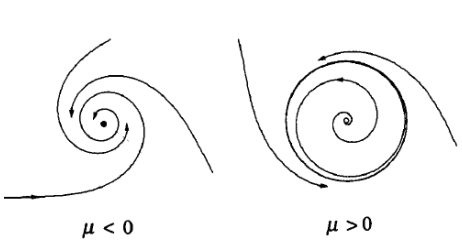

(a) Supercritical Hopf bifurcation

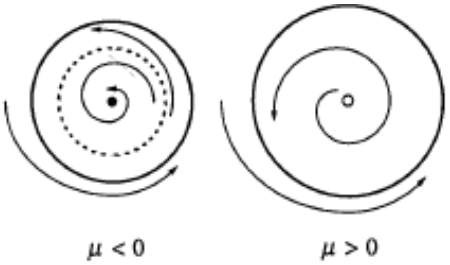

(b) Sub-critical Hopf bifurcation

Figure 2.5: Representation of a Hopf bifurcation

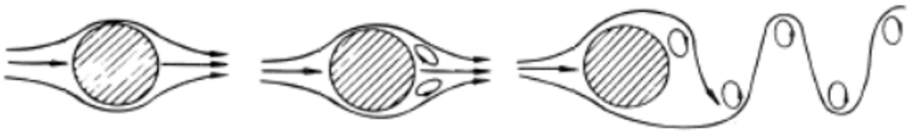

Figure 2.6: Cylinder base bifurcation scheme

in the sense that a curve of fixed points is born from a fixed point, and also because the eigenvalue that has become unstable at the critical point is purely imaginary. The closed curve that is generated can be both continuous and discrete, depending on whether the new solution periodically falls on the same points or not. This is due to the fact that the dynamical system of study is discrete, and therefore so is the solution. Neimark-Sacker bifurcations are particularly interesting because they can be responsible for the transition of ordered solutions to chaotic states: a quasi-periodic solution generated by this bifurcation can become chaotic by the loss of regularity of the solution.

PERIOD DOUBLING BIFURCATION

A period doubling bifurcation is a type of bifurcation in which a periodic orbit becomes unstable and a new stable orbit of double period is born. Period doubling bifurcations are interesting because they allow for an ordered solution can become chaotic: usually this occurs in a cascade fashion, several period doubling bifurcations are observed separated by increasingly smaller distances. Eventually, the solution reaches a point in which the periodicity is lost. An interesting fact that is observed in this type of cascades is that periodic windows are usually observed in the chaotic regime: regions of order inside chaos. The difficulty in the study of period doubling bifurcations is that the distance between bifurcations is reduced after every bifurcation, and therefore at some point the bifurcations are so close to each other that they cannot be distinguished. The most relevant example in the study of this type of bifurcation is the logistic map. In this example, depending on the value of a parameter, the solution can present periodic solutions of period 1, 2, 4, etc, or chaotic solutions [16]. Figure 2.7 shows the typical representation of a period doubling bifurcation, in which a periodic solution of period 1 is shown for values of $a < 3$. When the critical point is reached two stable solutions are observed for $a \in (3, 3.4)$, as the solution will travel from one to the other periodically. Therefore the period has doubled. This occurs several times and eventually chaos is reached.

2.5.5. SUMMARY

The study of bifurcations allows to determine the different qualitative behaviors of the system. Furthermore, the study of the different maps allows to determine the bifurcation scheme and classify the different bifurcations into "prototypical" bifurcations. The study of the flow states and bifurcations is particularly interesting for flow control, as some states have beneficial properties (for instance low drag) while others do not. The goal is then to determine how a certain beneficial state can be favored in an efficient fashion.

2.6. BIFURCATION STUDIES APPLIED TO BLUFF BODY WAKES

In this section the author will describe the most important contributions in the field of stability analysis applied to aerodynamic problems.

In the study of aerodynamic problems from the stability point of view, authors have mostly focused in symmetric cases (spheres, disks, etc.). Symmetric cases are interesting because for low Reynolds the flow

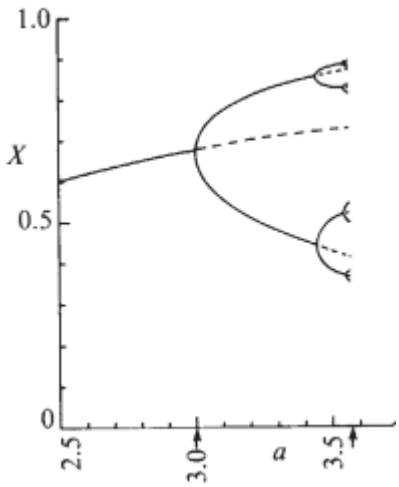

Figure 2.7: First period doubling bifurcations of the logistic map. Figure reproduced from [21]

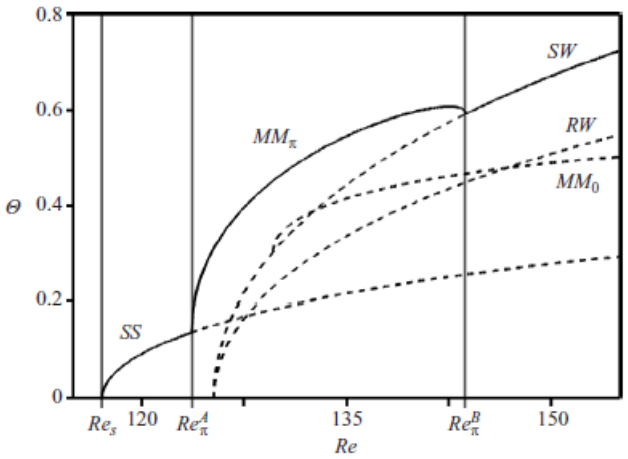

Figure 2.8: Bifurcation map for the disk, figure reproduced from [24]

structure will respect the symmetry of the problem. Pitchfork and Hopf bifurcations are usual in these cases. In this work the Author will focus in the cases that possess a blunt trailing edge. The particularity of these systems is that the separation point is fixed. Therefore the Author will review the literature regarding stability studies on disks, axis-symmetric bluff bodies and the Ahmed body.

2.6.1. FLOW ON THE DISK

Natarajan [22] Fabre [23] and Meliga [24] have performed relevant contributions to the stability analysis of flow on a disk. Meliga studied the theoretical bifurcation diagram and performed linear and weakly non-linear analysis of numerical solution. Using linear analysis the first two bifurcations can be determined: the first one is steady ($\omega = 0$) and the second one is unsteady ($\omega > 0$). Then weakly non-linear analysis can be used to complete the bifurcation map shown in Figure 2.8.

For very low Reynolds the solution is steady and axis-symmetric. A first steady bifurcation occurs at $Re \backsimeq 115$, and the solution looses the axis-symmetry but keeps a reflectional symmetry. When Reynolds is increased the center of the wake moves away from the disk and for $Re \backsimeq 125$ the steady state (SS) solution becomes unstable through a Hopf bifurcation and looses its symmetry. During the bifurcation the first destabilizing eigenmode of the system becomes unstable and the solution will present a natural frequency of Strouhal number $St = 0.121$ [24]. At the threshold of the first bifurcation (stable) all perturbations will decay, however on the threshold of the second bifurcation some regions will amplify the perturbations very fast and others much slower. These regions are the most susceptible regions of the flow.

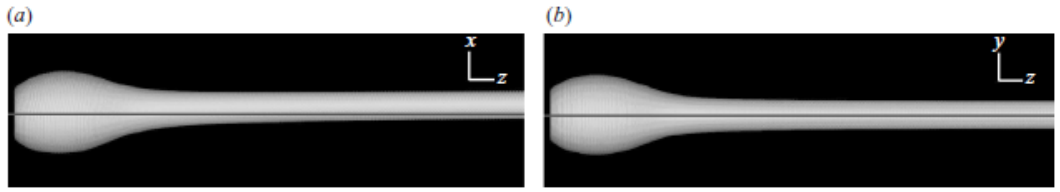

(a) Steady solution ($Re < 115$)

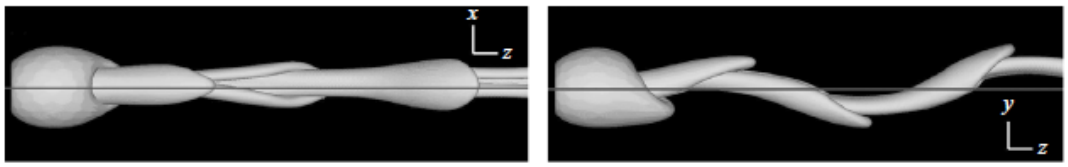

(b) Unsteady non symmetric solution ($115 < Re < 125$)

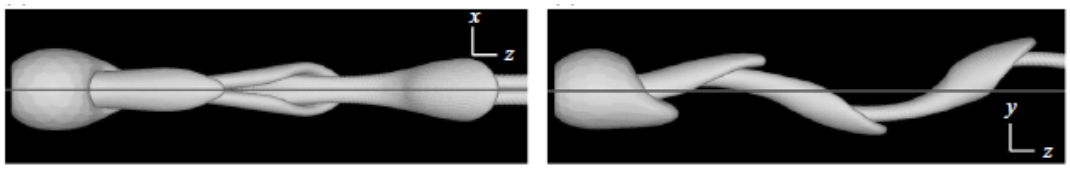

(c) Unsteady symmetric solution ($125 < Re < 140$)

Figure 2.9: Top and side view of the wake, black line represents the main axis of symmetry. Figures reproduced form [24]

According to [23] a symmetry preserving bifurcation is also possible (as it is for the sphere), however for the disk wake this bifurcation would be unstable. Fabre [23] defines these two possibilities as Reflectional Symmetry Preserving (RSP) and Reflectional Symmetry Breaking (RSB). Interestingly a last bifurcation occurs at $Re \backsimeq 140$ which restores the reflectional symmetry of the wake but in a plane perpendicular to the previous reflectional symmetry plane or Standing Wave state(SW). The three flow states can be observed in Figure 2.9

CONCLUSIONS

The wake of the disk is characterized by a steady symmetry breaking bifurcation, an unsteady symmetry breaking bifurcation and an unsteady symmetry restoring bifurcation. These results were obtained with the use of both linear analysis and weakly non-linear analysis, the only difference between the two being the accuracy of the bifurcation point. Therefore the Author concludes that the flow on the disk can be qualitatively studied using linear analysis.

2.6.2. FLOW ON THE AXIS-SYMMETRIC BLUFF BODY

The axis-symmetric bluff body is a bullet-like body with a blunt trailing edge. The main differences with the Ahmed body is that the section is circular and no ground is present. The axis-symmetric bluff body shares some similarity with the disk and some with the Ahmed body. The topology of the wake is shown in Figure 2.10.

According to Bury [25] and Rigas [26] at low Reynolds the wake of associated to the bluff body is a toroidal structure. A first bifurcation occurs at $Re = 450$ and the wake loses the axial symmetry in favor of a specular symmetry. The destabilization of the torus shape wake is shown in Figure 2.10a and the new specularly symmetric wake is shown in Figure 2.10b.

For $Re = 600$ the wake becomes unstable. This bifurcation preserves the reflectional symmetry of the wake (RSP). An interesting feature of this state is that it can be divided in three sub-states. First there is only one fundamental frequency ($St = 0.12$), and the lobes are equally spaced. Note that this frequency is almost identical the natural frequency of the first unstable mode of the disk. Then a second peak in the frequency spectra appears, which is associated to vorticity bursts. The dynamics of the wake become more and more affected by this new frequency until the system becomes chaotic (but preserving the reflectional symmetry). This process is shown in Figure 2.10c.

The wake instabilities grow for increasing Reynolds and finally at $Re = 900$ the wake goes through another bifurcation and looses the remaining symmetry (RSB). For $Re > 1000$ the wake becomes chaotic.

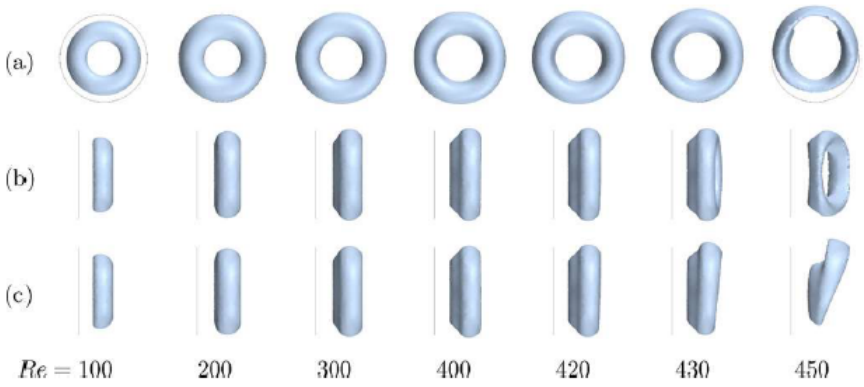

(a) Steady axis-symmetric solution

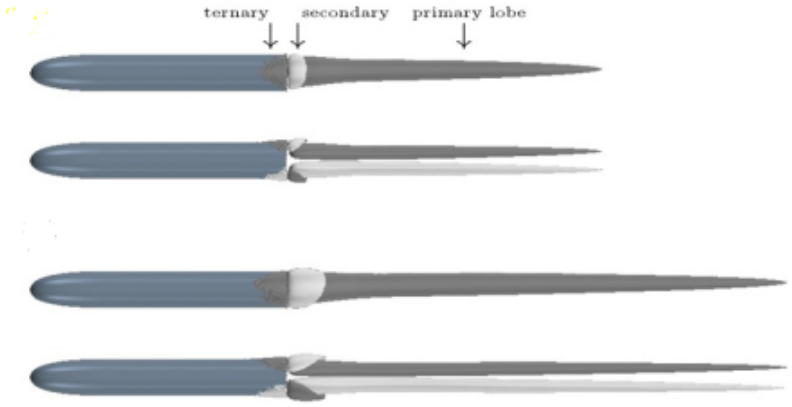

(b) Steady solution with reflectional symmetry (top: $Re = 450$, bottom: $Re = 550$)

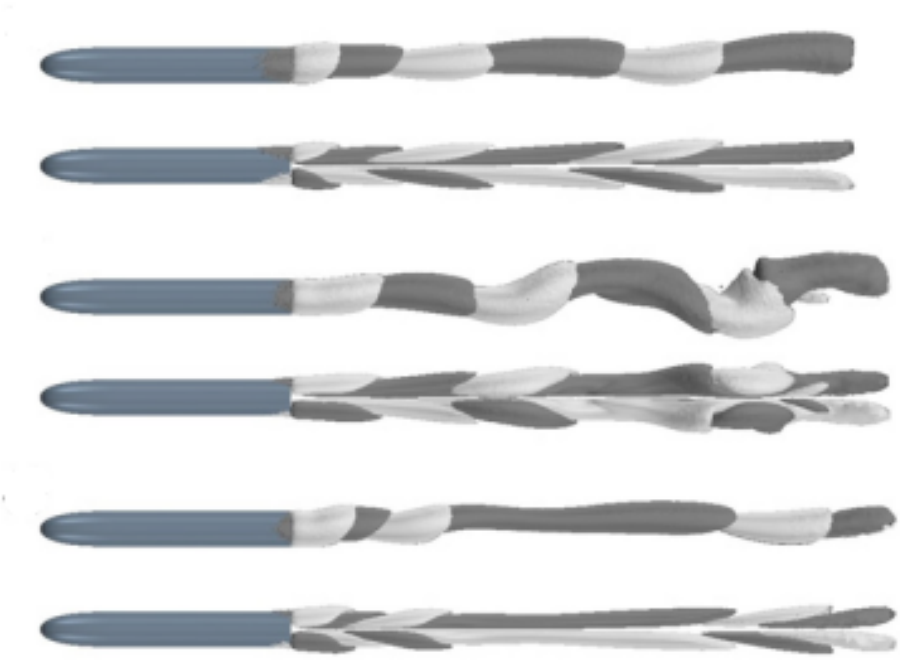

(c) Unsteady solution ($Re = 600, 700, 800$). For $Re = 1000$ the wake is chaotic

Figure 2.10: Top and side view of the wake. Figures reproduced form [25]

According to Bohorquez [27] the aspect ratio of body determines the critical Reynolds values. In his study he used a body with an aspect ratio of 1 and 2, while bury [25] used a body of aspect ratio 7. This explains why he predicted that the first bifurcation should appear for a Reynolds a 50% lower than bury for $L/D = 2$ or 70% lower for $L/D = 1$. Furthermore, he also compared the predicted values using linear theory and experiments, and determined that linear theory overestimates the Reynolds critical values. The most remarkable fact, however, is that linear stability studies can accurately predict the bifurcations and the properties of the wake in the transition states even if the critical point is not determined correctly.

Rigas [28] studied the high Reynolds chaotic regime experimentally. He concluded that the wake has two main characteristic frequencies: one due to vortex shedding ($St = 0.2$) and one associated to the rotation of the vortex shedding plane ($St = 0.002$). This is relevant because he determined that the vortex shedding frequency at the chaotic regime could be related to the low Reynolds flow properties. Therefore, Rigas concluded that the large scale coherent structures of the turbulent regime maintain a relation with the low Reynolds instabilities in a statistical sense.

CONCLUSIONS

The wake of the axis-symmetric bluff body is characterized by a steady symmetry breaking bifurcation, an unsteady reflectional symmetry preserving bifurcation and an unsteady symmetry breaking bifurcation.

When comparing to the disk, it is possible to conclude that the destabilization of the wake is qualitatively different since in the disk wake the symmetry of the wake is broken first to then be recovered while this does not occur in the axis-symmetric bluff body case. However, the natural frequency of the flow at the first unstable state is similar, which seems to point out that the first transition to unstable behavior is similar.

Linear studies have been found to be a good tool for determining the qualitative behavior of the wake. However they do not seem to predict correctly the exact value of the critical points, which they tend to overestimate. This is similar to what other literature reports for the disk.

Evidence was found that supports the idea that instabilities at the transitional regime can be directly related to the vortex shedding properties of the turbulent regime [25], [27], [28]. Since vortex shedding is the most relevant phenomenon of the wake in both regimes Rigas [26] showed that both vortex shedding and vortex shedding actuation could be described using transitional regime tools for much larger Reynolds. The author concludes therefore that the implementation of flow control strategies that target vortex shedding suppression at transitional Reynolds can be representative of flow control strategies at turbulent Reynolds.

2.6.3. FLOW ON THE AHMED BODY

In Chapter 3 the Ahmed body geometry was classified into square and slanted. Less literature exists regarding stability studies in this geometry than for the disk or axis-symmetric bluff bodies, and it is generally focused on the 3D square Ahmed body.

SQUARE AHMED BODY

Grandemange [29] studied the low Reynolds Ahmed body wake and determined that the wake is steady and symmetric left to right. When increasing the Reynolds number a Reflectional Symmetry Preserving (RSP) bifurcation is observed, leading to an unsteady symmetric left to right wake. This bifurcation is identified as a Pitchfork bifurcation, as two symmetric states are possible.

Then by further increasing the Reynolds number a new bifurcation is observed and the wake became stable again but lost its symmetry, in what can be described as a Reflectional Symmetry Breaking bifurcation (RSB). It is worth mentioning that the wake seems to have turned 90° and is now aligned with the floor plane. Furthermore this state only appears if the ground clearance is greater than 0.4. It seems that the wake can only orient itself parallel to the ground plane if there is enough flow on the underbody.

Finally, the wake undergoes a last bifurcation to become unstable and non-symmetric. Dye images of the wake from [29] are shown in Figure 2.11.

The flow behavior at high Reynolds number regime retain some of the characteristics of the transitional regime. This seems to be due to the fact that the main phenomena driving the dynamics of the system is in both cases vortex shedding. This thesis is supported by the fact that peaks at the vortex shedding frequency can be observed both at transitional and highly turbulent regimes. The exact Strouhal number associated to vortex shedding is more controversial. Grandemange [29] proposes 0.17 (vertical) and 0.127 (horizontal), which is in good agreement with Li [30] and Volpe [31] 0.19 (vertical) and 0.13 Horizontal, however Pastoor [5] finds 0.23, which is in better agreement with Bruneau [32], Parkin [33] or Henning [34] who propose 0.25.

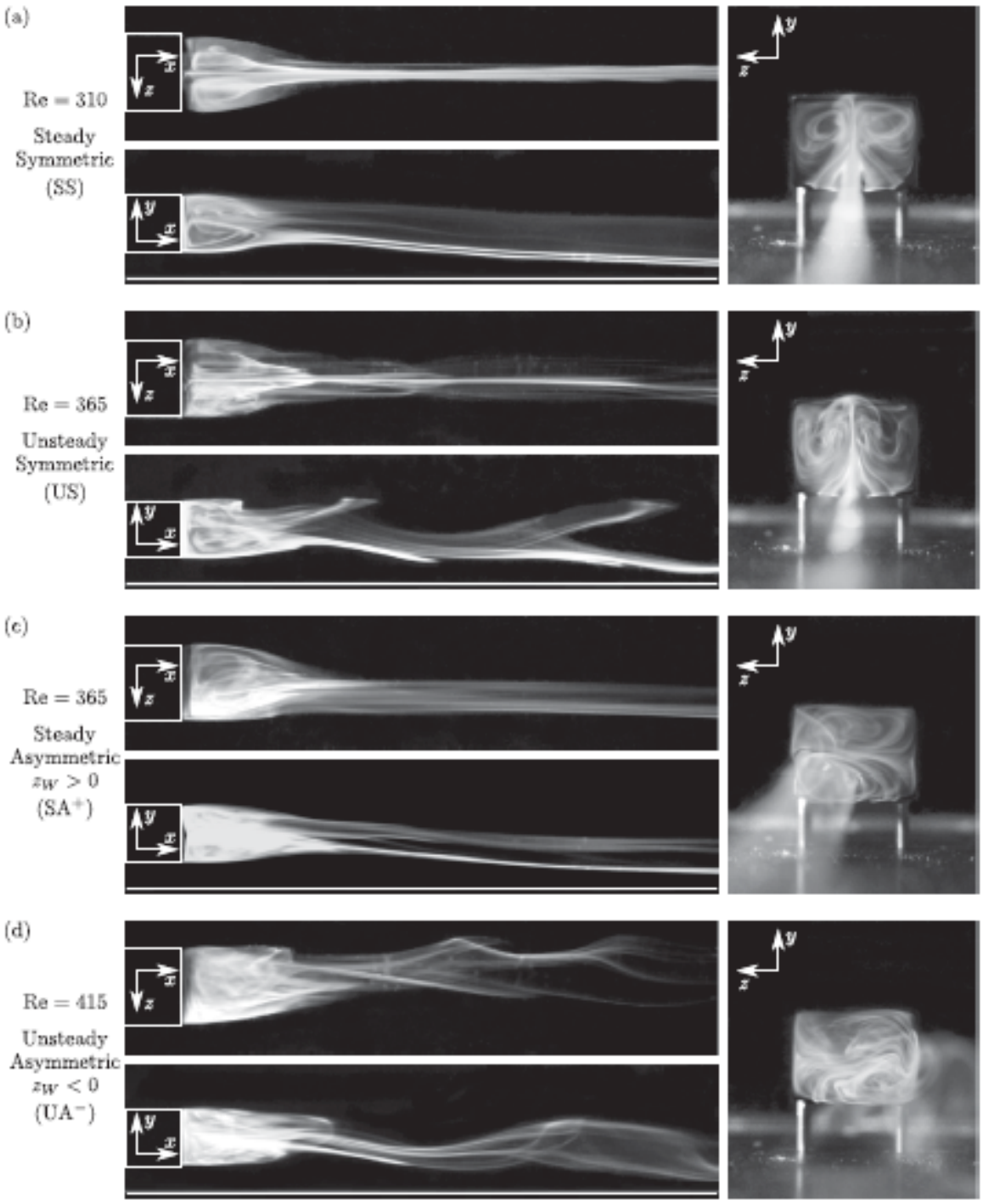

Figure 2.11: Transitional states of the Ahmed body wake, figure reproduced from [29]

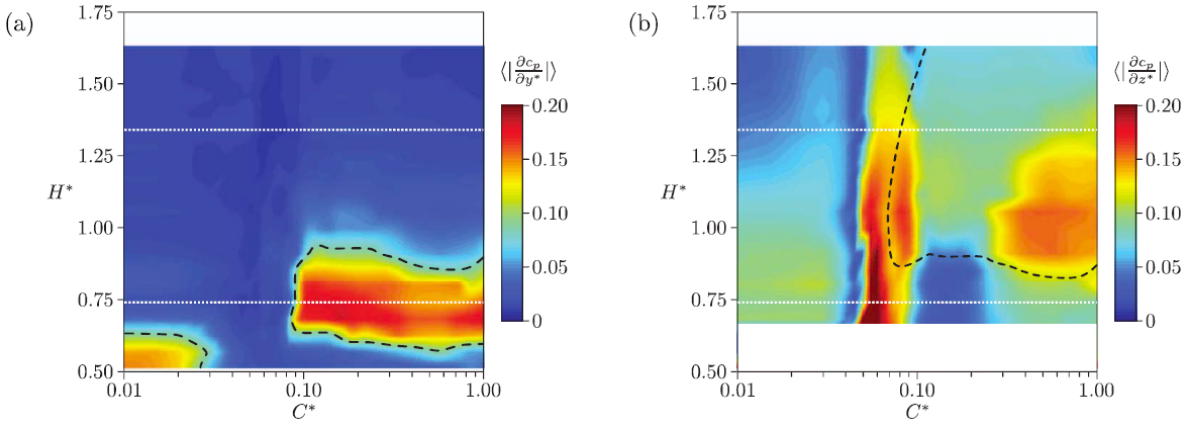

Figure 2.12: Effect of ground clearance and aspect ratio on the pressure gradients (horizontal, left and vertical, right) at the center of the rear base, figure reproduced from [37]

Grandemange [29] determined that the location at which the measuring took place was relevant when determining the frequency of vortex shedding. This could be the reason for which the results vary so much between different authors. Tunay [35] proposes that the reason for this variation could also be related to how the Strouhal number is computed. Some authors determine the results from the total forces of the vehicle, while others use properties of the flow, as for instance the pressure gradient at the center of the cavity. It is not illogical then to assume that all authors observe the same phenomena even if the values do not match exactly.

In this regime the center of pressure (and therefore the wake) is reported to switch between two preferred positions randomly [36]. These positions can be associated to the two stable positions that appear at the transitional regime after the pitchfork bifurcation. This behavior is reported to be Reynolds independent. The characteristic timescale of this switching is much smaller than the vortex shedding. However, according to later articles [37], [38] this can be highly influenced by ground clearance and aspect ratio of the body. The bi-stability of the wake can be analyzed through the pressure gradient at the center of the cavity. Figure 2.12 shows the pressure gradient at the center of the cavity as a function of the aspect ratio and the ground clearance. From the Figure it is clear that horizontal bi-stability is only possible for low aspect ratios and vertical bi-stability is only possible for large enough ground clearances.

Other authors [39] have also observed these low frequency oscillations, but attributed it to bubble pumping (a low frequency change in size of the recirculation bubble) while other authors [14] do not report this frequency at all. Parkin [33] (who has studied the 2-D Ahmed body) did not observe the low frequency oscillations either. Due to the high aspect ratio the bistable lateral vortex shedding does not appear. This is supported by the studies of Grandemange, [37], which determined the aspect ratio is a key element in whether the bi-stability appears or not.

Varon [40], recently studied the bistable behavior from a deterministic point of view (opposed to the stochastic approach proposed by Grandemange). According to his data the barycenter of pressure seems to present dynamics that resemble a strange attractor similar to the one first presented by Lorenz [41]. The author concludes that the nature of the bistable behavior of the wake is still controversial.

Gentile [42] and Rigas [28] have linked the bistable symmetry breaking motion of the center of pressure of the Ahmed body wake to the fluctuations of the center of pressure of the bluff body wake. According to this authors the low frequency oscillations around the center of the body are the same phenomena, the only difference being that the in this case the symmetries are infinite, and so there are as many stable points forming a circle.

Interestingly, in the highly turbulent flow (in average) symmetry is restored. This could be related to what occurs in lower order dynamical systems when a fixed point is destroyed: even if the fixed point has vanished, a ghost remains which influences the system [16]. In this case the two attractors seem to be ghosts of the two stable points that appear when the system goes through a pitchfork bifurcation at the transitional regime.

CONCLUSIONS

The square Ahmed body wake transitions to chaos through the following stages:

- An unsteady symmetric state. This bifurcation is identified as a pitchfork bifurcation.
- A steady non-symmetric state. This state only appears if the ground clearance is large enough.
- An unsteady non-symmetric state

When the wake destabilizes it is due to vortex shedding. This phenomenon will dominate the wake both during transition and after the chaotic stage is reached. Additionally, the highly turbulent wake is determined by a low frequency bi-stable behavior. The wake seems to switch between two stages that are similar to the two symmetric positions that appeared after the first pitchfork bifurcation.

When comparing the Ahmed body wake to the bluff body wake it seems that the type of bifurcations are different from one to the other. However they do share the common feature that vortex shedding dominates the wake both in some transition states and at the chaotic state. The bi-stability of the wake seems to be a singular feature of the 3D Ahmed body and seems to be due to the fact that it is only symmetric in two planes. This does not allow for the wake plane to rotate as it did in the case of the axis-symmetric bluff body, and drastically changes the transitions sequence to turbulence. The behavior of the wake is then determined by two characteristic time scales: vortex shedding $St \propto 10^{-1}$ and the switching between the two bistable points. As stated in the studies of the axis symmetric bluff body, evidence indicates that the active flow control strategies developed at transitional regimes can be successfully applied to higher turbulent regimes if they target vortex shedding suppression.

Finally attention should be put when choosing the ground clearance, since it can drastically change the topology of the wake, and therefore the bifurcations sequence. A ground clearance of more than 0.1 is essential, and a ground clearance of 0.4 is recommended.

SLANTED AHMED BODY

The bifurcations sequence from laminar regime to pre-chaotic behavior of the slanted Ahmed body geometry has not been characterized to the best of the authors knowledge. It seems then that it is a good research area, as it presents some characteristic features that can be of interest. However, there are several studies regarding the highly turbulent regime.

The dynamics of the slanted Ahmed body wake are directed by vortex shedding. Therefore the spectral analysis of the wake shows a peak at the vortex shedding frequency. Thacker [43], Joseph [14], Duell & Geroge [39] and Parkin [33] report a peak at $St = 0.11, 0.1, 0.07, 0.22$ respectively although in the last case the geometry is 2D, making it less comparable to the 3D cases, but more comparable to this work.

According to Barsotti [9] the turbulent regime of the slanted geometries presents a second characteristic peak different from vortex shedding. This peak can be associated to shear layer Kelvin-Helmholtz instabilities, which typically occur as the destabilizing phenomena in shear layers. The author concludes that this can occur in the cases where the wake detaches and a shear layer appears in the separated region. Thacker [43] and Joseph [14] also observe a second frequency peak in the shear layer region, but associate it to its flapping motion. The reason of this additional frequency is yet to be fully understood.

3

THE BASELINE AHMED BODY CONFIGURATION

3.1. AHMED BODY GEOMETRY

The geometry of the Ahmed body that will be simulated is presented in figure 3.1. To simplify the computation of the Reynolds number of the problem Re_H the height of the model has been imposed to be $H = 1$ and the inlet velocity is imposed to $u = 1$. Therefore the following measures are imposed: $h = 0.1736$, $L = 3.6825$, $L_{slant} = 0.7929$ and $\alpha = 25$. The density of the problem is also imposed to be $\rho = 1$, and the desired Reynolds number can be imposed through the modification of the kinematic viscosity ν.

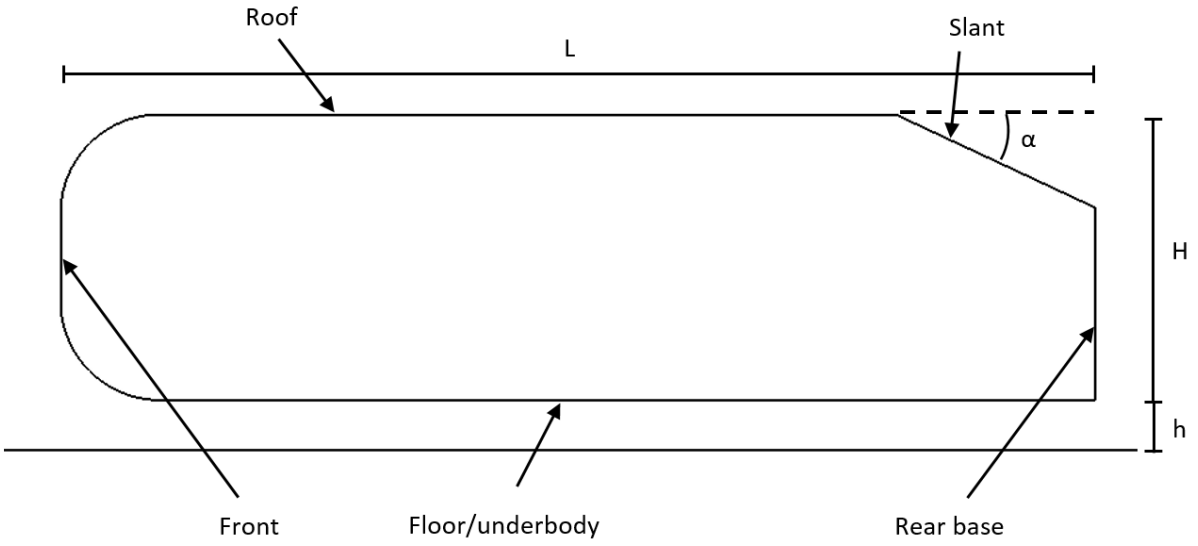

Figure 3.1: Ahmed body geometry

3.1.1. NUMERICAL SETUP

As in any numerical simulation, the first step that is required is the definition of the domain. To define it three main dimensions have been defined H_1, L_1 and L_2 (shown in figure 3.2). The rectangular shape of the domain is standard in literature.

It is general knowledge that the domain size can greatly affect the solution due to boundary conditions interference. This is due to the fact that far field conditions do not necessarily apply at the chosen boundary locations, forcing an unphysical solution of the problem. During the literature study performed prior to the start of this thesis the following minimum domain sizes were determined: the inlet should be located at least 10H upstream from the Ahmed body geometry, and that the outlet should be located at least 20H

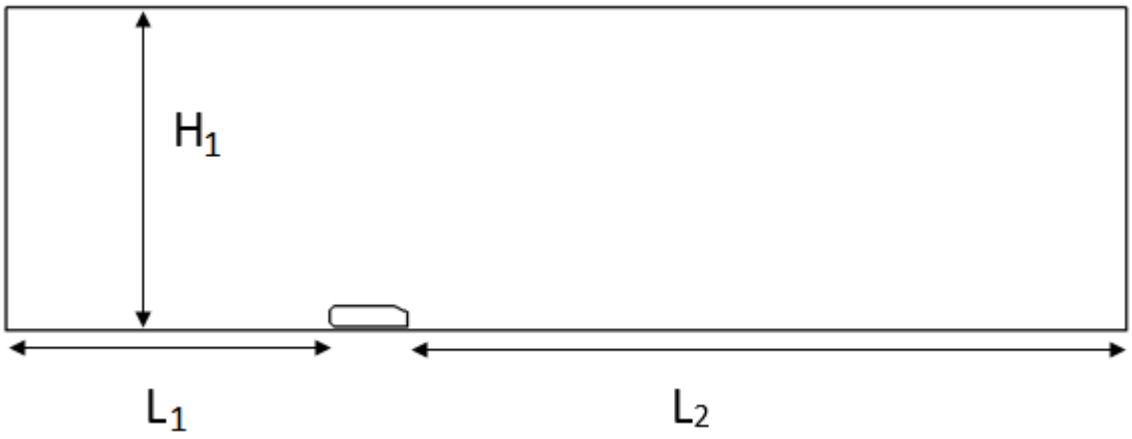

Figure 3.2: Domain dimensions

downstream from it. The ceiling location is also recommended to be located at least 10H. To validate these recommendations the author has performed a study to determine the impact of boundary conditions.

3.1.2. BOUNDARY CONDITIONS

The boundary conditions of the problem have been set in the following way[1]:

1. Inlet: The inlet velocity is set to free-stream horizontal velocity and 0 vertical velocity
2. Outlet: Convective (robin) outlet boundary conditions have been applied to u, v and p. This type of boundary conditions can be specified in the Nektar++ to reduce instabilities when energetic vortices cross the boundary[44].
3. Ahmed body boundary: Both horizontal and vertical velocities are imposed to 0.
4. Bottom wall: Horizontal velocity is imposed equal to free-stream velocity and vertical velocity is imposed to 0.
5. Top wall: Horizontal velocity gradient is imposed to 0 and vertical velocity is imposed to 0.

3.1.3. MESHING

Producing a quality mesh is one of the most important steps when solving the Navier-Stokes equations. Mesh design determines the quality of the solution and computational efficiency.

The meshes described in this section will be 2D to reduce the computational effort of the simulations. However some of the simulations performed in this project are quasi 3D. The mesh that has been used in these cases is exactly the same, since Nektar++ allows to expand the 3rd dimension using Fourier expansions. To produce the 2D meshes the software Gmsh has been used.

MESH TOPOLOGY

To mesh the domain a structured approach has been used. However, in the region adjacent to the bottom front region the author has chosen an unstructured algorithm to improve the mesh quality. Additionally the domain has been divided in 3 main zones to allow for localized sub-grid refinements (see figure 3.3). These refinements are implemented directly in the solver software as polynomial expansions. In the boundaries between regions of different order the base functions of largest order are truncated. For this reason it is recommended that the difference in order between two adjacent regions is 2 or lower. For this reason 3 regions have been implemented: then it is possible to have a very large order (8, for example) in the near wake and 4 in the very far wake, with an intermediate region of order 6 in between.

The order of the polynomial expansions will be a key parameter in adequately representing the flow properties. This is particularly relevant immediately at the boundary layer, as to adequately represent it, the first node should be in the laminar sub-region of the flow. This criterion is the y+ criterion and should be taken

[1] pressure gradient is always imposed to 0, unless specifically specified otherwise

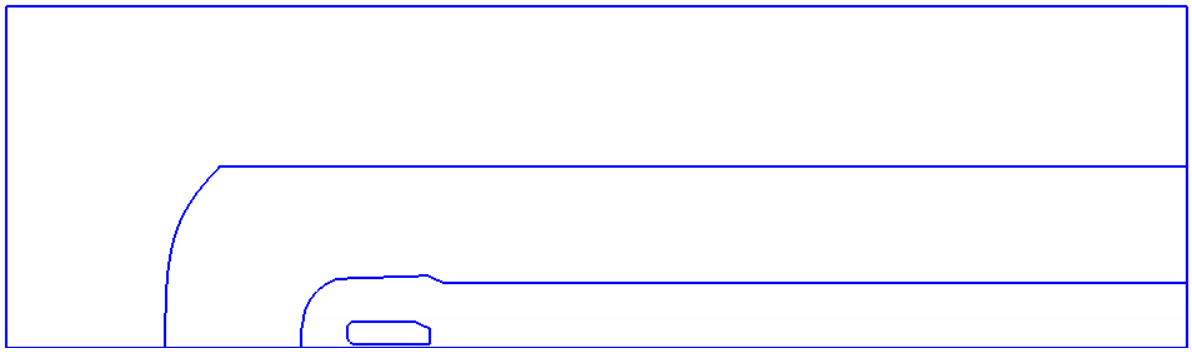

Figure 3.3: General mesh topology

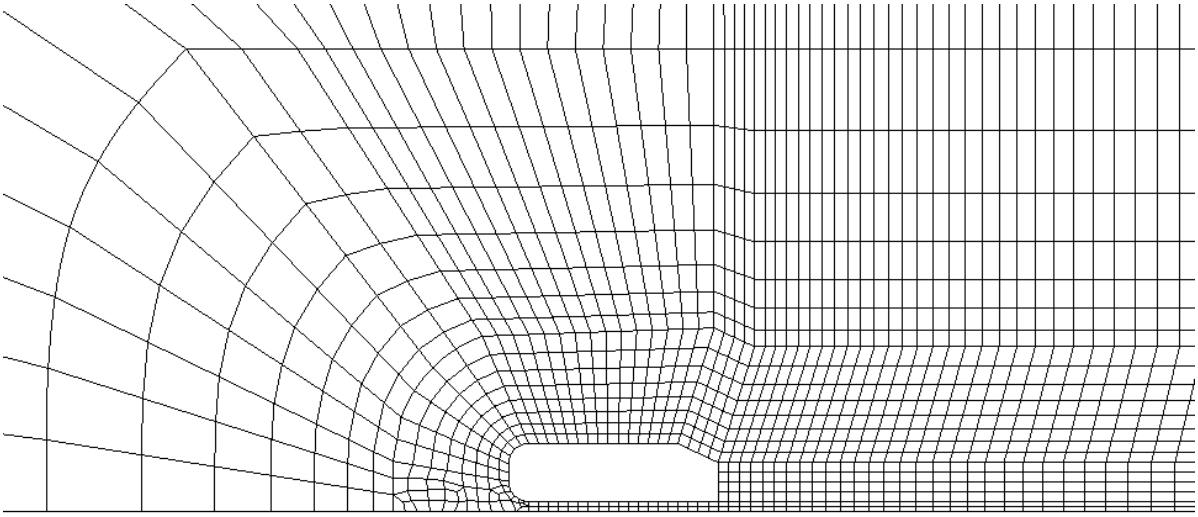

Figure 3.4: Near body mesh topology

into account. The general mesh topology is represented in figure 3.3 and a zoom of the near body mesh is presented in 3.4.

3.2. VALIDATION

In this section the accuracy of the solutions will be discussed. The discussion will be based on 2 main criteria: first the impact of changing mesh resolution will be determined; second the impact of changing the domain size will be established.

The study of the mesh resolution will be performed using two methods, one for the boundary layer and one for the overall resolution of the mesh. For determining the boundary layer accuracy the y^+ of the first element of the mesh is computed and forced to be of order 1. For determining the accuracy of the mesh in the wake, different mesh resolutions are compared.

The study of the domain size will be performed by comparing different solutions with different domain sizes.

3.2.1. MESH RESOLUTION

In wall bounded flows it is crucial to adequately resolve the boundary layer development on the surface of the object of study. Boundary layers are often characterized in three main regions: the inner layer (which depends only on the wall boundary condition), the outer layer (which depends on the outer flow) and the overlap layer. It is generally known that to adequately resolve the boundary layer, the mesh resolution has to be such that the inner layer is accurately represented. To characterize it, non-dimensional wall coordinates (also known as wall units) are generally used. Wall units are defined as:

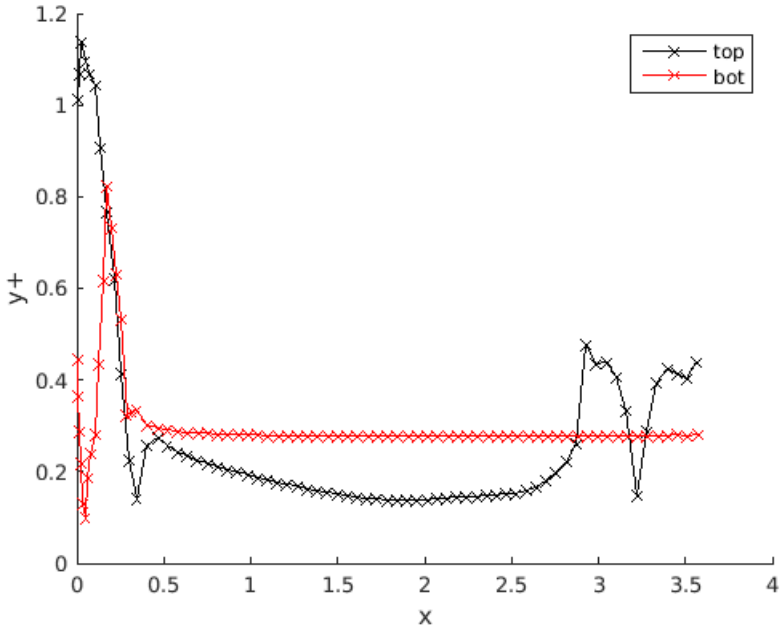

Figure 3.5: y^+ distribution for the top and bottom surfaces of the Ahmed body for Reynolds 550

$$y^+ = \frac{y v^*}{\nu} \tag{3.1}$$

Where:

$$v^* = \sqrt{\frac{\tau_W}{\rho}} \tag{3.2}$$

The inner layer can be characterized in three main sub-layers. The viscous sub-layer ($y^+ < 5$), the buffer layer ($5 < y^+ < 30$) and the logarithmic overlap layer ($y^+ > 30$). The viscous sub-layer is particularly interesting from the simulation point of view because it presents a linear behavior. This is due to the fact that in this region viscous stresses are much larger in magnitude than any other effect. Therefore, to correctly represent this sub-layer at least one point is required.

To take into account the boundary layer resolution considerations the y^+ criterion will be used. This criterion states that if the nearest point of the mesh from the wall is at a distance of order 1 wall unit, then the viscous sub-layer is adequately represented and so is the boundary layer.

Figure 3.5 shows the value of y^+ for the upper and lower surfaces of the model. As stated previously in this section, the goal is to obtain a y^+ of order 1 in all the Ahmed body surfaces. This is achieved in all the domain (see figure 3.5), the maximum y^+ being approximately 1.1 and the minimum being 0.2. The graph is presented for the most critical case, this being the highest simulated Reynolds number (550).

Additionally, to verify that the solution is mesh independent a comparison of different mesh resolutions is performed. Nektar++ is a spectral hp solver, which means that the solution is represented by polynomials of arbitrary order established by the user. As explained earlier in this chapter, the mesh has been designed in three regions of different polynomial order, with the highest order polynomials near the body. The increase of the polynomials can also be referred to as p (polynomial) refinements.

To verify the accuracy of the solution a p refinement has been applied in all the domain. Taking the lowest polynomial of the domain as a reference, the baseline case can be referred to as $p = 4$. The range of polynomials that have been tested is in the range from 3 to 6. To quantify the accuracy the Mean C_L and C_D of the body are compared, as well as the two main frequency peaks of the lift and drag signals. This study has been performed for representative Reynolds numbers of the two main states (periodic and quasi-periodic). In general, in these situations only the case of largest Reynolds number is studied. In this case, however, a number of bifurcations are present near the highest Reynolds number of study, which could potentially question the validity of this study. To compensate for this, two cases have been studied, one at $Re = 525$ which

	Re = 400		Re = 500	
Polynomial order	MEAN CD	MEAN CL	MEAN CD	MEAN CL
3	0.7349	1.5755	0.75671	1.35963
4	0.7306	1.5713	0.75198	1.35745
5	0.7296	1.5699	0.75079	1.3567
6	0.7302	1.5674	0.75059	1.35664

Table 3.1: Effect of the polynomial order on the solution at $Re = 400$ and $Re = 500$

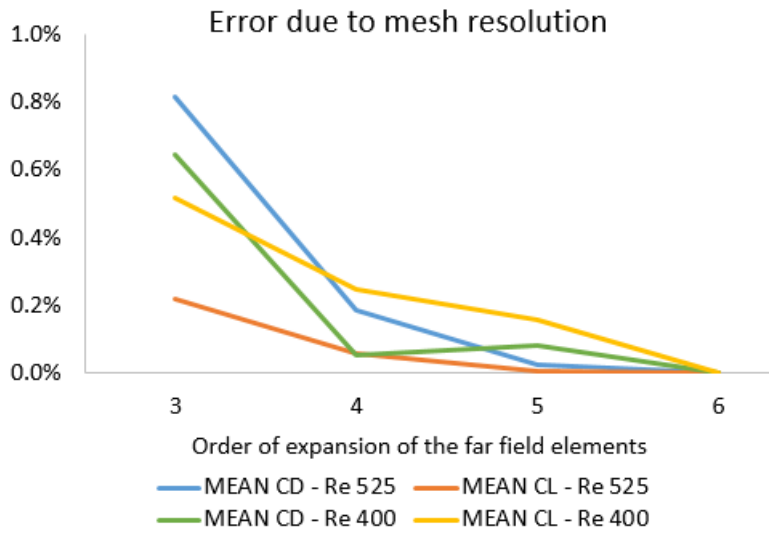

Figure 3.6: Effect of the polynomial order on the solution at $Re = 400$ and $Re = 525$

corresponds to the traditional approach, and one at $Re = 400$, which is not affected by nearby bifurcations. The results are presented in figure 3.6 and table 3.1. The order of the error introduced by the mesh resolution in both cases for average C_l and C_d is lower than 0.5%, which is than other contributions to the global error. The error in the location of the peaks is two orders of magnitude smaller, so it is not presented. The solution type is unaffected by the order of expansion of the mesh. The order of the mesh is therefore considered adequate.

3.2.2. DOMAIN SIZE

It is general knowledge that the domain size can greatly affect the solution due to boundary conditions interference. This is due to the fact that far field conditions do not necessarily apply at the chosen boundary locations, forcing an unphysical solution of the problem. During the literature study performed prior to the start of this thesis the following minimum domain sizes were determined: the inlet should be located at least 10H upstream from the Ahmed body geometry, and that the outlet should be located at least 20H downstream from it. The ceiling location is also recommended to be located at least 10H. To validate these recommendations a study was performed to determine the impact of boundary conditions.

As a starting point the recommended distances were been selected. The inlet and top boundary are expected to have an impact on the base pressure of the Ahmed body geometry, while the outlet conditions are expected to affect the vortex shedding process. Since the focus of this project is put in the study of the vortex shedding process, a convective boundary condition on the outlet has been imposed. This type of boundary condition can be specified in the Nektar++ to reduce instabilities when energetic vortices cross the boundary.

Figure 3.7 shows a diagram of the domain and the parameters that have been varied. L_1 represents the distance from the inlet, H_1 the height of the domain and L_2 the distance to the outlet. A study of the impact of the domain size was performed by varying these three parameters. This study was performed for representative Reynolds numbers of the two main states (periodic and quasi-periodic). In general, in these situations only the case of largest Reynolds number is studied. In this case, however, a number of bifurcations are present near the highest Reynolds number of study, which could potentially question the validity of

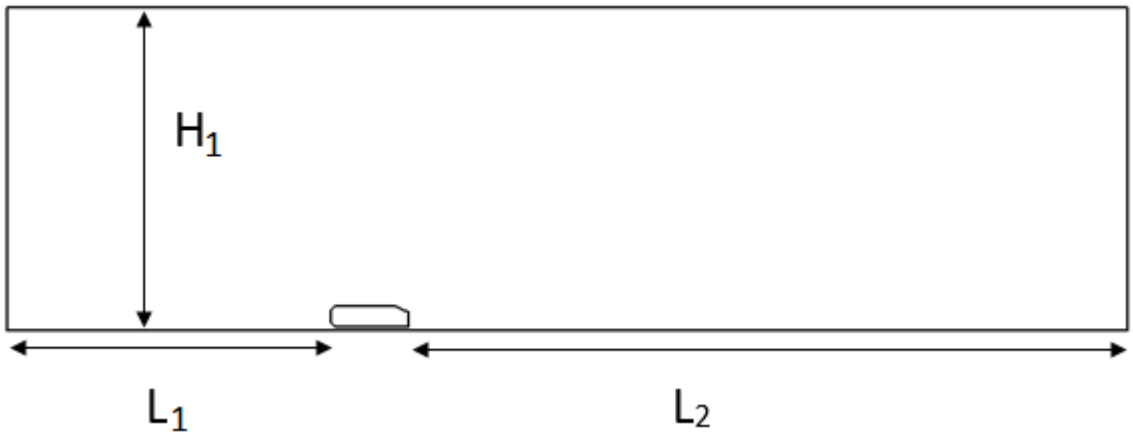

Figure 3.7: Domain dimensions

H_1	L_1	Mean C_D	f_1	f_2	Mean C_L	f_1	f_2
12	8	0.7908	0.0896	0.1792	1.6527	0.0896	0.1792
12	10	0.7657	0.0884	0.1768	1.6224	0.0884	0.1768
12	15	0.7426	0.0875	0.175	1.5955	0.0875	0.175
15	12	0.7438	0.0861	0.1722	1.5894	0.0861	0.1722
15	15	0.7306	0.0855	0.1711	1.5713	0.0855	0.1711
15	20	0.7218	0.0851	0.1702	1.5634	0.0851	0.1702
20	15	0.7253	0.0842	0.1684	1.5632	0.0842	0.1684
25	15	0.7213	0.084	0.168	1.5571	0.084	0.168

Table 3.2: Domain size study for L_1 and H_1 at $Re = 400$

this study. To compensate for this, two cases have been studied, one at $Re = 525$ which corresponds to the traditional approach, and one at $Re = 400$, which is not affected by nearby bifurcations.

As explained in this section the parameters L_1 and H_1 have a strong impact on the base pressure of the body. After performing an initial exploration, it was concluded that since the gradients are of the same order of magnitude, the error introduced by varying both parameters is also expected to be of the same order of magnitude. For this reason both parameters are varied at the same time.

To study the accuracy of the solution 6 parameters have been evaluated. The mean C_d and C_l values and the two main frequencies of the C_d and C_l signals. To adequately compare the solutions it is important to consider that the initial values can have an important effect on the steady state solutions. For this reason the same starting condition has been imposed for all cases. An initial exploration showed that using the proposed values in literature would not be accurate enough at the proposed Reynolds number. Table 3.2 presents an exploration of the most relevant cases that have been compared. The difference between each case and the finest case is presented in figure 3.8 in percentage. This allows to observe that except for a unexpected behavior in the case where $H_1 = 12$ and $L_1 = 15$, al solutions converge towards the finest case. The chosen domain size is $H_1 = 15$ and $L_1 = 15$ which presents a good accuracy while keeping a reasonable domain size. The error with respect to the finest case is of the order of 2%, which is considered acceptable for the present simulations.

The parameter L_2 was varied independently of the other two parameters. The effect of vortical structures on the flow field near the body requires to simulate a large portion of domain downstream of the body. Starting from the recommended values in literature an exploration to determine the impact of the outflow boundary conditions on the solution was performed. Table 3.4 shows the results obtained by increasing and decreasing the outlet distance by $30H$ (approximately 9 vehicle lengths). As in the previous section, the signal has been evaluated at $Re = 400$ and $Re = 525$ to avoid contamination of the results due to the bifurcations. The results are plotted graphically in figure 3.10.

The results show that the error introduced by the outflow distance is one orders of magnitude lower than the error introduced by the parameters L_1 and H_1 for $L_2 > 20H$. Therefore the recommended values deter-

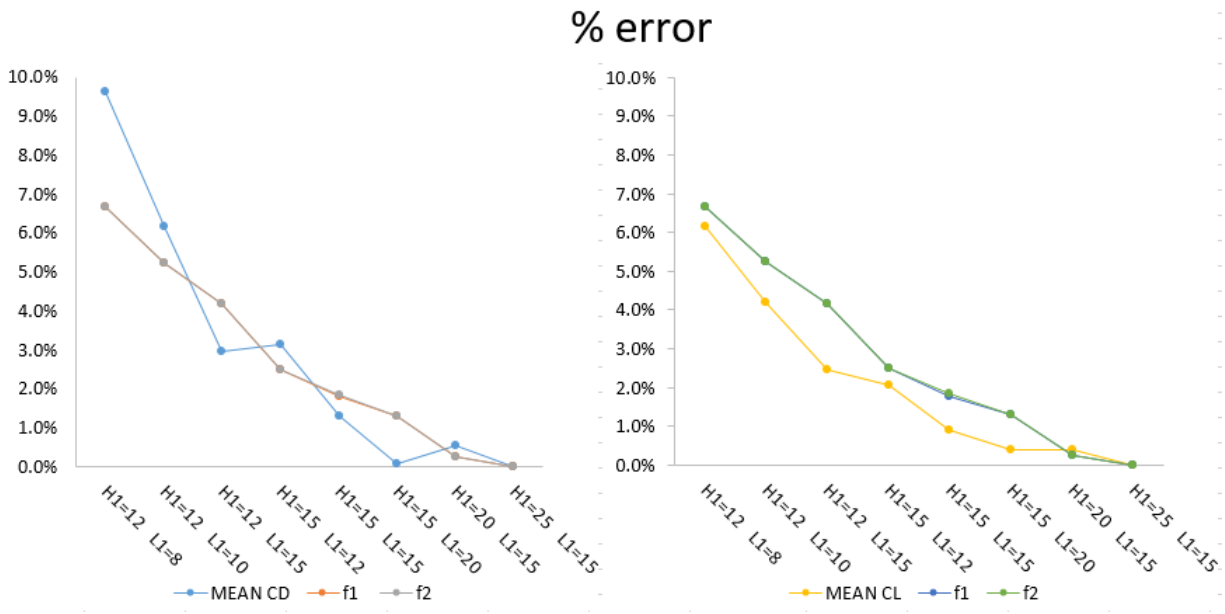

Figure 3.8: Error as a percentage with respect to the finest case for $Re = 400$.

H_1	L_1	Mean C_D	f_1	f_2	Mean C_L	f_1	f_2
12	8	0.8151	0.0933	0.0466	1.4168	0.0933	0.0466
12	10	0.7872	0.0929	0.0464	1.4077	0.0929	0.0464
12	15	0.7635	0.0916	0.0458	1.3875	0.0916	0.0458
15	12	0.8224	0.0954	0.0477	1.441	0.0954	0.0477
15	15	0.7519	0.0895	0.0447	1.3578	0.0895	0.0447
15	20	0.7435	0.0889	0.0445	1.3497	0.0889	0.0445
20	15	0.7448	0.088	0.044	1.3439	0.088	0.044
25	15	0.7432	0.0874	0.0437	1.3354	0.0874	0.0437

Table 3.3: Domain size study for L_1 and H_1 at $Re = 525$

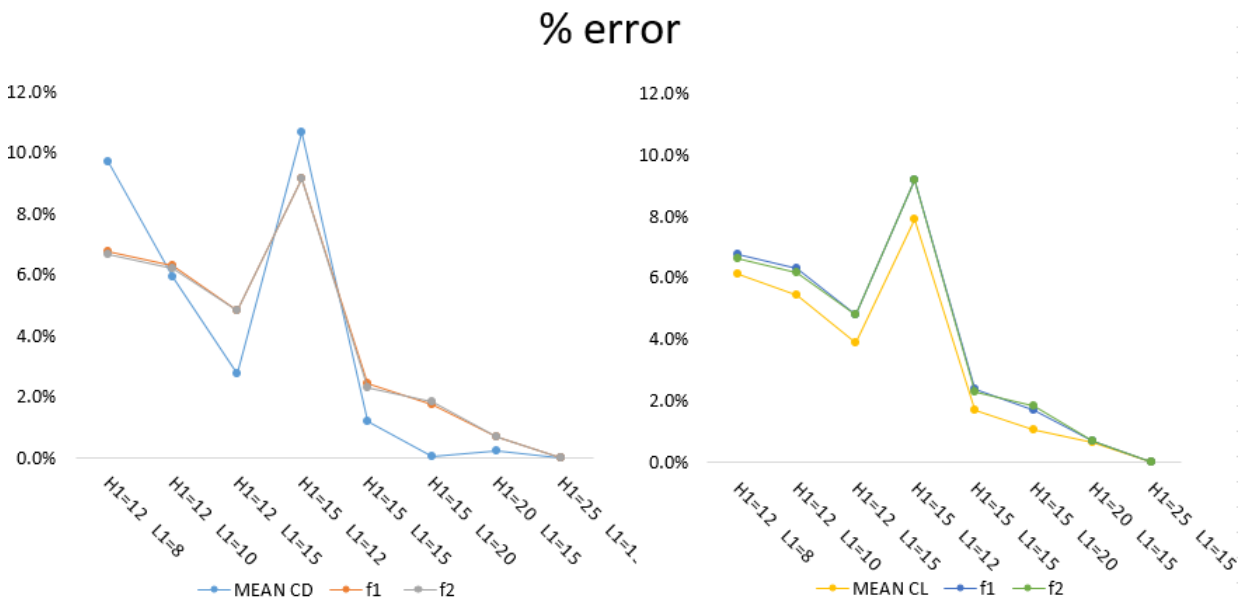

Figure 3.9: Error as a percentage with respect to the finest case for $Re = 525$.

L_2	Mean C_D	f_1	f_2	Mean C_L	f_1	f_2
20	0.7243	0.0835	0.0460	1.4262	0.0823	0.0460
25	0.7516	0.0885	0.0442	1.3481	0.0885	0.0442
35	0.7518	0.0895	0.0447	1.3572	0.0895	0.0447
35	0.7518	0.0895	0.0447	1.3572	0.0895	0.0447
40	0.7517	0.0895	0.0447	1.3576	0.0895	0.0447
45	0.7519	0.0895	0.0447	1.3578	0.0895	0.0447
50	0.7523	0.0893	0.0446	1.3549	0.0893	0.0446
55	0.7526	0.0893	0.0447	1.3536	0.0893	0.0447

Table 3.4: Effect of L_2 on the solution at $Re = 525$

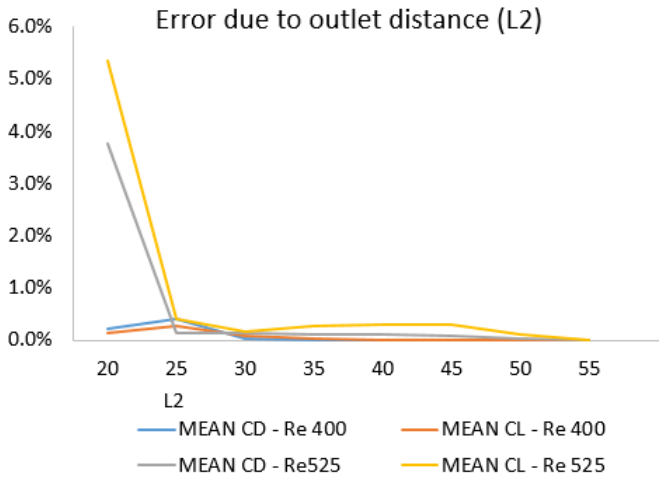

Figure 3.10: Error as a percentage with respect to the finest case for $Re = 525$.

mined in the literature study will be used.

3.3. CONCLUSIONS

In this section the accuracy of the simulations has been assessed. To assess it, two main factors have been studied: the mesh resolution and the domain size. To quantify this accuracy the forces on the body have been monitored. Additionally, to avoid a possible contamination of the results due to the proximity of several bifurcations, two Reynolds numbers have been tested.

First the effect of the resolution has been studied. Two verifications were applied: first, the mesh y^+ was determined to be of order 1 or smaller on the whole domain. Second, a comparison of solutions of different accuracy (through a polynomial refinement) was performed. As a result of these verifications it is possible to conclude that the simulations should be representative of the physics of a the actual case. Obviously this is a 2D case, and therefore this does not imply that the the simulations are representative of the 3D case. This is out of the scope of this work.

Second the impact of the domain size has been assessed. Since unphysical artificial boundaries were imposed to reduce the computational domain this is a key factor. Several distances at which the artificial boundaries are located were tested. This includes the inlet, the outlet and the top boundary. The results proved that for the case of study the recommended distances for the top and inlet boundaries found in literature seem to have a meaningful impact on the solution. For this reason it can be concluded that using a height of the top boundary (H_1) of at least 15 body heights and an inlet distance (L_1) of at least 15 body heights seems to be a better choice. On the other hand the results show that the outlet distance (L_2) has a lower impact on the solution than the other boundary distances. This is probably related to the fact that specific convective boundary conditions have been applied. According to this study, the outlet distance can be reduced up to $L_2 = 25H$ without a loss of accuracy.

4

BIFURCATION ANALYSIS FOR THE BASELINE MODEL

4.1. INTRODUCTION

The goal of this section is to provide information on the bifurcation scheme of the Ahmed body wake. Since several bifurcated states are expected, the goal is to characterize the bifurcations through the study of the different types of solutions. This is performed through the direct numerical simulation of the problem (DNS) until the steady state is reached. Since the Reynolds number is low and the flow is 2D, the computational cost of solving the problem is not very high. However, to study the different types of solutions it is necessary to study the fully developed flow states. For this reason, many time units must be ran, increasing the computational cost. To perform this task, the department of physics of the Universitat Politècnica de Catalunya allowed to run the simulations in their computational cluster.

4.2. DESCRIPTION OF THE FLOW FIELD STATES AND BIFURCATIONS

4.2.1. STEADY STATE

At very low Reynolds numbers the 2D flow is steady and fully laminar. A strong separation on the front upper surface is observed, and the roof of the body presents a separated boundary layer. The flow field is shown in figure 4.1. This type of solution is observed in the range $0 < Re < 220$. This solution can be mapped to a point in the Cl-Cd space.

4.2.2. FIRST PERIODIC STATE

At approximately Re 220 the solution destabilizes, leading to a periodic behavior in the aerodynamic forces. This bifurcation can be therefore identified as a Hopf bifurcation.

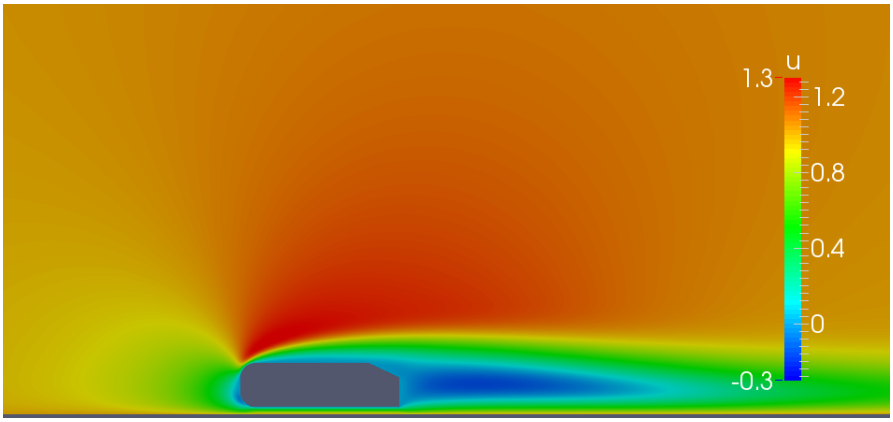

Figure 4.1: Horizontal velocity field at Reynolds 100

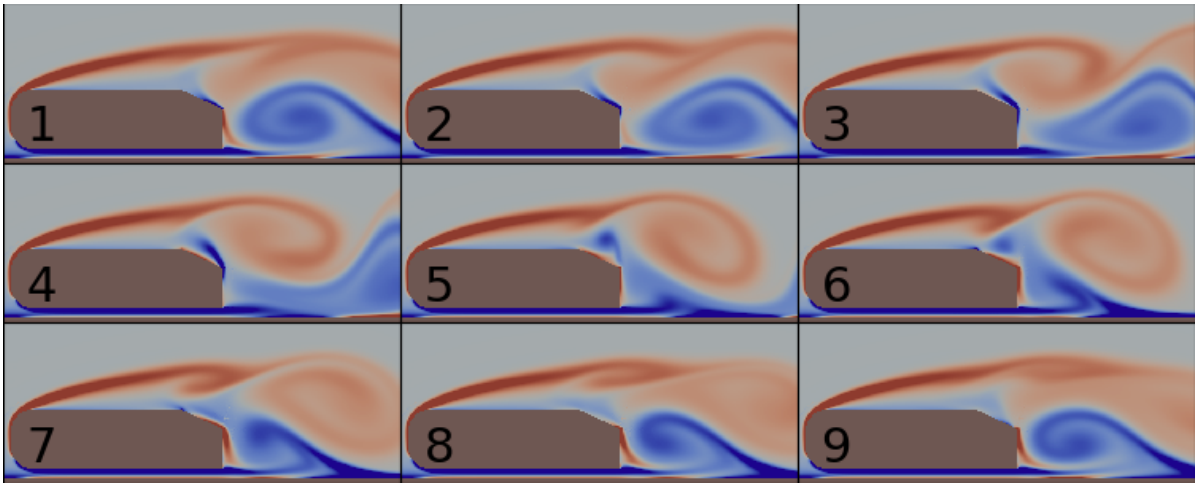

Figure 4.2: Temporal evolution of the vorticity field at Reynolds 500

By plotting the flow fields it is easy to observe that the periodic solution is due to the occurrence of vortex shedding (see figure 4.2). Since the model is not symmetric, neither are the shed vortices. The perfect periodicity is due to the fact that (after the initial transient) all vortices are shed identically. The best proof to this statement can be obtained by plotting the long term behavior of the Cl-Cd map, which closes on itself perfectly. It is presented in figure 4.4a.

The vortex shedding frequency has been established as approximately 0.083Hz. This frequency remains unchanged in the range $220 < Re < 500$. The Fourier transform of the lift coefficients can be used to prove this statement, and is presented in figure 4.4b.

The amplitude of the vortex shedding phenomenon highly depends on the Reynolds number. Starting from a 0 amplitude at Reynolds 220, it grows until a new bifurcation is observed.

4.2.3. SECOND PERIODIC STATE

At approximately Reynolds 520 a new bifurcation occurs and a new periodic solution is observed. The new periodic solution is particularly interesting for two reasons: first of all the new state is radically different from the previous solution, indicating a saddle node bifurcation. At the critical point, the original periodic solution becomes unstable, forcing the system towards a new stable solution. On the other hand, the new solution presents a new natural frequency, which is exactly half of the vortex shedding frequency. This indicates a period doubling bifurcation. Surprisingly, the vortex shedding frequency has been affected, and the peaks are slightly displaced in the frequency domain. The variation is of the order of 10%, and could be related to the saddle node bifurcation that occurs at the same time. This bifurcation cannot be directly identified as one of the normal form bifurcations because the two flow states that are being analyzed are not the result of a single effect. The destabilization of the original solution generates a new unstable branch that links the two stable branches. This branch is particularly interesting because it appears in the range $500 < Re < 520$. Therefore in this region 3 solutions coexist: two of which are stable, the other being unstable. This phenomenon is also known as hysteresis, and the initial conditions of the problem are the key factor that determine towards which solution the problem will tend to. The study of the unstable branch can bring more light to how the two bifurcations occur and will be performed in section 4.3

The second periodic state consists in the shedding of two different types of vortices, one which is larger than the vortex that was observed at $Re = 500$ and one that is smaller. Therefore contrarily to the first periodic state, in this case the vortex shedding periodicity occurs after two vortices have been shed. This can be easily observed in figure 4.3: each half period is represented in six snapshots. Therefore snapshots 1 and 7 are at the same phase of the cycle, 2 and 8 as well, etc. This allows to observe that during the first half period the rear base vortex is much larger than in the second half period. In the C_l-C_d map shown in figure 4.4c this is clearly observable as there are two branches, one which has a large amplitude ($C_d \in (0.2, 0.5)$), and one which has a much smaller amplitude ($C_d \in (0.3, 0.45)$).

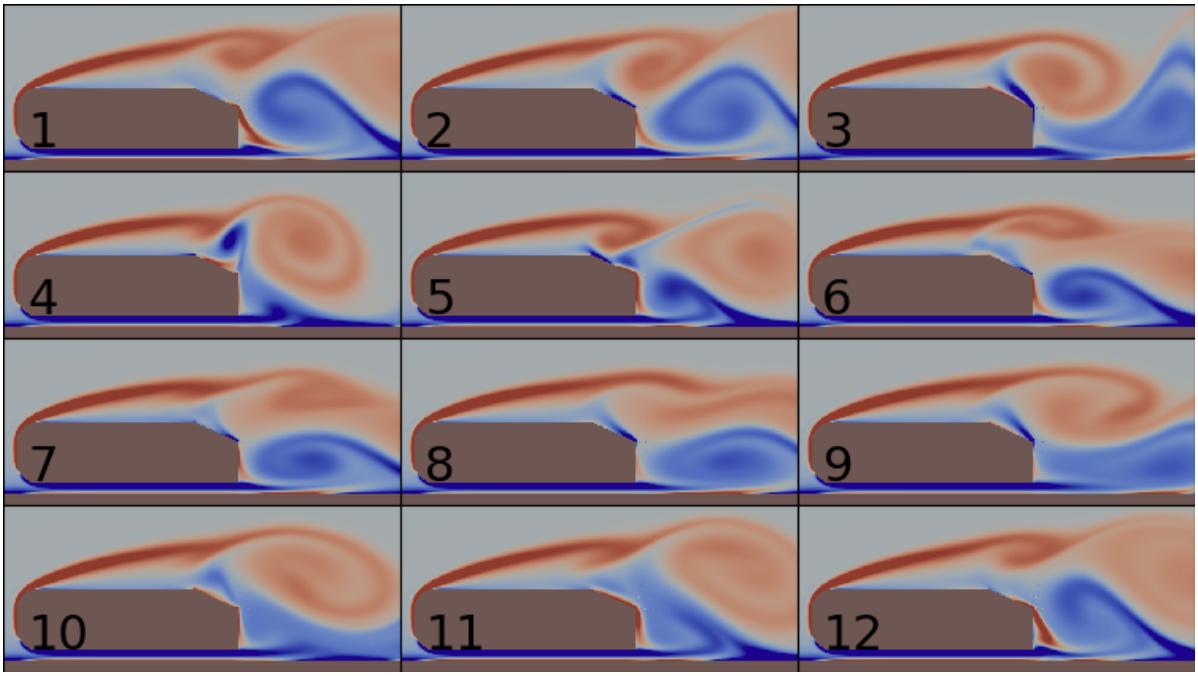

Figure 4.3: Temporal evolution of the vorticity field at Reynolds 520

4.2.4. QUASI-PERIODIC STATE

At approximately $Re = 525$ a new bifurcation occurs, leading to a quasi-periodic state. The Cl-Cd map of this type of solution is shown in figure 4.4e. In this state a new frequency occurs, which is incommensurable with respect to the vortex shedding frequency. For this reason the solution only closes after a number of vortex shedding cycles.

The Cl-Cd map is not the most useful tool for the study of quasi-periodic solutions. Instead Poincaré section maps allow to better study this kind of solutions, and allow to compute the new incommensurable frequency. Alternatively, it can also be determined by analyzing the Fourier transform of the signal. Both methods will be presented in section 4.4.

4.2.5. CHAOTIC STATE

By further increasing the Reynolds number ($Re > 540$) a great amount of noise appears, making the solution even more complex. However, vortex shedding remains the most relevant phenomenon, and therefore the Fourier transform of the signals maintain a peak at that frequency and at its harmonics. The incommensurable frequency also remains as a relevant phenomenon, also maintaining a peak at this Reynolds number. However, the solution does not exhibit any kind of periodicity. No substantial quantitative changes can be observed in the forces applied to the body (see figure 4.4c), which indicates that the wake topology has not been substantially affected by the destabilization of the periodic orbit.

In figure 4.5 the long term temporal evolution (initial transients have been suppressed) of the lift coefficient signal for $Re = 500$, $Re = 510$ and $Re = 550$ is presented to show the difference between the periodic, period two and chaotic types of solutions. The results confirm that the chaotic solution seems to be attracted by the period two orbit. This is consistent with the destabilization of a new mode, the amplitude of which is small compared to the main modes that drive the problem (vortex shedding and its subharmonic frequency). $Re = 525$ is not presented as it seems chaotic to visual inspection. This is because the periodicity occurs after a large number of cycles. This will be further discussed in section 4.4. The steady solution is also not presented as it is a line of constant C_l.

4.2.6. COMMENTS ON THE VALIDITY OF THE MODEL

The early separation on the front region represents a large difference between the model behavior and the expected high Reynolds behavior. This is particularly problematic because it is not possible to actuate on a separated boundary layer, which implies that an active flow control placed in the rear slant will not be

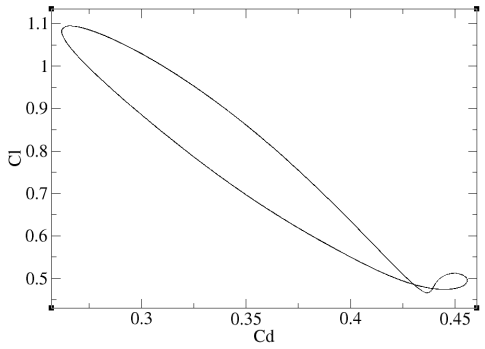

(a) Map of the aerodynamic forces at $Re = 500$ (first periodic state)

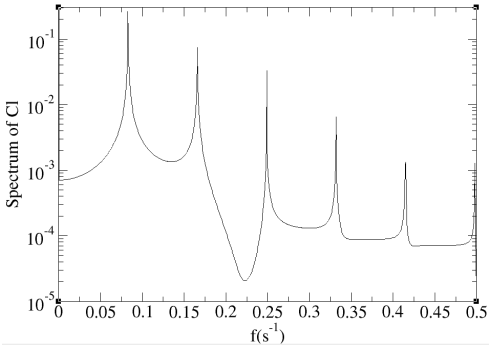

(b) Fourier transform of the lift coefficient at $Re = 500$ (first periodic state).

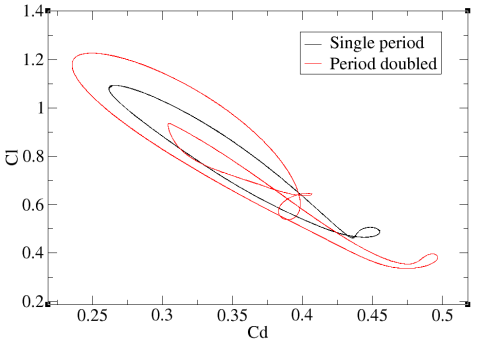

(c) Map of the aerodynamic forces at $Re = 510$. Two possible solutions can be obtained (one corresponds to the first periodic state (black) and the other one to the second periodic state (red))

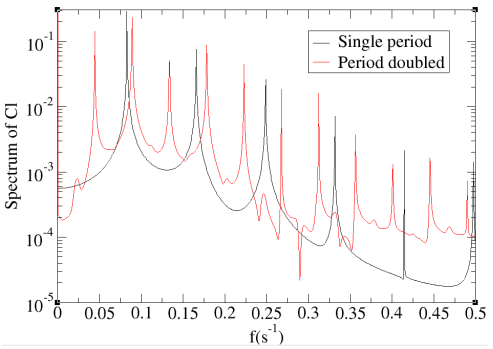

(d) Fourier transform of the lift coefficient at $Re = 510$ (first periodic state).

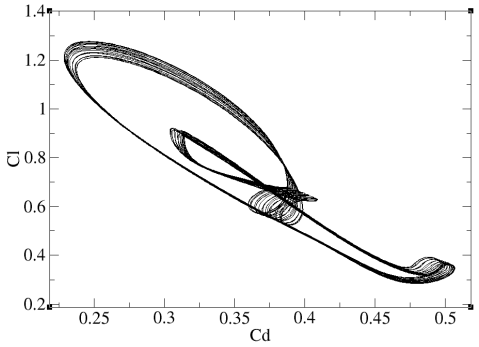

(e) Map of the aerodynamic forces at $Re = 525$.

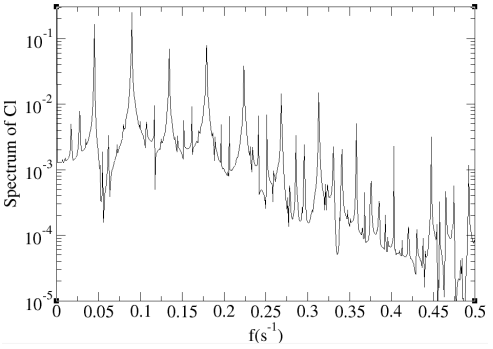

(f) Fourier transform of the lift coefficient at $Re = 525$.

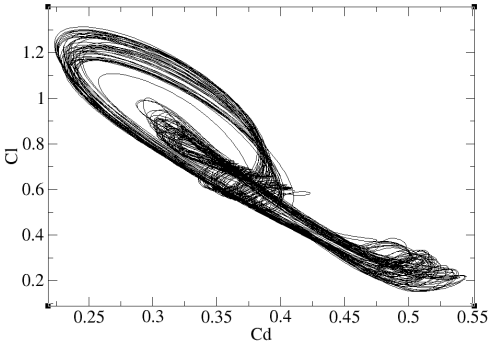

(g) Map of the aerodynamic forces at $Re = 550$.

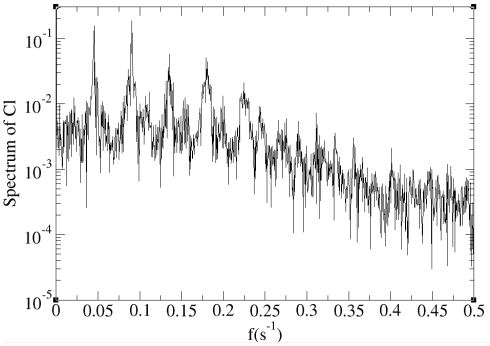

(h) Fourier transform of the lift coefficient at $Re = 550$.

Figure 4.4: Summary of the different types of solutions

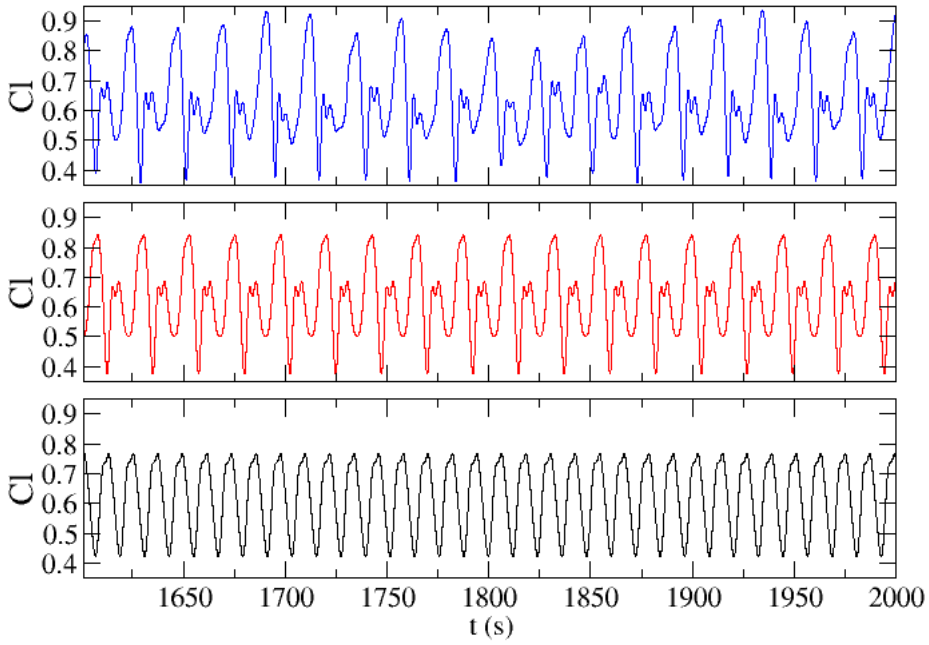

Figure 4.5: Comparison of the time evolution of the lift signal for $Re = 500$ (black), $Re = 510$ (red) and $Re = 550$ (blue)

effective. To solve this problem several possibilities can be considered:

1. Applying a suction in the front region to suppress separation: The application of a flow control on the front top region can be used to suppress the early separation and produce a model that resembles more the case of interest. This solution has the advantages of not altering the geometry and producing a case that is similar to the higher Reynolds behavior, but will alter the bifurcations scheme that has been studied. The philosophy of this solution is somewhat similar to the boundary layer tripping technique (that is usually applied to wind tunnel experiments). This technique consists in forcing the transition of the boundary layer at a given location to mimic what occurs at higher Reynolds. Similarly, in this case the boundary layer separation is suppressed.

2. Redesigning the front region to prevent separation: Similarly to the previous solution this will produce the desired flow behavior. However it has the added inconvenient of introducing a geometry change, which makes it less comparable to the original geometry as well as being complicated to perform (different Reynolds number may require different curvatures).

3. Applying the AFC on the front region: This solution consists in accepting the new problem and adapting the control strategy to it. However the problem will not be comparable to higher Reynolds scenarios.

Having considered all the options, the first solution is considered to be the most optimal. This is due to the fact that it does not require any modification to the geometry and allows for a reasonable comparison with the higher Reynolds cases in which AFC in the rear slant are effective.

4.3. STUDY OF THE HYSTERESIS REGION USING EDGE TRACKING

In the study of the different states, the region of $500 < Re < 520$ has been found to be particularly interesting due to the fact that two stable solutions can coexist. This phenomenon is also known as hysteresis. The key parameter in determining towards which solution the case will tend to are the initial conditions. Figure 4.4c presents the two types of solutions that are obtained at Re 510.

The justification for the study of this region is that the bifurcation that separates the two states is not a simple bifurcation, instead two bifurcations occur. On the one hand the transition from one to the other is not smooth, indicating a saddle node bifurcation. On the other hand, the new state presents a new frequency which is one half of the original vortex shedding frequency, which indicates a period doubling bifurcation. Then, three possible scenarios can occur:

1. First the period doubling bifurcation occurs, then this solution bifurcates immediately again, and the unstable branch is born period doubled.

2. First the saddle node bifurcation occurs, the unstable branch is not period doubled and the period doubling occurs on the new stable branch.

3. First the saddle node bifurcation occurs, then the period doubling bifurcation occurs on the unstable branch.

4.3.1. EDGE TRACKING TECHNIQUE

Edge tracking is a technique that targets to determine the nature of an unsteady solution by modifying the initial conditions of the problem. As a starting point two converged stable states of the two types of solutions are required. The method consists then in generating an array of new initial conditions and determining towards which final state they will tend. The unsteady branch will therefore be located in the subregion between the two closest initial conditions points that tend to different solutions. To produce the array of initial conditions the parameter space between the two solutions is discretized. The accuracy of the unsteady branch properties will the be determined by the distance between the starting conditions of the simulation and the unstable branch. As a general rule the attraction towards the stable solution decreases when the initial conditions are placed closer to the unstable branch. This implies that by increasing the accuracy of the location of the unstable branch, the solution will remain closer to it for a larger number of periods.

Figure 4.6 aims to clarify this process. It consists of a hysteresis region map where two stable solutions (or states) (solid line)coexist. If this is the case, then they must be separated by an unstable branch of solutions (dashed line). The dashed line separates the basin of attraction of the two stable solutions. This implies that if a solution starts between the unstable solution and one of the stable solutions, then it can only tend to that solution. For a fixed Reynolds this implies that it can only go "up" or "down" in the diagram. The edge tracking method consists in placing a number of initial conditions in this region and determining towards which stable solutions they tend to. By doing so the location of the unstable branch can be pinpointed to a certain accuracy, which depends on the spacing resolution. Producing a solution that will remain near the unstable branch indefinitely is impossible due to the obvious limitations in simulation capability and costs. However, it is possible to produce initial conditions such that the solution will remain close to the unstable branch for a sufficient amount of time such that the properties of this branch can be studied. This, however requires a fine discretization of the initial conditions space. If the initial conditions space were to be equally spaced this would require a great amount of simulations to be run. To minimize the computational cost of this process the discretization of the space should not equal, but instead it should be finer in the region close to the unstable branch. The most optimal method to discretize the problem in terms of computational time is the bisection method which consists in splitting the space in two, determining in which of the two subspaces the branch has fallen, and then repeating the process in the subspace of interest until the desired resolution is reached. However this procedure is far from being optimal from the simulation time point of view, since only one job is being run at a time. To speed up the process the arbitrary number of 9 equally space points is placed and the region between the two closest points which tend to different solutions is chosen as the new region of interest.

4.3.2. RESULTS

The two stable solution types at $Re = 510$ are shown in figure 4.7. One flow state from each solution is chosen and 10 interpolated flow states are computed. This procedure is repeated 4 times until the unstable solution is clearly observable (several periods can be observed before the solution tends to one of the stable solutions). The unstable branch is observed as the limit cycle that separates the two closest initial conditions that tend to different stable solutions. In this case, the two solutions are represented in blue and orange. Since this curve has two branches, it is possible to state that the unstable solution is period doubled.

Period doubled solutions can be understood as if the problem tries to follow the original period but is unable to close after the full cycle. Instead it deviates from the initial conditions and can only return to them after two cycles. By taking the Poincaré section of this solution it is possible to clearly observe two points, which represent the difference between the two states that are possible after n cycles. By measuring the distance between these two points a period doubling amplitude can be determined. The PD amplitude of the unstable branch at $Re = 510$ is determined to be approximately 50% of the PD amplitude of the stable branch.

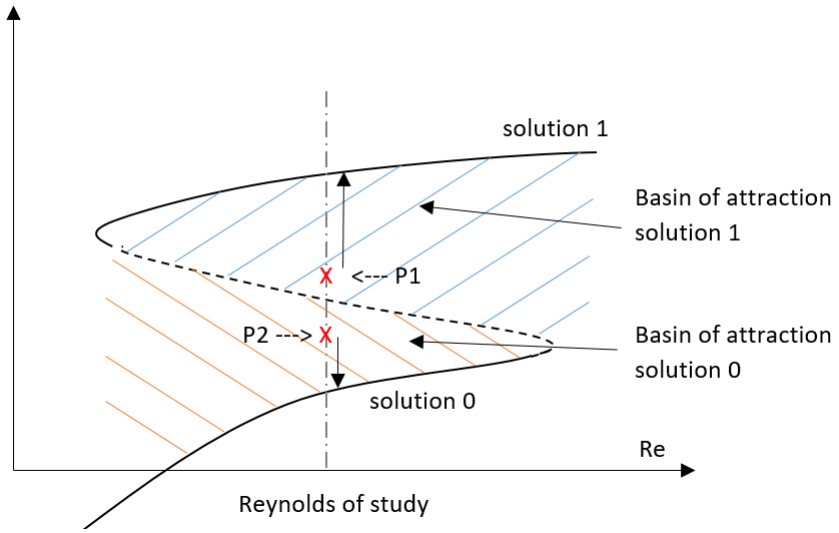

Figure 4.6: Schematic description of the edge tracking method

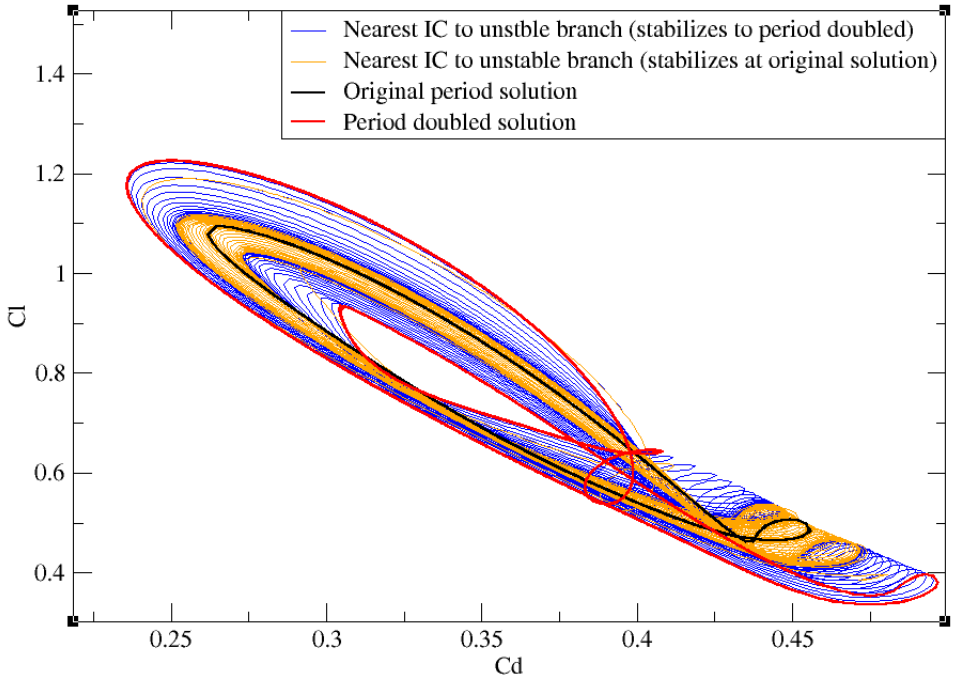

Figure 4.7: Application of edge tracking at $Re = 510$, unstable solution can be found in the region comprised between the blue and orange line

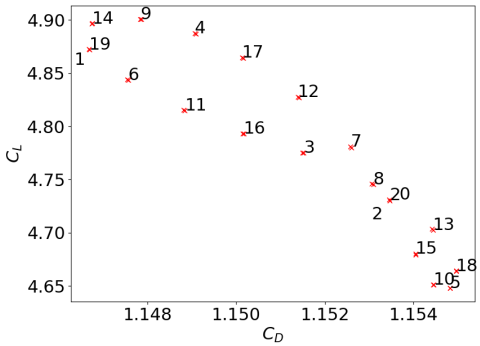

(a) Poincaré map of the solution at $Re = 525$.

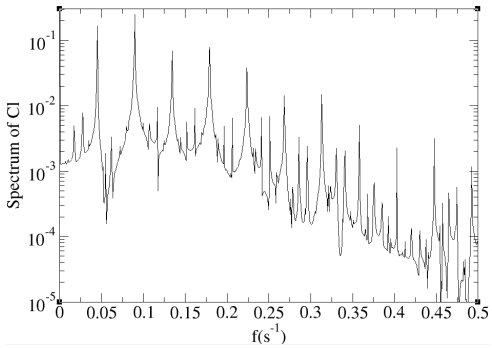

(b) Fourier transform of the lift coefficient at $Re = 525$.

Figure 4.8: Analysis of the quasi-periodic solution at $Re = 525$

4.4. STUDY OF THE QUASI-PERIODIC STATE

The study of the quasi periodic state can be performed using the Poincaré section method, which consists in evaluating making a Cl-Cd map of the solution when a third variable is constant. In this case the viscous drag has been chosen as the constant variable. In this graphical method, the viscous drag is used to determine the "periodicity" of the signal and therefore the time length of a vortex shedding cycle. By plotting the Cl-Cd after each vortex shedding cycle it is possible to observe that after 18 cycles the solution closes on itself as shown in figure 4.8a (points 1 and 19 overlap and the same occurs with points 2 and 20). Furthermore, the points do not fully fill the circle, instead only 18 discrete positions are valid (in figure 4.8a 50 red crosses are being plotted). This clearly indicates that the solution is quasi-periodic. On the other hand the solution closes 7 or 10 (depending on the rotation direction that is taken into account) laps to complete the Poincaré map. Therefore the incommensurable frequency is 7/18 or 10/18 times the vortex shedding frequency (0.033 and 0.046).

The Fourier expansion of the signal presents peaks at the location of each of the two main frequencies, and also at the location of all the linear combinations of the two frequencies. Therefore the incommensurable frequency must be the location of one of the peaks, such that the location of all the other peaks can be written as a linear combination of it and the vortex shedding frequency. The best frequency estimate that has been obtained by using this method is 0.036. This coincides with a good accuracy with the estimation of Poincaré section method (0.033) with an error margin of 10%.

4.5. QUASI-3D APPROACH

The results presented in this work are 2D in general, however it can be interesting to determine whether the problem would be stable if it had been imposed to be 3D. To do so the program Nektar++ allows to perform a study of the growth of perturbations in the third dimension by applying a purely spectral expansion in the Z direction and applying periodic boundary conditions. This expansion can be imposed to have any arbitrary number of modes, effectively allowing to simulate the three dimensionality of the problem. However this can be extremely costly, as running the 3D simulation will greatly increase the number of computational points as the number of modes are increased. To obtain an estimation of the stability of the 3D case without performing a purely 3D simulation the quasi-3D approach can be applied. In this type of simulation only two modes are imposed in the third dimension: mode 0 represents the 2D simulation and mode 1 represents the instability of the 2D simulation in the third dimension. By varying the length of the domain in Z it is possible to determine if a certain perturbation of the length scale of L_Z would grow or decay. If the perturbations decay for all length scales, then the 2D simulation can be considered representative of the 3D case. If they grow, then the most energetic length scale of the quasi-3D approach (the one which grow faster) is the most likely length scale to destabilize in the fully 3D problem.

A quasi 3D approach has been applied to the model to determine if the different periodic solutions observed in the 2D problem are stable in a 3D case. Perturbations of the order of 10^-6 are applied to the converged states in the form of velocity in the Z direction. This order of perturbation is chosen as it is halfway between the machine precision and the maximum velocity. Unfortunately for all periodic solutions the perturbations grow for length scales of the order of $L_Z \approx 10^0$, which indicates that they are not stable in 3D. The same approach is then applied to the steady solution before the first bifurcation to determine if this

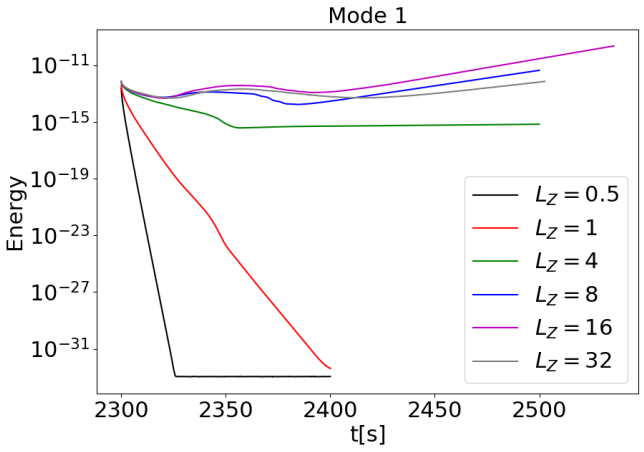

Figure 4.9: Temporal energy of Mode 1 in the quasi-3D simulation of the problem at $Re = 200$

flow topology can be representative of the 3D case. This type of solution is also unstable, indicating that the steady solution is not stable in a 3D environment either. The modal energy of mode 1 (which corresponds to the component of the energy in Z) is presented in figure 4.9 for this type of solution ($Re = 200$). For $L_Z < 4$ the perturbations are observed to decay, while for $L_Z > 4$ they grow after an initial transient. The fastest growing lengths is $L_Z = 16$. This supports the idea that the model is not representative of the 3D flow, and gives an idea of order of magnitude of the first scales to destabilize, which will lead to a new 3D state.

4.6. SUMMARY AND CONCLUSIONS

In this chapter the different types of flow states that were observed experimentally (using DNS) were described. The transition from steady laminar behavior to chaotic pre-turbulent behavior was characterized. Three main states were observed: first a periodic state, second a periodic state of double period, third a quasi-periodic state and finally a chaotic solution.

The study of the second periodic state allowed to determine that there is a region where both the first and the second periodic state coexist, which is also known as a hysteresis region. This implies that the bifurcation that separates the two states must be a supercritical bifurcation (a bifurcation by which the previous stable solution becomes unstable). The study of the unstable branch revealed that it is also period doubled.

The study of the quasi-periodic state revealed that this regime is governed by two main frequencies, the vortex shedding frequency and a second frequency. The study of the Poincaré map of the solution allowed to determine that a sub-critical Neimark-Sacker has occurred. The new frequency has been determined by using two different techniques.

After the quasi-periodic state the last state could not be identified clearly. Its behavior seems to be chaotic although the vortex shedding frequency and the new-born frequency guide the new phenomena. This scenario is consistent with a cascade of Neimark-Sacker bifurcations. In this scenario, it should be possible to find a new state in which only three incommensurable frequencies are observed. However, this was been attempted for three reasons: first, it is difficult to find a new state that presents these properties(the distance between bifurcations is reduced with each bifurcation); second, it is not trivial to identify the third frequency even if the state is found; third, there is no particular interest in determining the value of the third eigenmode.

The study of the flow fields showed, however, that it does not present the desired flow features. This is due to an early separation of the top surface boundary layer in the front region of the body (which does not occur at higher Reynolds). As explained, this could be related to the 2D nature of the simulation, which does not allow the instabilities in the third dimension to grow and force a new equilibrium. This has the unexpected consequence of negating the effect of the AFC on the rear slant of the vehicle.

To solve this unexpected issue a new model is proposed. The new model consists in applying a suction on the front region of the top surface of the body. This will prevent the early separation of the boundary layer, making the model comparable to the higher Reynolds flow fields and allowing for the rear region flow control to be effective. This has been determined to be the least intrusive solution to the problem. This new model will be discussed in the second part of this thesis

5

THE MODIFIED AHMED BODY CONFIGURATION

5.1. CHANGES TO THE MODEL

The conclusions of the first part of this thesis were that the original model of study is not valid for the application of AFC on the rear slant. Therefore the model must be modified in such a way that it allows to study the rear slant phenomena. To do so, the top boundary layer early separation must be suppressed. The least intrusive way to obtain the desired results is to introduce a suction to the front top part of the roof (see figure 5.1). This introduces 2 obvious effects on the model and 1 that is not so obvious. First of all, the resolution of the mesh must be increased in the actuation region to account for the the new phenomena. The second obvious change is that a new boundary condition must be imposed in the actuation boundary, however the amplitude of the suction is not so clear. Finally the least obvious effect on the problem is that when an adequate suction is applied, the periodic state of the flow is maintained until much larger Reynolds numbers. As a matter of fact the chaotic behavior is observed at Reynolds that are almost of the order 10 times larger than the one at which chaotic behavior was observed when suction is not applied. The new model that was been designed for this section must take into account these three phenomena and at the same time the experience obtained from the first part of this work.

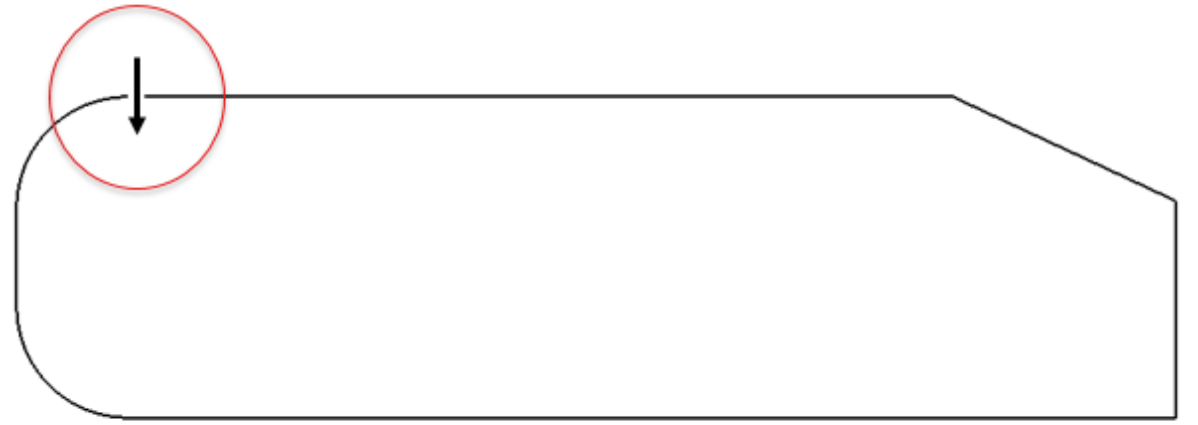

Figure 5.1: Schematic representation of the front actuation

The increase in the Reynolds number requires a drastic change in the design of the mesh. At Reynolds of the order of 10^3 the boundary layer at the top wall will require a special treatment to keep the y^+ of the problem in the order of one. Also, the resolution of the mesh in the wake mush be greatly increased. Furthermore, reducing the mesh size forces the time-step to be reduced to prevent the solution from diverging from

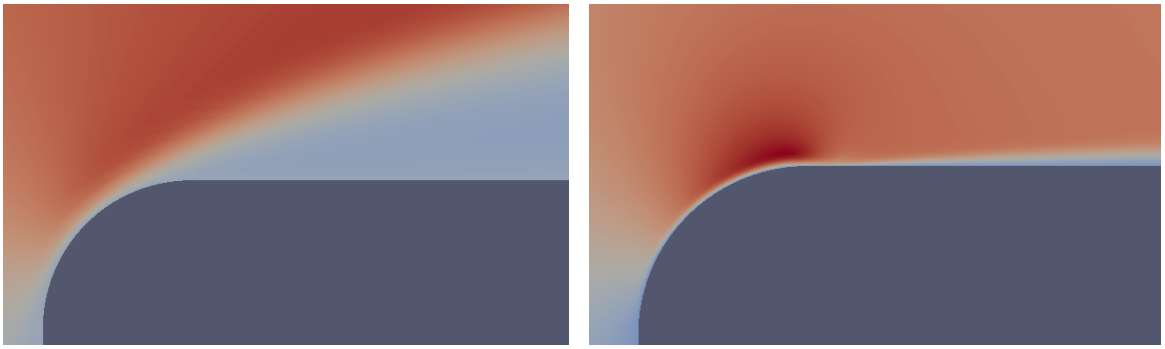

(a) Flow on the top roof before flow control (b) Flow on the top roof after flow control

Figure 5.2: Comparison of the flow features with and without flow control

numerical instabilities (respecting the CFL condition). This implies that the computational cost will greatly increase. To reduce the computational cost of the problem two actions have been taken: the domain size has been reduced and the meshing philosophy has been drastically changed.

5.1.1. CHANGES TO THE DOMAIN SIZE

In chapter 3 it was shown that using convective boundary conditions the impact of the outlet was minimal compared to the impact of the other boundary conditions. This was confirmed for lengths greater than 20H. Taking advantage of this fact, and with the goal of reducing the computational cost of the simulation, the outlet distance is reduced to 25H. The rest of dimensions has been kept the same, respecting the results of the domain size study performed in the previous part.

5.1.2. CHANGES TO THE MESH TOPOLOGY

To maintain the y^+ criterion the mesh density must be increased. To avoid increasing the mesh density in great measures the height of the elements is set to decrease in the near-wall region. To maintain a reasonable aspect ratio the width of the near wall elements is also reduced. Finally, to reduce the element count of the domain an unstructured algorithm is chosen for the far field. The number regions of the far field is reduced to 1, so therefore to maintain the order of the polynomials in the boundary layer and wake, the far field order of polynomial is increased to 6. To maintain the vortical structures inside the high resolution region the wake separation line is given a certain angle. A scheme of the mesh topology is shown in figure 5.3. Additional resolution is added near the AFC location. A zoom of the mesh near the body is shown in figure 5.4

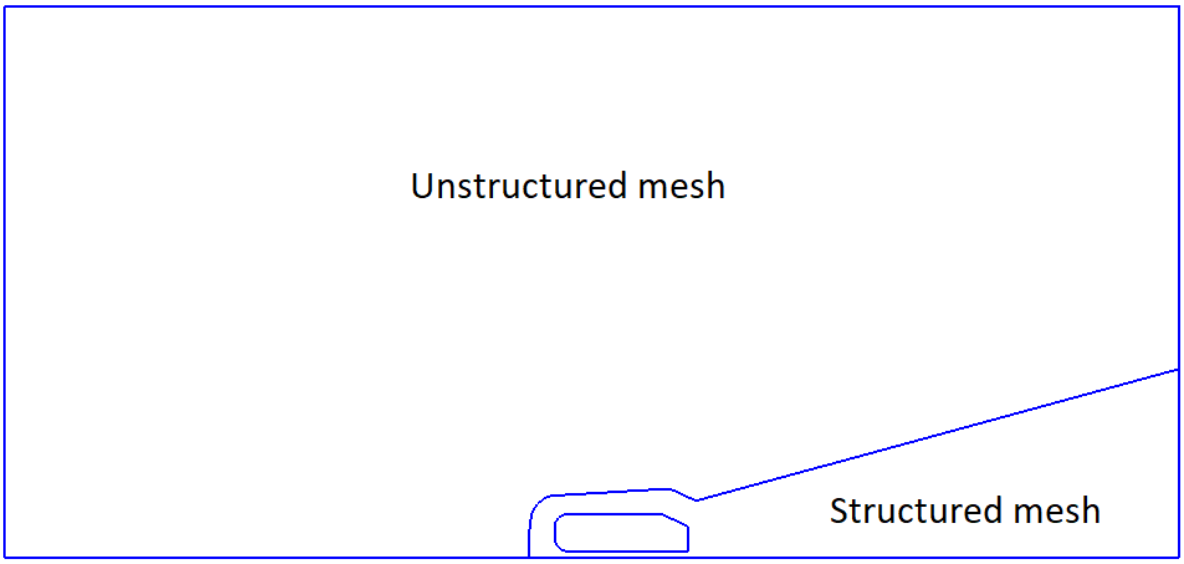

Figure 5.3: New mesh partitioning scheme

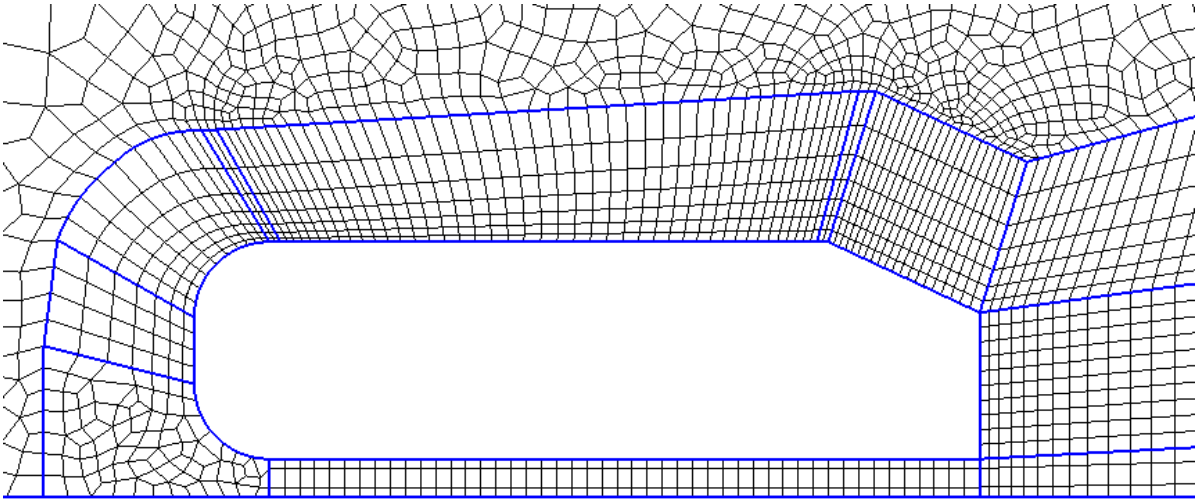

Figure 5.4: Detail of the new mesh near the body

5.1.3. CHANGES TO THE BOUNDARY CONDITIONS

The changes to the boundary conditions are exclusively applied to the flow control surface. The Ahmed body top surface has been split, and a region of approximately 5% of L has been selected for actuation. The suction amplitude has been set to 30% of the inlet velocity. This value has been set after some extensive testing at the Reynolds range of interest. Higher values do not provide any advantage and can generate numerical instabilities due to the high velocity in the front region, which require reducing the time-step. On the other hand reducing the suction amplitude can lead to not being able to reattach the boundary layer. It is interesting to note that this constraint decreases when the Reynolds number is increased. In the range of $1000 < Re < 5000$ the value of 30% of the inlet velocity has been judged adequate.

5.2. RESOLUTION

5.2.1. y^+ CRITERION

Similarly to what was done in the first model to take into account the boundary layer resolution considerations the y^+ criterion will be used. This criterion states that if the nearest point of the mesh from the wall is at a distance of the order 1 wall unit, then the viscous sub-layer is adequately represented and so is the boundary layer.

Figure 5.5 shows the value of y^+ for the upper and lower surfaces of the model. As stated previously in this section, the goal is to obtain a y^+ of order 1 in all the Ahmed body surfaces. This is achieved in all the domain, the maximum y^+ being approximately 2.1 and the minimum being 0.4.

5.2.2. OVERALL RESOLUTION

The study of the resolution will be presented for $Re = 3750$ as it is the Reynolds that will be used for the case of active flow control. Similarly to what was presented for the model from part 1 the mesh resolution will be evaluated by comparing the total forces on the vehicle by varying the polynomial order of expansion of the mesh. The near wall mesh polynomial order of expansion is varied in the range $6 < P_{order} < 10$. The error of the mean Cl and Cd of steady state solution is presented in figure 5.6a, and the mapping of the solutions in figure 5.6b. Note that for $P_{order} = 6$ the graph is significantly thicker (the solution is not periodic). Therefore it is possible to assume that resolution is not sufficient. It is also interesting to note that for the lowest odd order of expansion ($P_{order} = 7$), the error is significantly larger than for all other cases, which seems to indicate that there is an error in this case. In fact some unphysical oscillations are observed in the Cl-Cd map for all odd orders of polynomial expansion (but are attenuated with increasing polynomial order). These oscillations are not observed for lower even orders of expansion, indicating that perhaps odd orders of expansion are less stable in this type of code. 8 is the lowest order of expansion that is deemed acceptable from the results, which is in good agreement with the y^+ criterion, which indicated that for this order of expansion $y^+ \approx 1$ for all the body. The mesh resolution is considered acceptable because by increasing the polynomial order of

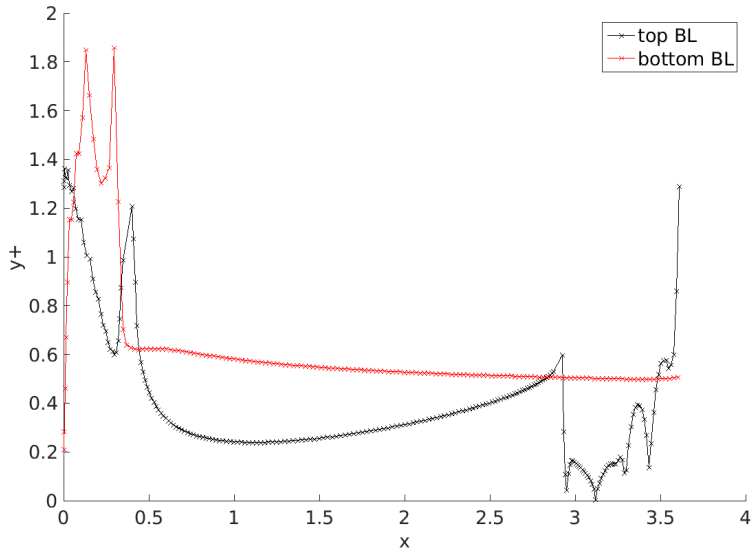

Figure 5.5: y^+ distribution for the top and bottom surfaces of the Ahmed body for Reynolds 3750

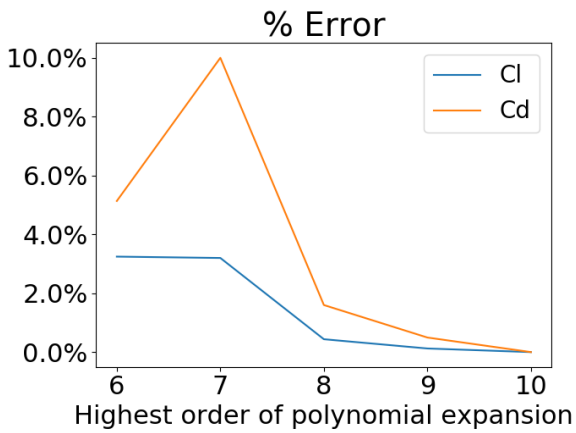

(a) Average error of the solution

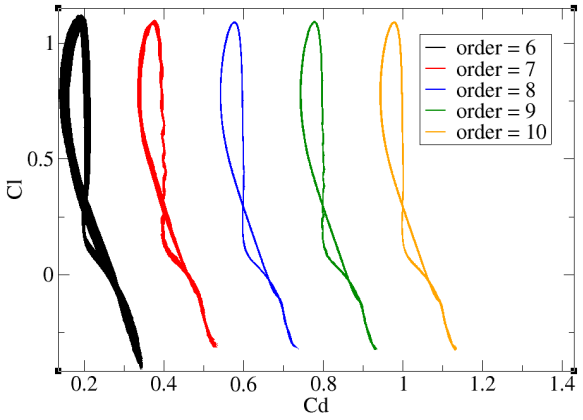

(b) Comparison of the types of solutions (figures have been displaced laterally for better visualization)

Figure 5.6: Analysis of the error as a function of the near-wall polynomial order of expansion at $Re = 3750$

expansion the solution is unchanged from the stability point of view. Furthermore the y^+ criterion is fulfilled and the error of increasing the number of computational points per element from 8×8 to 10×10 is inferior to 2% both for drag and lift. This order of accuracy is similar to the one estimated in part 1. Higher polynomials would compromise the computational time of the simulations.

5.3. FLOW CONTROL VALIDATION

The validation of the flow control devices will be reduced to assuring that there are no unphysical abrupt changes in the velocity, vorticity and pressure fields that can perturb the downstream flow. The goal of actuation is to suppress the boundary layer separation and produce a fresh boundary layer. The actuation will be considered valid if this goal is obtained. The suction is constant along the actuation surface and the suction has been fixed to the arbitrary value of 30% of the inlet velocity. Values lower than 10% will fail to achieve reattachment of the boundary layer, while increasing the suction amplitude can lead to numerical instability due to violation of the CFL condition at the flow control location[1].

[1] The near wall mesh has a very high resolution in the perpendicular direction to account for a good description of the boundary layer development and flow control effect. If the imposed velocity is increased, particles will eventually travel a larger distance in one time-step than the mesh size, violating the CFL condition

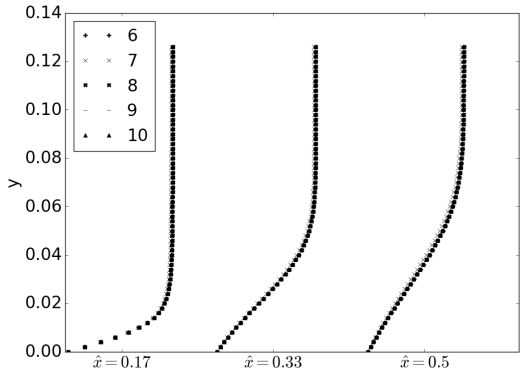

(a) Boundary layer profiles at $\hat{x} = 0.17$, $\hat{x} = 0.33$ and $\hat{x} = 0.50$

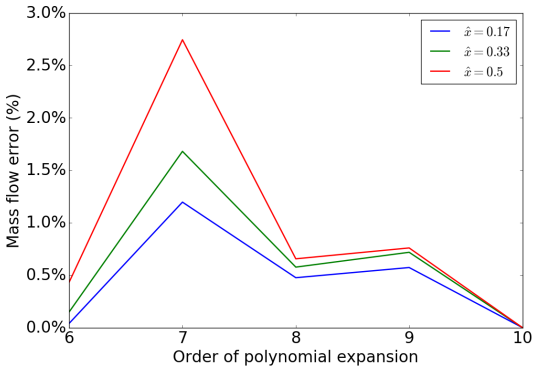

(b) Mass flow error

Figure 5.7: Study of the top roof boundary layer properties as a function of the near wall polynomial expansion order

5.3.1. STUDY OF THE BOUNDARY LAYER PROPERTIES

As explained earlier in this section the goal of the active flow control is to produce a boundary layer that is attached to the top roof. Therefore the effect of the flow control should be measured downstream of the control location. To evaluate the impact of mesh resolution on the active flow control the boundary layer properties at several downstream distances are evaluated. Several mesh resolutions are tested to establish that the solution is mesh independent. To perform this study the polynomial order of expansion of the mesh is varied in the range $6 < P_{order} < 10$. Defining $\hat{x} = x/L$ The velocity profiles over the roof at positions $\hat{x} = 0.17$, $\hat{x} = 0.33$ and $\hat{x} = 0.50$ are presented in figure 5.7a. The quality of the boundary layer representation is deemed good for all polynomial orders of expansion. However, for a polynomial order of 7 the result is slightly less accurate than for the other polynomial orders. Again, the software Nektar++ seems to produce lower quality solutions for odd orders of polynomial expansion than for even ones. To avoid this problem an even polynomial of expansion is used. The mass flow at the same locations is presented in figure 5.7b to give a quantitative approximation of the error. The order of magnitude of the error introduced in the boundary layer properties is less than 1% for all cases except for $P_{order=7}$, which has already been discussed and discarded.

6

BIFURCATION ANALYSIS FOR THE MODIFIED MODEL

6.1. INTRODUCTION

Similarly to what was done in the first part of this master thesis, the transitional regime of the new model will be studied. As already explained the main difference between the two models is that in this case there is no early separation in the top surface. This implies that the flow will remain attached to the top surface for a large range of Reynolds and consequently move the location of the bifurcations to values that are of the order 10 times larger than the ones observed in the previous part.

The aim of this section is to determine the different types of solutions of the transitional regime and study their properties. The information obtained in this section will be used in the application of AFC to the model (last part of this master thesis). The flow fields over the transitional regime are very similar.

6.2. DESCRIPTION OF THE BIFURCATIONS

The first behavior that is observed is a periodic vortex shedding in the rear slant. This is due to two reasons: first the slant is not rounded, second the lowest Reynolds of study is 1500. Following the discussion of the first part of this work one would expect to choose a lower Reynolds, fully laminar flow. However, the current model (which includes a suction on the front region) cannot force the flow to reattach in the front region at extremely low Reynolds, as the suction magnitude would have to be increased the more the Reynolds is decreased. Therefore, to study this region the geometry would have to be redesigned. Since the steady case does not present features as interesting as the consequent flow states it has been omitted.

6.2.1. FIRST PERIODIC STATE

For Reynolds greater than 1500, the model functions correctly, the boundary layer is reattached and a periodic flow is observed. Vortex shedding is the most relevant phenomenon. The natural vortex shedding frequency is found to be $f_{Str} = 0.187$. This value is in good agreement with Parkin [33], who performed 2D simulations of the Ahmed body at higher Reynolds. On the other hand it is also in good agreement with some measures of the vortex shedding frequency performed for the square Ahmed body which were presented in section 2.6.3 and were found to be in the range $f_{Str} \in (0.17, 0.25)$. However it is in a worse agreement with the measures performed on the 3D slanted Ahmed body which showed a vortex shedding frequency in the range $f_{Str} \in (0.07, 0.11)$. The vortex shedding process becomes more complex with increasing Reynolds. This can be observed in figure 6.1a. However, the natural frequency remains approximately constant in the range $1500 < Re < 3850$. This is shown in figure 6.1b, where the first peak of the Lift signal is located at the same frequency for all three shown Reynolds.

6.2.2. SECOND PERIODIC STATE

At approximately $Re = 3850$ a bifurcation occurs and a new periodic state is born. In this state the flow does not return to a certain flow state every vortex shedding cycle, instead it does every two cycles. This allows to identify the bifurcation as a period doubling bifurcation. The new branch is very similar to the previous one,

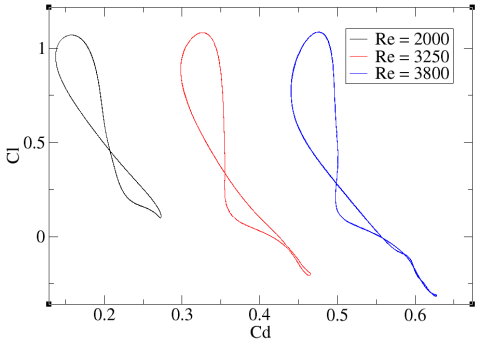

(a) Map of the aerodynamic forces at $Re = 2000$, 3250 and 3800 (first periodic state). Figures have been displaced laterally for better visualization

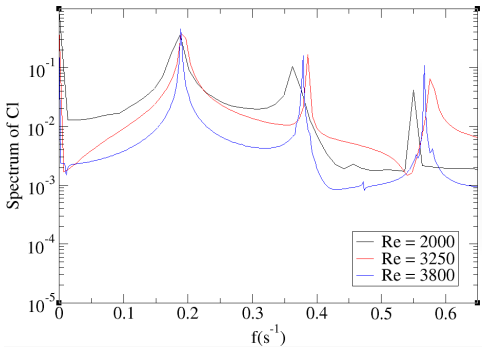

(b) Fourier transform of the lift coefficient at $Re = 2000$, 3250 and 3800 (first periodic state).

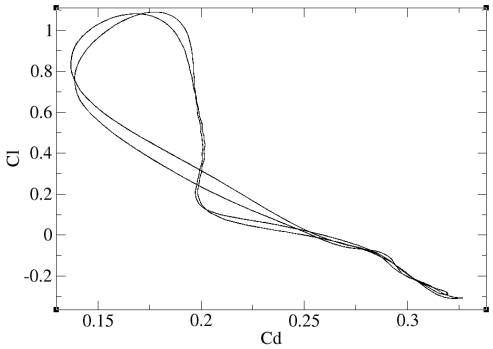

(c) Map of the aerodynamic forces at $Re = 3900$ (second periodic state)

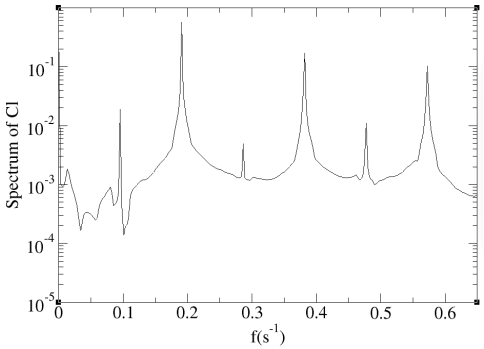

(d) Fourier transform of the lift coefficient at $Re = 3900$ (second periodic state).

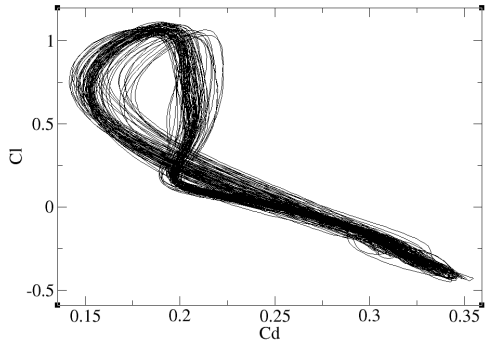

(e) Map of the aerodynamic forces at $Re = 4000$ (chaotic window)

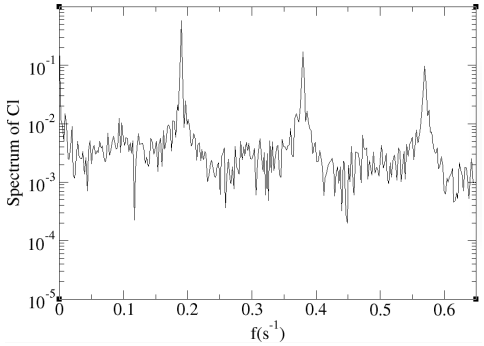

(f) Fourier transform of the lift coefficient at $Re = 4000$ (chaotic window).

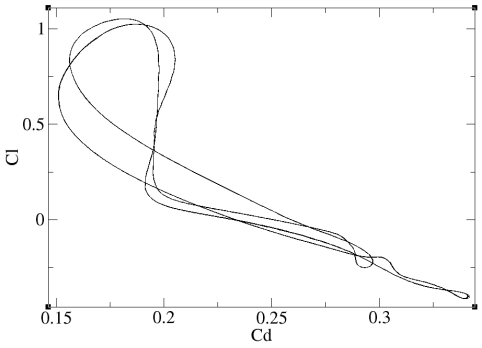

(g) Map of the aerodynamic forces at $Re = 4100$ (periodic window)

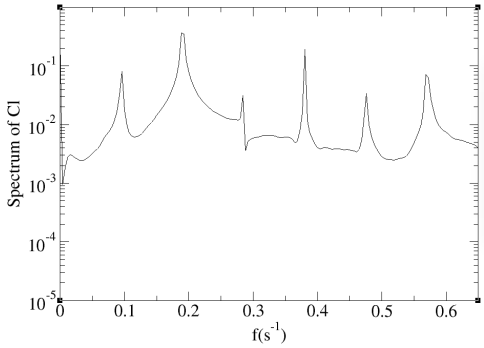

(h) Fourier transform of the lift coefficient at $Re = 4100$ (periodic window).

Figure 6.1: Summary of the different types of solutions

and the general flow characteristics and forces of the body do not vary greatly. Comparing the maps of the two branches, however, it is very clear that the qualitative behavior of the solution has changed (at $Re = 3750$ the solution repeats a single loop, while at $Re = 3900$ the solution performs two loops). This is shown in figure 6.1c. The Fourier transform of the signal presents a peak at half the vortex shedding frequency, which confirms the period doubling bifurcation (see figure 6.1d). The wake topology is not significantly altered (the shed vortices are slightly smaller one period, and slightly larger the next one), differences in the flow fields are almost imperceptible.

6.2.3. CHAOTIC WINDOW

At approximately $Re = 4000$ the solution becomes much more complex and is no longer periodic. The map of this state shows that there is no quasi-periodicity as the Cl-Cd curve does not close on itself (see figure 6.1e). This is further confirmed by a Poincaré section analysis of the signal. The study of the Fourier transform of the lift signal (figure 6.1f) reveals a great number of small peaks. These peaks could perhaps be associated to a new frequency (and its harmonics and the linear combination of this unidentified frequency with the vortex shedding frequency). If not, they can only be identified as noise. The solution can be classified as an early chaos which is mostly driven by the original solution. However, during the bifurcation the periodic solution has destabilized, so the new solution behaves as if it the periodic solution was attracting it but could not force a fully periodic state.

6.2.4. PERIODIC WINDOW

In the range $4050 < Re < 4300$ the solution re-stabilizes to a periodic state. The new periodic solution is similar to the period doubled case, as can be observed in figure 6.1g. Note that the peaks in the Fourier transform for the main frequency are almost identical (figure 6.1h). On the other hand, the peak of the period doubling phenomenon is now more energetic: it has a larger impact on the solution. Finding periodic windows after the first chaotic windows is not a common behavior. It can occur in at least two situations: a period doubling cascade or a sub-critical saddle node bifurcation.

SUBCRITICAL SADDLE NODE BIFURCATION

Assuming that the flow undergoes a supercritical saddle node bifurcation, implies that two solutions coexist. Assuming that the periodic solution is solution A and that the chaotic is solution B, it should then be possible to find a Reynolds at which it is possible to observe both states. Finding initial conditions that lead to the different states is therefore the way of verifying this scenario.

In the present study case the two states were found to occur at different Reynolds: the periodic solution is found at $Re < 3950$ and $Re > 4050$ while the chaotic solution has is observed in the range between these two values. If there were a supercritical saddle node bifurcation, then it should be possible to find a periodic solution in the range $3950 < Re < 4050$. The initial conditions that are most likely to produce this scenario are those of a fully developed periodic solution at $Re \approxeq 3900$ or $Re \approxeq 4100$. However, this scenario would also be validated if there were a point of the periodic region where with adequate IX the chaotic behavior could be observed.

To verify this possible scenario 4 experiments were performed:

1. Running a simulation at $Re = 4000$ starting from initial conditions of $Re = 3900$.
2. Running a simulation at $Re = 4000$ starting from initial conditions of $Re = 4100$.
3. Running a simulation at $Re = 3900$ starting from initial conditions of $Re = 4000$.
4. Running a simulation at $Re = 4100$ starting from initial conditions of $Re = 4000$.

All these experiments were designed with the goal of observing two different types of solutions at a given Reynolds. If all 4 cases tend to the solution that has already been observed, then it is reasonable to assume that this scenario does not occur. The results of this experiment have turned out to be negative. For all Reynolds numbers all solutions tend to the already observed flow state.

PERIOD DOUBLING CASCADE BIFURCATION

The period doubling cascade has been studied in the paradigmatic case of the logistic map (this example was discussed in section 2.5.4). In this cases the solution undergoes a number of period doubling bifurcations

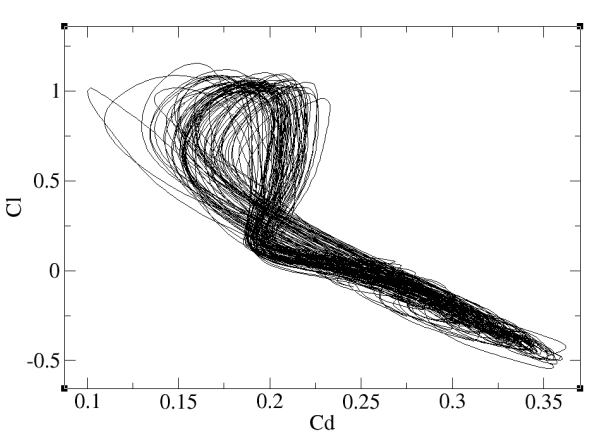

(a) Map of the aerodynamic forces at $Re = 4300$ (chaotic)

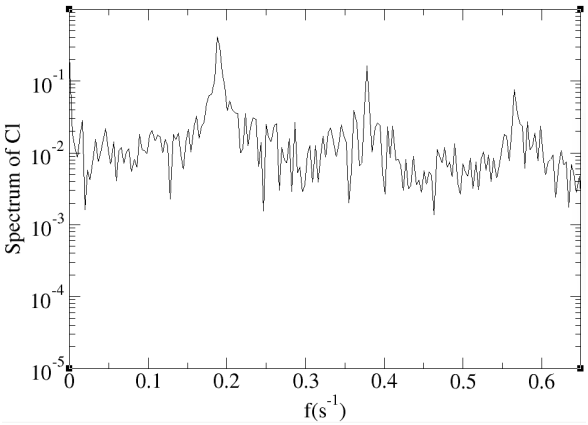

(b) Fourier transform of the lift coefficient at $Re = 4300$ (chaotic).

separated by an progressively smaller distance in the control parameter (in the present study the Reynolds number). This progression can be determined using what is known as renormalization theory. This theory states that the distance between superstable states (in this case a certain period double state and its period doubled state) decreases progressively with a scale α. To confirm this scenario, a new periodic state of period 4, 8, 16, etc. should be found. However, as already explained, the size of the windows in which these states occur is reduced with increasing period. This implies that the size of the largest window (period 4) can already be smaller than the experimental accuracy. To verify this scenario the only possibility is to increase the resolution in Reynolds number near the bifurcation point. After increasing the resolution to Reynolds steps of the order of 0.5 the period four solution was found. Since no further information would be obtained from finding this solution, it was concluded that further investigating this branch was not relevant as the computational cost is too large for the expected gain. The bifurcation scheme is assumed to be a period doubling cascade as it is the most likely possibility: a period 2 solution was observed before chaotic solutions were first observed and a periodic window is observed in the chaotic region. Given the similarities with the logistic map, the conclusion of this study is that a period doubling cascade is the most feasible bifurcation scheme.

6.2.5. CHAOTIC STATE

At approximately $Re = 4300$ the flow undergoes another bifurcation and becomes chaotic. This is consistent with the scenario of a period doubling cascade with periodic windows.

6.3. DESCRIPTION OF THE FLOW FIELDS

As an example of the behavior of the wake, the temporal evolution of the model at $Re = 3750$ is presented in figure 6.4. It is compared to the temporal evolution at $Re = 4100$ to show that there is no substantial difference in the flow fields in the transitional regime ($Re \in (3750, 4300)$) and therefore any Reynolds number in this range is representative of this regime. This case ($Re = 3750$) will be referred to as the baseline case from now on, as it is the basis for the actuated cases presented in the last part of this thesis. The analysis of the flow fields shows that vortex shedding is the driving phenomenon of the wake: two shear layers are observed (at the top and bottom separation regions) and vortices are shed alternatively. From the point of view of the bottom shear layer the process is simple: a vortex is generated, grows until it occupies the full rear base and is then shed. It is therefore possible to identify three phases, which are shown in figures 6.4 and 6.5: generation (frames 1-2), growth (frames 3-6) and shedding (frames 7-9). The snapshots are equally spaced in time from each other. The behavior of the top shear layer is more complex, but is mostly defined by the bottom vortex shedding. Three phases can also be observed: generation (frames 7-8), growth (frames 9-2) and shedding (frames 3-6). Therefore the two main vortex trails are shed in an out of phase synchronized fashion. Several key flow features can be identified in the vorticity snapshots: first of all a large shear layer is observed over the slant and destabilizes after it reaches the rear base. The separation angle of this shear layer oscillates between 10 deg and 20 deg (measured from the slant surface). Second, the bottom vortex is much larger than the top one, and dominates the wake (for instance in frames 2 and 3 it is possible to observe that it forces the shedding of the top shear layer vortex). Finally, the bottom vortex is observed to force flow to travel from the

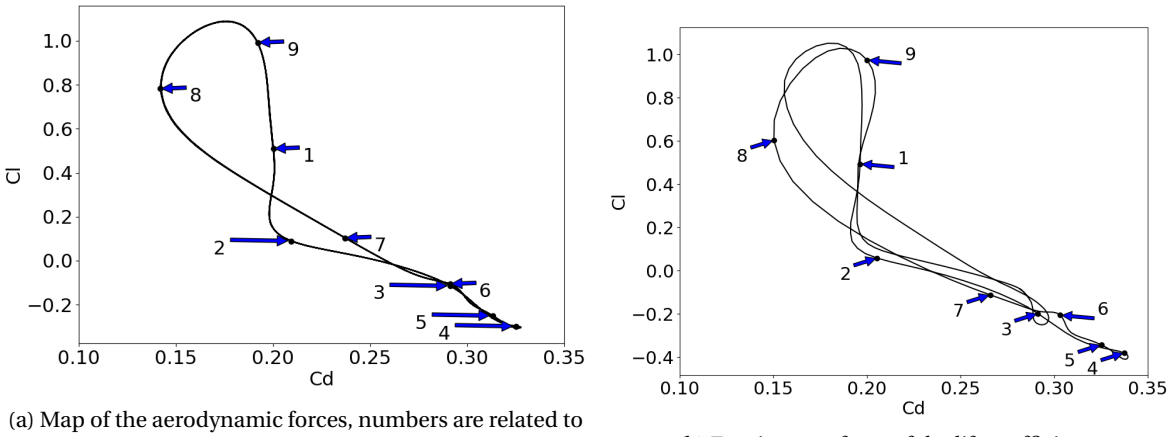

(a) Map of the aerodynamic forces, numbers are related to the snapshots show in figure 6.4

(b) Fourier transform of the lift coefficient

Figure 6.3: Comparison of the temporal evolution of the Cl-Cd maps at $Re = 3750$ and $Re = 4100$

rear base to the slant region during growth, generating a complex separation and reattachment scenario over the slant. This is clearly observed in the pressure and streamlines flow fields, which can present attached flow (frame 9), one large separation bubble (frames 1-3) or a complex combination of several vortices (frames 5-8).

The Cl-Cd curve behavior can be directly related to what is observed in the flow states, and is presented in figures 6.3a and 6.3b. The drag behavior can be directly related to the phases of the bottom vortex. During the bottom shear layer generation phase drag is observed to be constant, during this vortex's growth drag is slowly increased until reaching its maximum value, and finally during its shedding it is drastically decreased. This confirms that the bottom vortex shedding is the dominating phenomenon in the drag behavior. The largest changes in pressure are observed in the underbody region, indicating that the bottom vortex is also the determining factor in the behavior of Cl. The pressure variations over the slant are minor compared to those of the underbody, further confirming that this vortex is by far the most important flow feature in the analysis of the global forces of the body. This control over the wake is so important that it has frequency locked the top shear layer, and both phenomena occur at the same frequency. This is observed in figures 6.1b, 6.1d, 6.1f, 6.1h or 6.2b, which only present one peak at the vortex shedding frequency.

The conclusion of the study of the baseline case is that the most important phenomenon is the bottom vortex shedding. Large structures are observed near the rear base, which produces low pressure regions near the rear base in a periodic fashion. The oscillations in lift and drag are large due to the large pressure variations between when the vortical structures are observed near the rear base and when they are shed into the wake. Furthermore, this behavior is observed to occur along the whole transitional regime, and irrespective of the type of solution. To prove this, two periodic solutions are compared ($Re = 3750$ and $Re = 4100$) which correspond to two types of solutions. The similarities in the flow fields prove that any solution in the transitional regime is representative of the whole range of Reynolds.

Large variations on the global forces over each cycle imply that the vortex shedding phenomenon is large and therefore that actuation can potentially have a large impact on the solution. Furthermore, the flow is observed to separate and reattach over the slant during the vortex shedding period, indicating that a reduction in drag is potentially possible (the wake presents the High Drag topology, explained in section 1, which has been observed to be the wake topology that presents highest drag). Furthermore, as explained in section 1, large structures that appear next to the body are associated to high drag, which point towards a possible drag reduction by vortex splitting and/or vortex pushing.

6.4. CONCLUSIONS

The first goal of this chapter was to determine the transitional behavior was to characterize the transitional regime of the model. For this reason, the different types of solutions that appear in the transitional regime of the Ahmed body model were described and discussed. Starting from a periodic behavior the flow undergoes a first period doubling bifurcation, and then a period doubling cascade to a chaotic solution. However this chaotic regime seems to re-stabilize in the region $4050 < Re < 4300$, in which the period doubled solution is observed.

The study of the transitional regime has allowed to determine that the key flow features are maintained

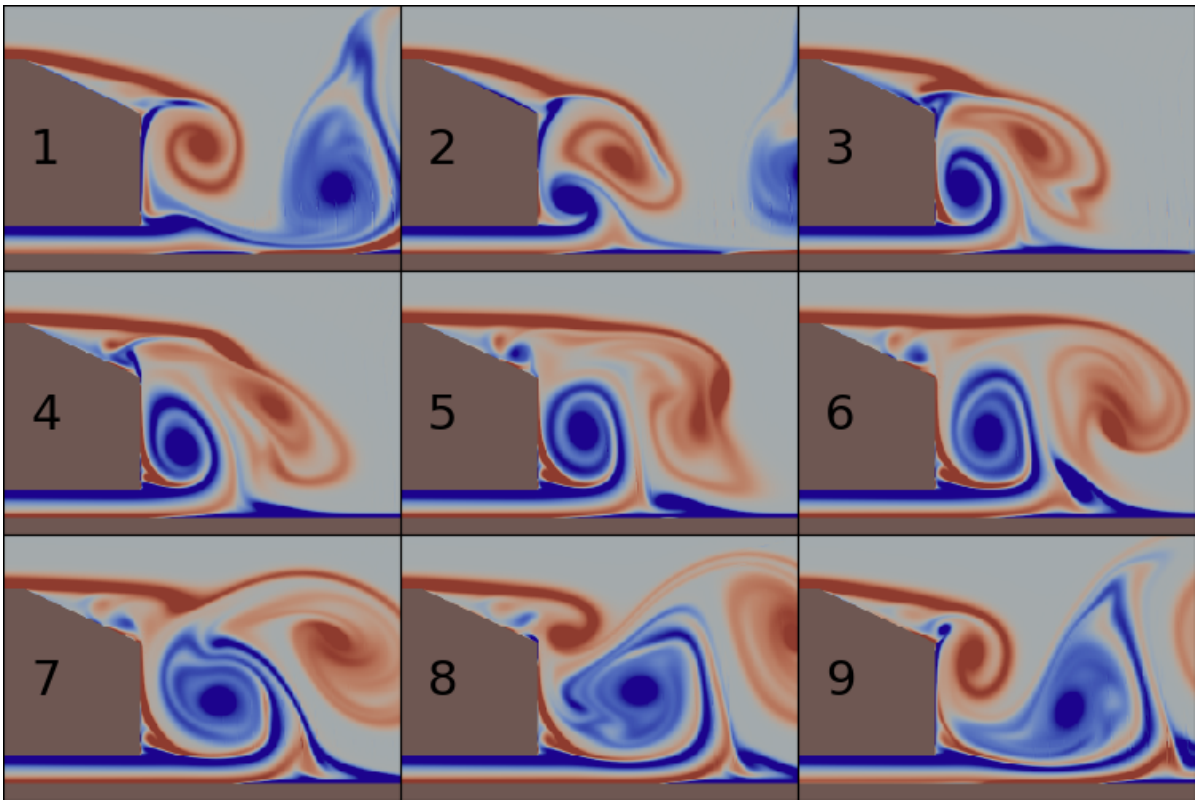

(a) Vorticity field for the baseline case at $Re = 3750$

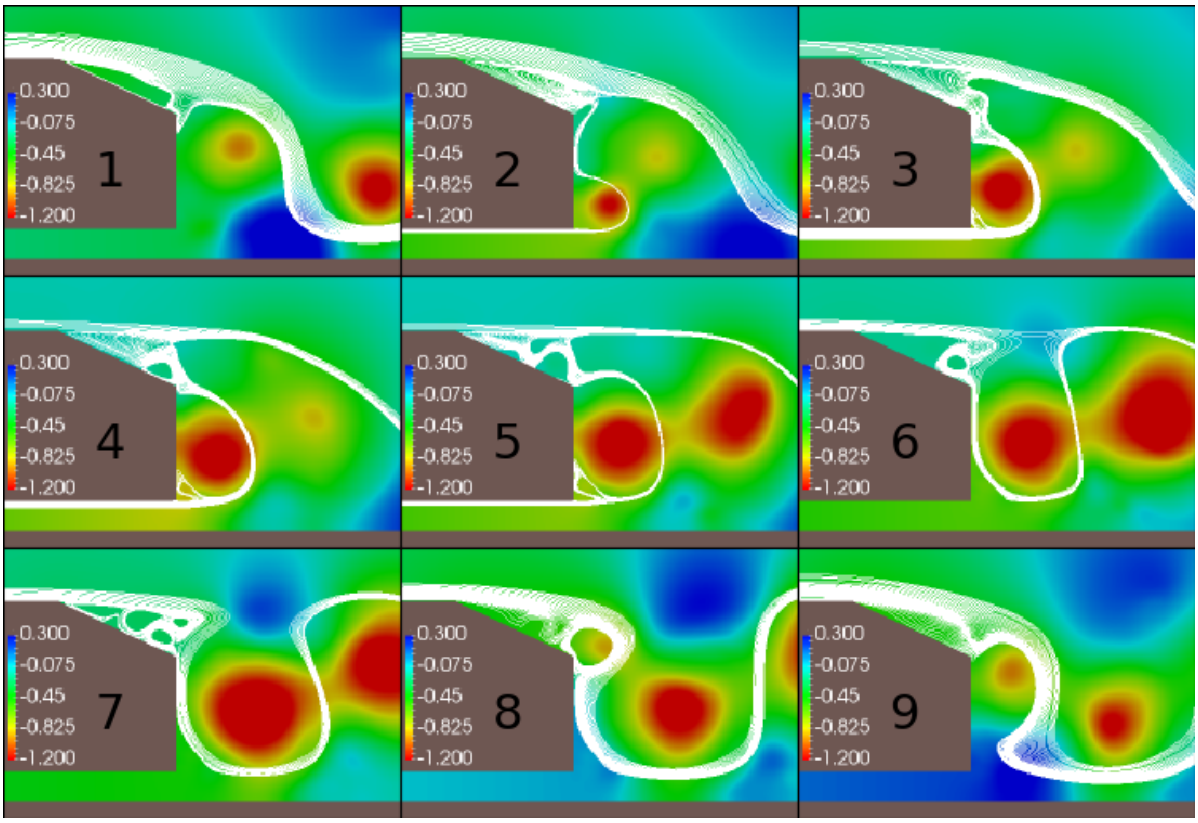

(b) Pressure field and streamlines for the baseline case at $Re = 3750$

Figure 6.4: Wake evolution diagrams for the baseline case at $Re = 3750$, snapshots are equally separated in time

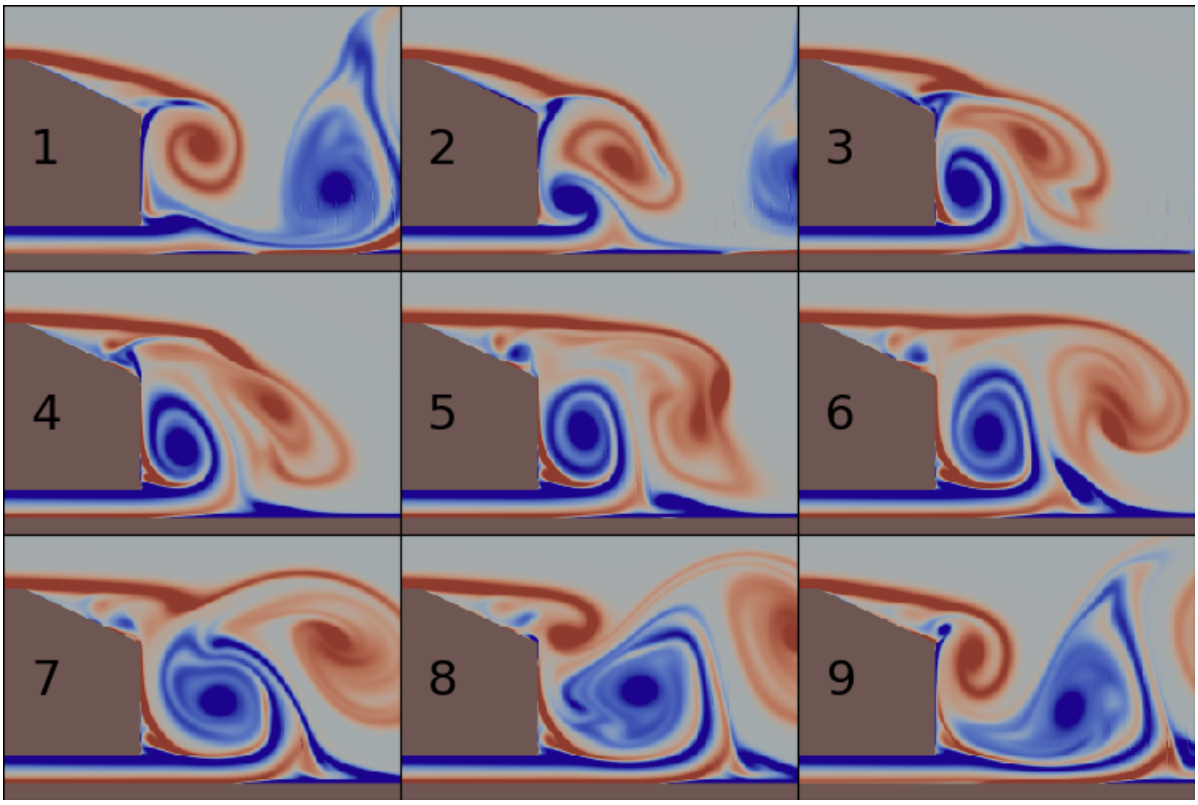

(a) Vorticity field for the baseline case at $Re = 4100$

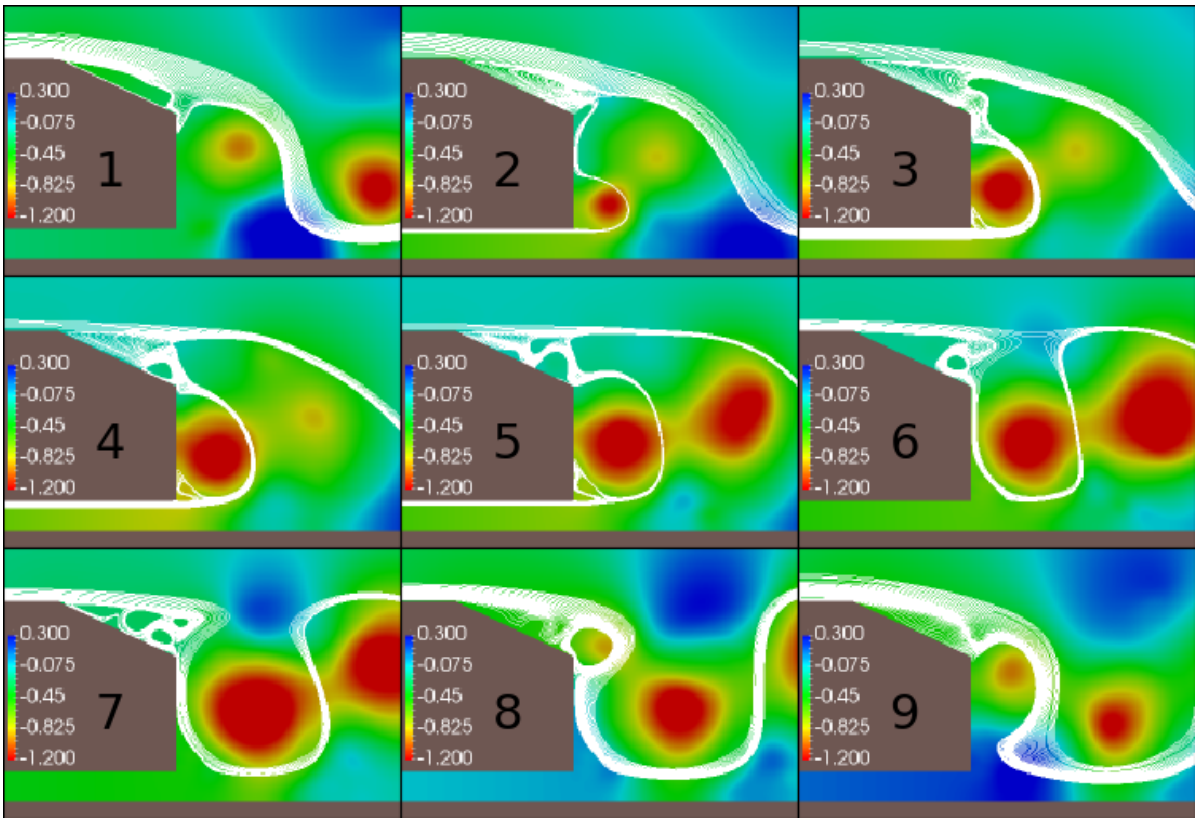

(b) Pressure field and streamlines for the baseline case at $Re = 4100$

Figure 6.5: Wake evolution diagrams for the baseline case at $Re = 4100$, snapshots are equally separated in time

relatively constant in the range of Reynolds numbers in which bifurcations are observed ($Re \in (3500, 4300)$). For this reason $Re = 3750$ is selected as a representative case of this regime for the application of AFC.

The second goal of this chapter was to determine the most interesting frequencies for the application of active flow control. Two main natural frequencies are found to appear: the vortex shedding frequency and the period doubling frequency (which is 1/2 of the vortex shedding frequency).

As explained in section 1.1.3 two main strategies in the application of AFC have been proposed in literature: flow control using a frequency of the order of the natural vortex shedding frequency and flow control using a frequency that is much larger than the vortex shedding frequency. In this project the first strategy was selected for two main reasons: first, the goal is to force the solution to bifurcate to a new flow state. It is assumed that it is more likely that the flow can adapt to a new solution that has a periodicity of the same order as the natural frequency of the problem than if the forcing frequency is an order of magnitude larger. On the other hand this was shown to be effective on other transitional flow models that are currently being studied in the physics department of UPC.

Both the natural vortex shedding frequency and half of it were selected as interesting actuation frequencies. Therefore the study of the actuation will be performed at these two frequencies and its harmonics. This study is presented in the third and last part of this thesis.

7

APPLICATION OF AFC

7.1. DESCRIPTION OF THE MODEL

The model that will be used for this section is similar to the one used for the second part of this thesis. The main difference is that a new region on the rear part of the roof is defined where a periodic suction and blowing boundary condition is imposed see figure 7.1. The domain that is used and the meshing philosophy are identical, however the mesh is refined near the new actuation surface.

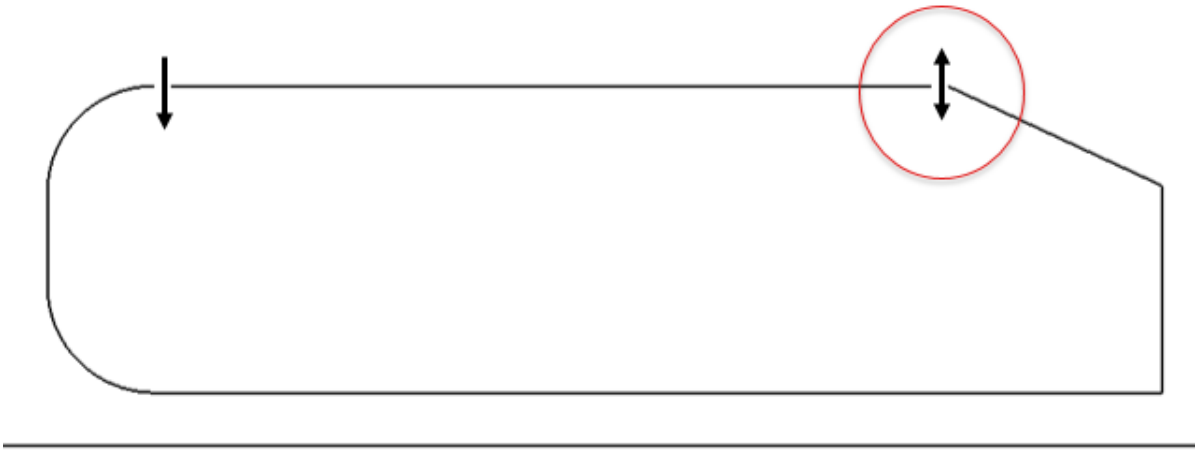

Figure 7.1: Schematic representation of the rear actuation

7.1.1. AFC BOUNDARY CONDITION

The changes to the boundary conditions are exclusively applied to the flow control surface. The Ahmed body top surface is split, and a region of approximately 5% of L (immediately next to the slant) is selected for actuation. The suction amplitude is set to vary between 5% and 100% of the inlet velocity. The velocity profile is chosen to be quadratic with maximum velocity at the center and 0 velocity at both ends. The jet momentum coefficient can be computed using the following formula:

$$C_\mu = \frac{\frac{1}{\tau}\rho_{AFC} A_{AFC} \int_0^\tau u_j^2(t)\,dt}{\frac{1}{2}\rho_0 u_0^2 A_0} \tag{7.1}$$

Therefore the actuation amplitudes correspond to a variation of C_μ in the range $C_\mu \in [3.6\times10^{-6}, 1.4\times10^{-3}]$. The maximum suction velocity that can be imposed is determined by the mesh density. Large suctions can bring numerical instabilities to the solution due to poor resolution. However small actuation amplitudes can fail to excite the flow instabilities, resulting in an unsuccessful actuation.

The actuation frequency is also presented in a non-dimensional fashion. Since the most relevant frequency was found to be related to vortex shedding, the non dimensional frequency $\hat{f}$ can be defined as the ratio between the actuation frequency and the natural vortex shedding frequency:

$$\hat{f} = \frac{f_{AFC}}{f_{Str}} \tag{7.2}$$

ACTUATION METHODOLOGY

The actuation frequency is one of the key parameters in AFC. As explained in the introduction section, two approaches exist in the application of active flow control based on this parameter: actuation at frequencies of the order of the natural vortex shedding phenomena and actuation at frequencies much larger than the natural vortex shedding phenomena. The first approach was chosen as the main area of study for this thesis project: in the second part of this master thesis several frequencies were selected to be studied because they represented the most relevant phenomena:

1. The natural vortex shedding frequency:
   Vortex shedding is the key phenomenon that drives the wake dynamics. Therefore an actuation at this frequency can potentially resonate with the vortex shedding process and bring new types of solutions. The flow actuation effect is not centered in changing the vortex shedding frequency; instead it is centered in trying to force the vortex shedding phenomena to occur in a synchronous fashion with the actuation. This corresponds to a non dimensional frequency of $\hat{f} = 1$

2. The first subharmonic of the vortex shedding frequency:
   In part 2 of this work the wake destabilization process in the transitional regime was described. The conclusions of this part were that the solution destabilized through a period doubling cascade process. The natural frequency of this phenomenon is equal to one half of the natural vortex shedding frequency. Actuation at this frequency could potentially resonate with the period doubling instabilities that occur in the transitional regime and bring new types of solutions. Therefore the target of this actuation is to modify the vortex shedding phenomenon by exciting a different one: in this case period doubling instabilities. This corresponds to a non dimensional frequency of $\hat{f} = 0.5$

3. The first harmonic of the vortex shedding frequency:
   This frequency was selected for two main reasons. On the one hand because it represents the second highest energy mode. This was observed in part 2 of this report, where the Fourier transform of the signal was presented. Since it is the first harmonic of the vortex shedding phenomenon, it presents the second strongest energy peak. On the other hand it was selected because several authors in literature present it as a relevant frequency. This type of actuation targets to force the vortex shedding phenomenon to occur twice per cycle, introducing new types of solutions and flow states. The instabilities that are targeted in this type of actuation are the vortex shedding instabilities, however in this case they are excited by applying two full actuation cycles per vortex shedding period. This corresponds to a non dimensional frequency of $\hat{f} = 2$

To complete the study a fourth actuation strategy was applied. It consisted in actuating at a frequency that is not a multiple of the vortex shedding frequency, but instead it is incommensurable. This strategy is not recommended in literature in general, however it was selected to determine if vortex shedding can be forced to occur at a frequency that is not related to the natural vortex shedding frequency. There exists an infinite number of possible frequencies that are incommensurable with respect to the natural vortex shedding frequency. As a representative example of these frequencies, $\hat{f} = 1.3$ was selected. This strategy does not target any physical instabilities, instead it tries to impose a new frequency to the vortex shedding process. Unfortunately, this actuation did not bring any new types of solutions that cannot be presented with $\tilde{f} = 1$ or $\tilde{f} = 2$. For this reason, it was decided not to include the results in the report.

7.1.2. CHANGES TO THE MESH TOPOLOGY

The mesh topology for this model was maintained similar to that of the baseline case, but additional resolution was added added near the AFC location and slant as in this region more energetic flow is observed. This has no impact on the baseline case, neither in flow properties nor in the Cl-Cd map. A zoom of the mesh near the body is shown in figure 7.2. The near wall mesh and the wake were imposed to have an expansion order of 8 and the far field laminar flow is imposed to have an order of expansion of 6.

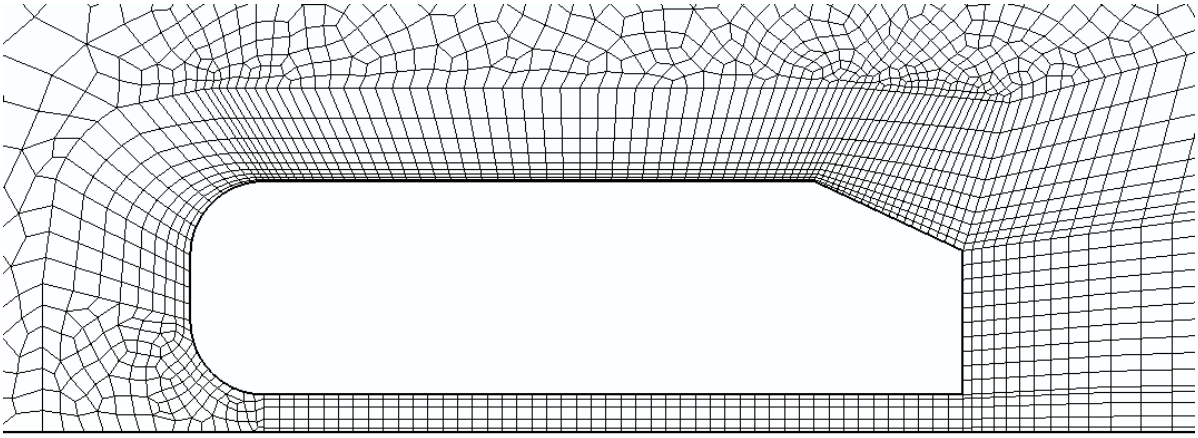

Figure 7.2: Detail of the new mesh near the body

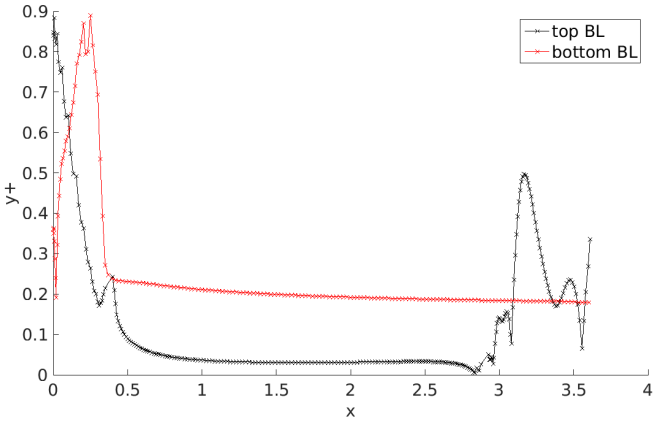

(a) y^+ distribution on the top and bottom boundary layers for $Re = 3750$, $\tilde{f} = 2$ and $C_\mu = 1.4 \times 10^{-3}$

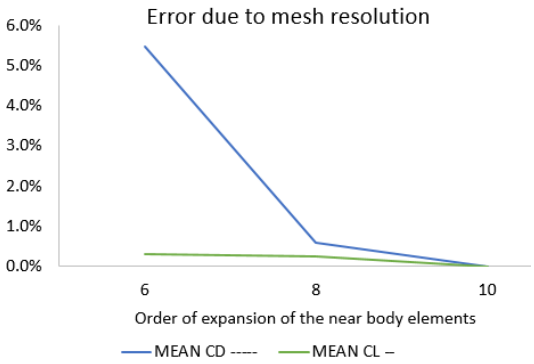

(b) Error of the solution as a function of the polynomial order of expansion for $Re = 3750$, $\tilde{f} = 2$ and $C_\mu = 1.4 \times 10^{-3}$

Figure 7.3: Study of the accuracy of the solutions

7.1.3. VALIDATION

The mesh resolution has been increased near the AFC to better resolve the actuation, and therefore the if the y^+ was already sufficient, now the boundary layer will be resolved with excess accuracy. However this is necessary to adequately resolve the effect of the actuation. To determine the accuracy of the solution both the y^+ criterion and a refinement in the polynomial order were applied, and are presented in figures 7.3a and 7.3b. The case of $\hat{f} = 2$ and maximum actuation amplitude ($C_\mu = 1.4 \times 10^{-3}$) was chosen as the most critical case, as it is the case that introduces the largest changes to the flow fields and is periodic. The study of the y^+ criterion reveals, as expected, that the representation of the boundary layer should be more than adequate, as the maximum value of y^+ is below 1. The resolution analysis only features the even polynomials of expansion because as explained in the previous sections the odd polynomials tend to introduce unphysical pressure oscillations. The results show that increasing the polynomial order of expansion produces changes to the average forces of the order of 0.5% when the near wall polynomial order of expansion is increased form 8 to 10, which is considered adequate. Additionally it is important to take into account that since the width of the periodic window is rather small, there are several bifurcations that could force the solution into a completely different solution. For this reason it is significant that the type of solution is unaffected by the polynomial order. The results are considered to provide sufficient accuracy.

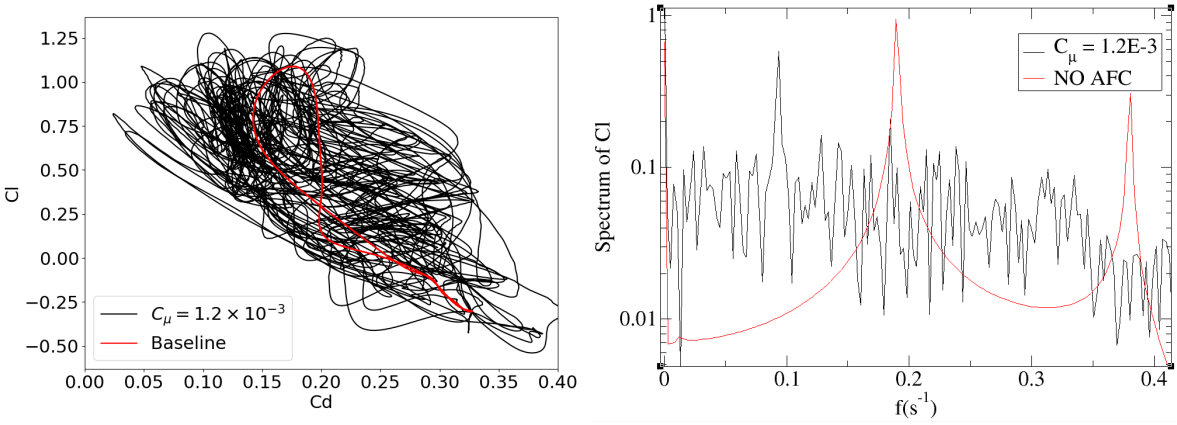

(a) Map of the aerodynamic forces

(b) Fourier transform of the lift coefficient

Figure 7.4: Analysis of the forces signal for $C_\mu = 1.2 \times 10^{-5}$ at $Re = 3750$ and $\tilde{f} = 1/2$

7.2. STUDY OF THE DIFFERENT TYPES OF SOLUTIONS

In this chapter the study of the results of the actuation application on the roof, at the junction with the slant of the Ahmed body at $Re = 3750$ will be presented. This actuation was performed at 4 discrete actuation frequencies ($\hat{f} = 0.5$, $\hat{f} = 1$, $\hat{f} = 1.3$, $\hat{f} = 2$). However, $\hat{f} = 1.3$ will not be presented because it does not bring any new interesting information. The velocity was imposed to vary in the range $u_AFC \in [0.05 \times u_0, u_0]$ with up to 11 different actuation amplitudes. The jet momentum coefficient was therefore varied in the range $C_\mu \in [3.6 \times 10^{-6}, 1.4 \times 10^{-3}]$.

In this section the different types of solutions that can observed will be described. The different types of actuated flows will be compared to the baseline (non-actuated) flow presented in section 6.3. The results will be discussed as a function of both the non-dimensional actuation frequency ($\hat{f}$) and the non-dimensional actuation amplitude: the momentum coefficient (C_μ).

7.2.1. ACTUATION AT $\tilde{f} = 1/2$

Actuation at the first subharmonic of the natural vortex shedding frequency has only been observed to produce chaotic solutions. From the quantitative point of view, however, it produces interesting results as average drag can be reduced up to 20% with respect to the baseline case.

In the study of the baseline case the bifurcation sequence of the model was discussed, and the two most unstable modes were identified. The first one was the natural vortex shedding frequency of the problem and the second one was the first subharmonic frequency, which produced a period doubling bifurcation. The target of this section is to investigate whether it is possible to excite the flow at this frequency and obtain a resonance that produces a new type of solution. This frequency has not been reported to produce interesting drag reductions at high Reynolds numbers in literature, and the amplitude of the period doubling instability is small in comparison with the natural vortex shedding instability, which indicates that this frequency is less likely to produce new solutions than the natural vortex shedding frequency. Nevertheless, it will be presented to demonstrate whether the flow is receptive to this kind of actuation.

Actuation at $\tilde{f} = 1/2$ only produces chaotic solutions because the flow states that are generated are maintained for enough time to allow for the solution to naturally destabilize. During the blowing half-period the flow is forced to separate at the junction between the roof and the slant. For small amplitudes this does not produce large variations on the flow field, as the top shear layer destabilizes slightly earlier (but still near the rear base) and the separated region is slightly larger, but the location and size of the vortices is quite similar. When the amplitude is increased the separation on the rear slant becomes more massive and vortices are shed over the slant, changing the pressure distribution over the slant. This reduces the intensity of the shed vortices on the rear base, as the rear base vortex is not allowed to grow in the slant direction. However this has a low impact on the rear base pressure. On the other hand during the suction phase the flow is forced to remain attached over the slant, in which the attached low drag scenario is observed, and the intensity of the rear base vortices is significantly reduced. Furthermore, they are not allowed to grow in the slant direction either, and appear at a larger distance from the rear base, leading to a drag reduction both by vortex pushing. In general this type of actuation seems to force the solution to shift between a constant suction and a con-

stant blowing scenario, leading to a drag reduction during the suction half-period and a no gain or even drag increase during the blowing phase. In general this type of actuation does not seem to produce any interesting effects that are not present in constant suction or blowing.

Figure 7.4a shows that the amplitude of vortex shedding is increased with respect to the baseline case both in lift and in drag, confirming that reduction of the vortex shedding intensity has not been achieved. The Fourier transform of the signal further confirms that the flow is controlled by the AFC, as it presents a peak at the actuation frequency, but there is no indication of relevant resonances on the flow.

SUMMARY OF ACTUATION AT $\tilde{f} = 1/2$

The result of this actuation can be compared to applying a constant suction at the start of the slant during one vortex shedding period and a constant blowing during another one. During the suction period the vortex shedding amplitude is reduced, accounting for most of the drag reduction, and during the blowing phase the flow is forced to separate, accounting for most of the lift increase. Figure 7.6 presents the average Cl and Cd and the root mean square of the signals, compared to the baseline case. To evaluate the vortex shedding amplitude the RMS of both Cl and Cd can be computed. These provide a measure of deviation from mean quantities. Since the main phenomenon in all solutions is vortex shedding, in this case it provides with an approximate order of magnitude of the amplitude of this phenomenon. According to the results the RMS of the lift coefficient is maintained constant or slightly reduced (the extreme cases present a 20% reduction and a 5% increase in this quantity), while the RMS of the drag coefficient is increased with increasing actuation amplitudes (reaching up to a 25% increase). This indicates that in average the gain in vortex shedding intensity the top shear layer during blowing is compensated by the suction period (which is reflected in the slight reduction in the RMS of Cl). Second it seems to indicate that the vortex shedding intensity of the bottom shear layer is slightly increased (which is reflected in the slight increase in the RMS of Cd). Since drag is reduced in average, the only possible explanation is that although the bottom shear layer vortices are more energetic, they are shed faster into the wake, which is consistent with a drag reduction by vortex pushing.

It can also be interesting to analyze which regions of the vehicle contribute most to drag in each case. In the baseline case the pressure drag accounts for approximately 75% of the total drag and is the quantity that best represents the effect of flow control on the problem[1]. Therefore it is possible to compare which part of the Ahmed body (rear base or slant) contributes most to the total pressure drag in each case. Surprisingly the largest effect on pressure drag is observed on the rear base and not in the slant. This indicates that the average pressure over the slant is not greatly affected by actuation (on average), while the rear base is more affected. The reason for the rear base reduction was already explained, but a non-zero effect on the slant was also expected. This can only be explained because in average the additional separation during blowing is compensated by the reattachment introduced by suction.

In general it is not possible to conclude that the vortex shedding phenomenon has been substantially reduced, as the size and intensity of the vortices has been reported to remain similar or become larger both in the analysis of the flow fields and the study of the quantitative data. Therefore it can be concluded that despite the drag reduction, the actuation was not successful in reducing the vortex shedding intensity, nor in achieving resonance with the main flow structures.

7.2.2. ACTUATION AT $\tilde{f} = 1$

Actuation at the natural vortex shedding frequency targets to excite the main instability of the flow. By introducing a perturbation right before the separation point of the top shear layer, the goal is to change the way in which the top shear layer behaves. Actuation at this frequency is one of the most successful types of actuation at high Reynolds. This can be due to the fact that the active flow control resonates with the global instability of the flow (which is at the current Reynolds the only unstable mode that has been observed for the baseline case and is the most unstable mode at higher Reynolds).

Actuation at the natural vortex shedding frequency creates 3 different types of new solutions. These solutions can be qualitatively different from the stability analysis point of view or quantitatively different (for instance in the lift and drag coefficients). In this section the differences in flow features that drive these changes will be presented and discussed.

[1]The variations in friction drag are minor as the surfaces and velocity fields have not been greatly changed over the top and bottom surfaces, furthermore friction drag only contributes to 25% of the total drag

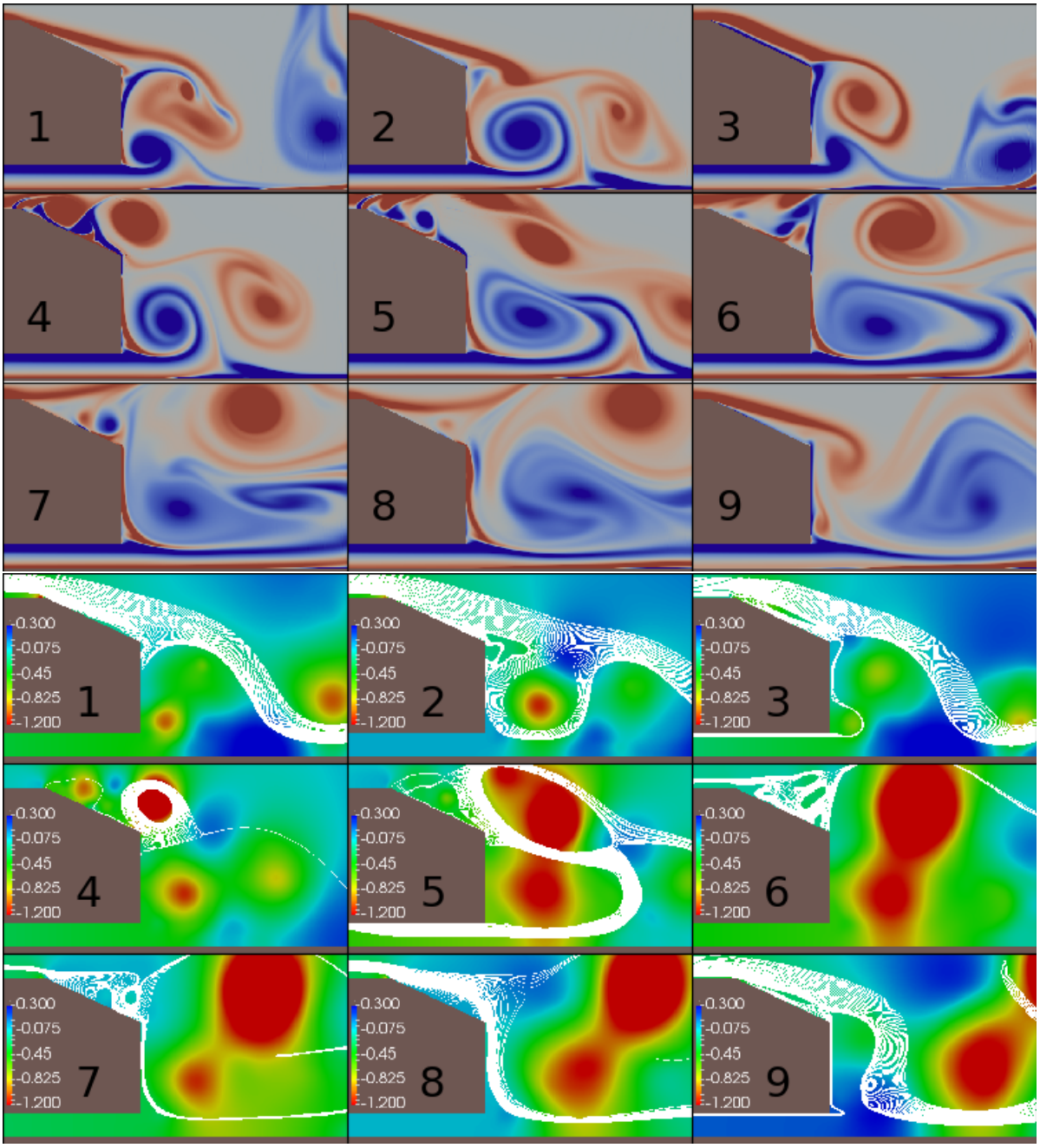

Figure 7.5: Wake temporal evolution for $\tilde{f} = 1/2$ and $C_\mu = 1.2 \times 10^{-3}$ at $Re = 3750$ (chaotic), snapshots are equally separated in time

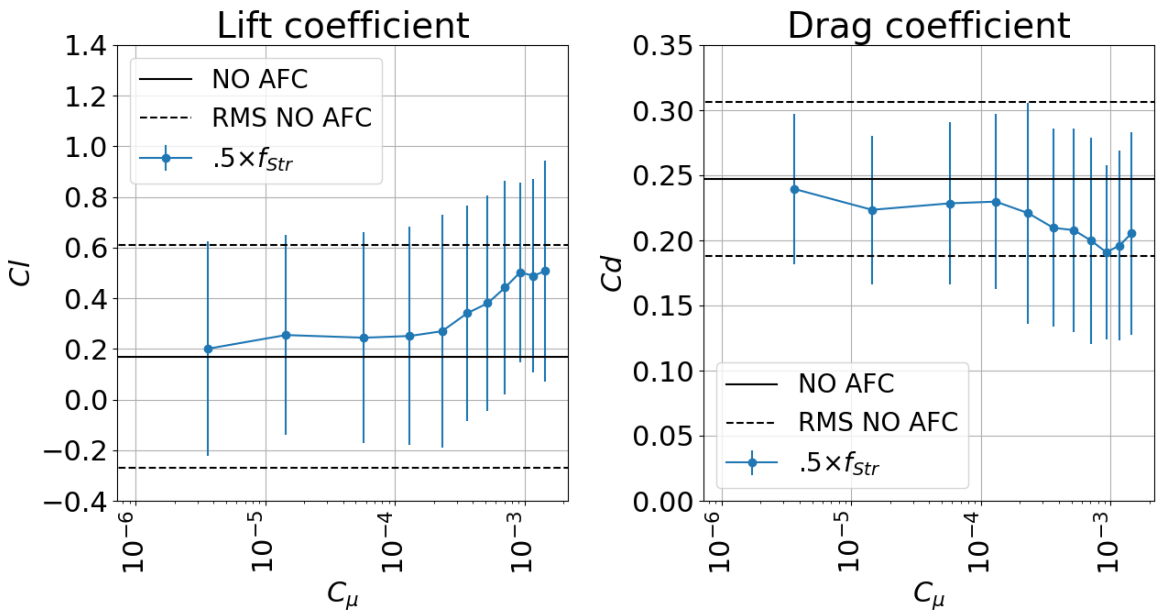

Figure 7.6: Lift and drag coefficients as a function of the jet momentum coefficient for $\tilde{f} = 1/2$ at $Re = 3750$, the error bars represent the RMS of the signal

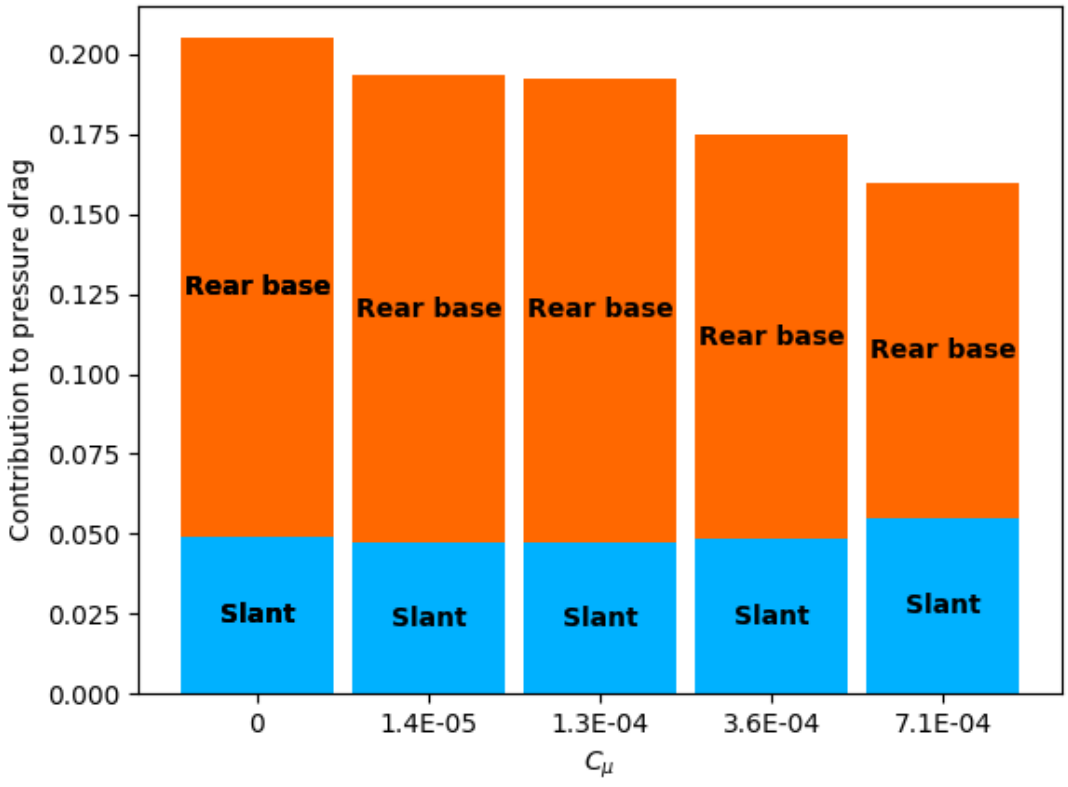

Figure 7.7: Contribution of the different parts of the body to the total drag as a function of the jet momentum coefficient at $Re = 3750$ and $\tilde{f} = 1/2$

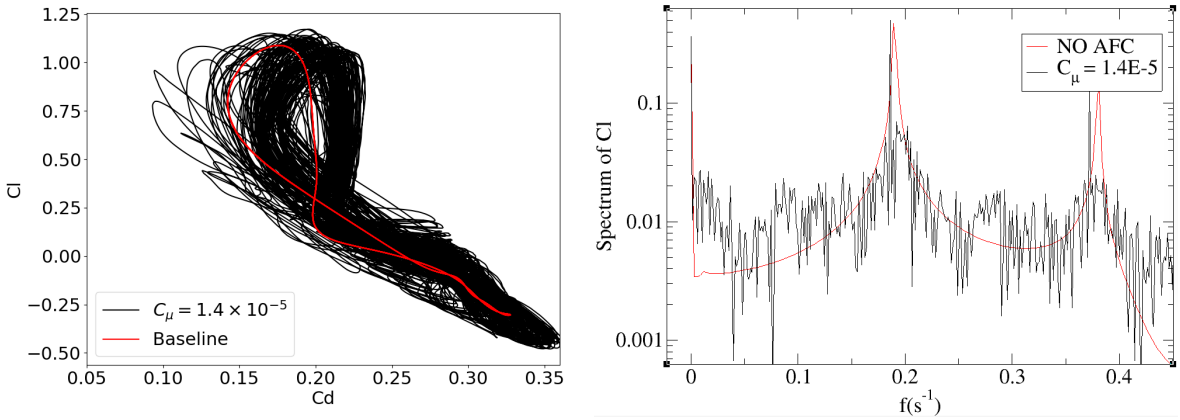

(a) Map of the aerodynamic forces

(b) Fourier transform of the lift coefficient

Figure 7.8: Analysis of the forces signal for $C_\mu = 1.4 \times 10^{-5}$ at $Re = 3750$ and $\tilde{f} = 1$

LOW ACTUATION AMPLITUDES ($C_\mu < 2.3 \times 10^{-4}$)
For low actuation amplitudes the flow control fails to excite the vortex shedding instability, and the flow characteristics resemble the baseline case from the quantitative point of view. However the flow control destabilizes the periodic vortex shedding process, generating a chaotic solution. The Cl-Cd map of this new flow state is presented in figure 7.8a. The main flow characteristics remain similar to those observed for the baseline case.

MODERATE ACTUATION AMPLITUDES ($C_\mu = 2.3 \times 10^{-4}$)
For moderate actuation amplitudes a new periodic solution is observed. The frequency of this solution is equal to the original vortex shedding and actuation frequency. From the point of view of global forces this new type of solution does not present any interesting new features (the average quantities are very similar to those of the baseline case). However, the vortex shedding process has been altered: in this new scenario the separation of the boundary layer is affected during the blowing phase of the flow control (figure 7.10, snapshots 1 to 3). The separation of the top shear layer during this period of the flow control is larger, forcing the destabilization of the wake at the center of the slant region. However, the vortex that is generated is not sufficiently energetic to stop the flow from the rear base vortex from entering the slant, and the rest of the vortex shedding cycle is very similar to the baseline case. This explains why the average forces are similar to the baseline case and why the Cl-Cd map (figure 7.9a) is only significantly different during the blowing phase of the cycle (points 1 to 3). The rest of the cycle is very similar with respect to the baseline case from the point of view of the velocity fields. The largest difference is observed on the slant region (figure 7.10, snapshots 5 to 7), where a single vortex is observed (in the baseline case multiple vortices where observed: snapshots 5 to 7). The bottom vortex is only slightly modified, showing that the flow control fails to excite the bottom shear layer. Although this solution may seem very similar to the baseline case, it shows that actuation is imposing a larger separation over the slant during the vortex growth process. In the baseline case the vortex shedding of the top wake was controlled by the bottom vortex, as it was the most energetic phenomenon. A moderate actuation amplitude, however, is energizing the vortices produced by the top boundary layer, and now both phenomena compete to dominate the slant vortex shedding process.

The conclusion of the study of the periodic solution is that although the chaotic solution is observed to re-stabilize into a periodic solution, the new wake state is not interesting from the point of view of drag reduction. Furthermore, it is not interesting from the point of view of the changes to the flow, as they are constrained to the blowing phase of the actuation in the slant region. The most interesting phenomena of this type of solution is its bifurcation scheme. Figure 7.9a shows the type of solution for both $C_\mu = 2.4 \times 10^{-4}$ and $C_\mu = 2.4 \times 10^{-4}$, showing that both a period 1 and period 2 solutions are observed. This indicates that similarly to what was observed in the bifurcation scheme when changing the Reynolds number, period doubling cascades seem to be the natural mechanism for the creation and destruction of periodic solutions.

LARGE ACTUATION AMPLITUDES ($C_\mu > 2.3 \times 10^{-4}$)
For actuation amplitudes $C_\mu > 5 \times 10^{-4}$ the flow is completely modified and the average forces on the body are greatly affected. By increasing the momentum coefficient to $C_\mu > 1 \times 10^{-3}$ the mean Cd is reduced by 30% and

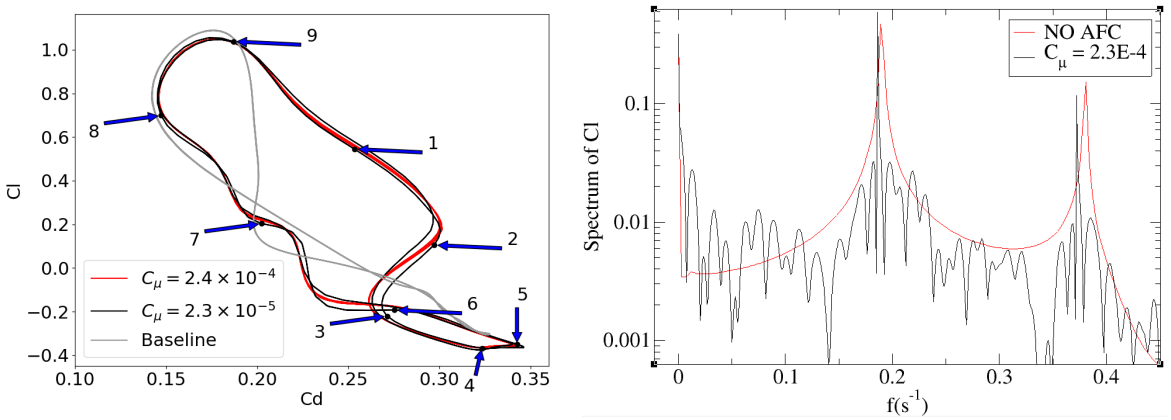

(a) Map of the aerodynamic forces

(b) Fourier transform of the lift coefficient

Figure 7.9: Analysis of the forces signal for $C_\mu = 2.3 \times 10^{-4}$ at $Re = 3750$ and $\tilde{f} = 1$

the mean lift is increased by 250%. For $C_\mu > 7.1 \times 10^{-3}$, the effect saturates, presenting a Cd approximately 40% lower than the baseline Cd and approximately 400% larger than the baseline Cl.

In this range of C_μ the solutions become chaotic. No periodic solution could be found in the range $C_\mu \in [2.3 \times 10^{-4}, 1.4 \times 10^{-3}]$. The Fourier transform of the lift and drag signals (see figure 7.11b) reveals that the natural frequency of the solutions has not varied, indicating that vortex shedding remains the main phenomenon. An interesting fact is that the amplitude of both the Cl and Cd signals has been reduced, indicating that vortex shedding has been attenuated. Although the solution is chaotic it is possible to observe clearly the vortex shedding process. This phenomenon now occurs differently depending on time, and therefore it is not possible to present an accurate description with only a few snapshots, however it is still possible to observe some common features with the previous cases. The top actuation now completely controls the vortex shedding process as the top shear layer dominates the near wake over the bottom vortex. The result is that now very little flow from the bottom region is introduced into the slant, and when this occurs it is shed into the near wake in a short time interval. The oscillating motion of the flow moving from the rear base towards the slant and back is now substituted by a motion that is unidirectional from the slant towards the wake. To obtain this behavior, however, a periodic reattachment and massive separation is observed over the rear slant. This is due to the fact that the top shear layer destabilizes over the slant and therefore the vortices are shed there (see figure 7.12). This implies that the low pressure vortex cores are generated directly in the slant region (which partially explains the increase on average lift). Since there is no flow moving from the rear base to the slant region the lower vortex cannot grow as it would in the baseline case. This is particularly important for two reasons: first of all the strength of the vortex is greatly reduced and secondly as it is not bound to the slant, the vortex core is observed to appear at a greater distance from the rear base. Additionally, the vortices from the top shear layer now push the bottom vortices away from the rear base. This has a large impact on the drag of the body, but also on the lift, as the underbody pressure is increased. A surprising effect of this actuation is that now the rear base vortex shedding frequency is observed to be larger than the NVS frequency. This can also be observed in the Fourier transform of the signal, which presents a second peak at $\tilde{f} \approx 1.5$. The chaotic behavior is introduced by the fact that there are now two different main frequencies on the flow. The conclusion of this section is that forcing a dominating vortex on the top slant will reduce the rear base vortex intensity and increase its frequency, effectively moving the vortex generation towards the slant. This has the positive effect of greatly increasing the pressure on the rear base and underbody, greatly reducing drag and increasing lift.

To summarize the complex behavior of the flow fields figure 7.11 shows the growth of two consecutive vortices. The changes in the slant region are observable in snapshots 4 to 6 and 11 to 12, where the large vortices generated by the destabilization of the top shear layer the slant travel downstream without opposition from the rear base vortex. This vortex is now clearly less energetic, and is generated at a larger distance from the rear base in both periods. This is observable both in its size and location (for instance in snapshots 3 and 9) but also particularly in the intensity and size of the low pressure regions. The reader can compare with figure 6.4 to see to which extent these changes have altered the wake topology.

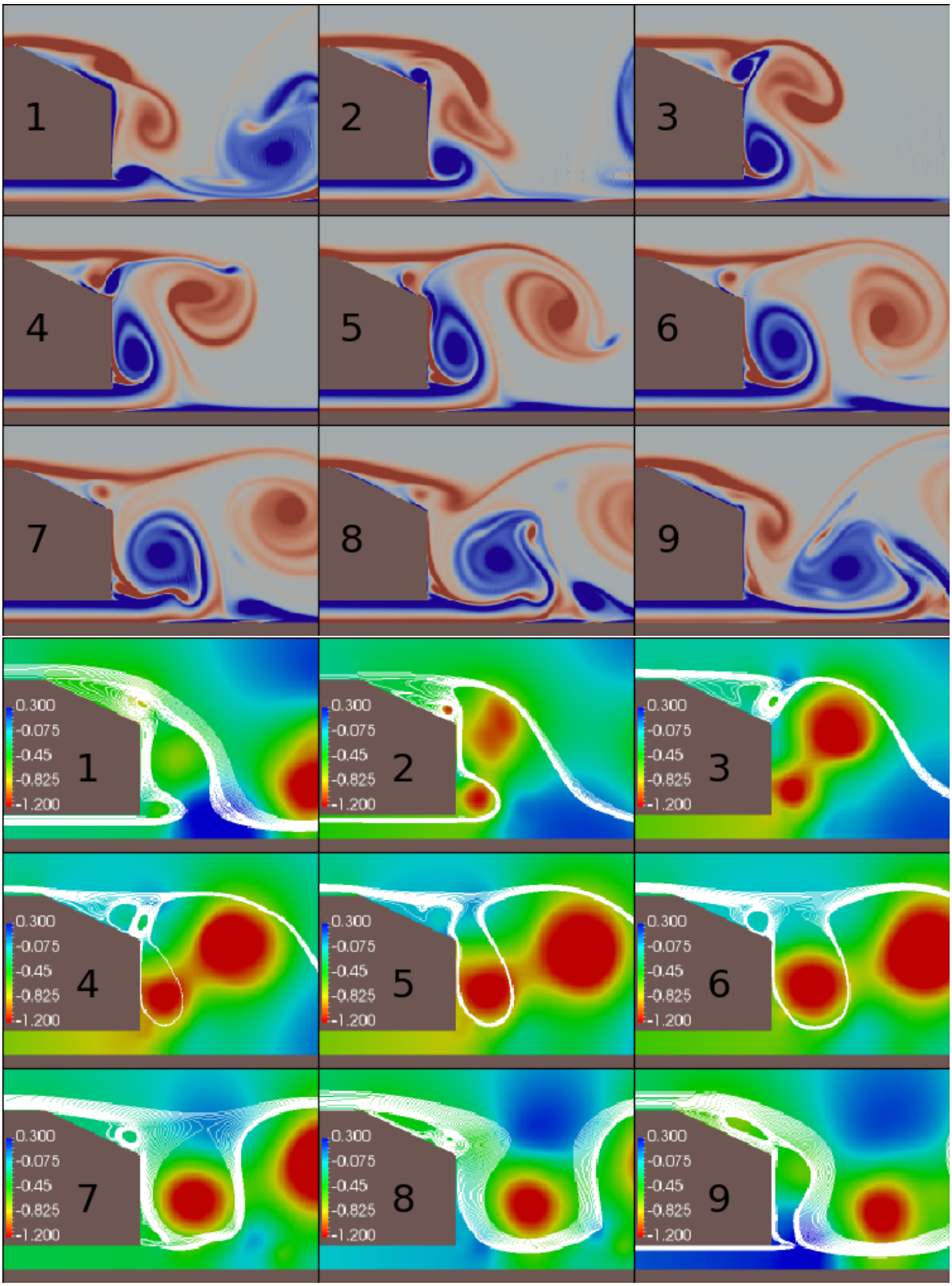

Figure 7.10: Wake temporal evolution for $\tilde{f} = 1$ and $C_\mu = 2.3 \times 10^{-4}$ at $Re = 3750$ (periodic), snapshots are equally separated in time

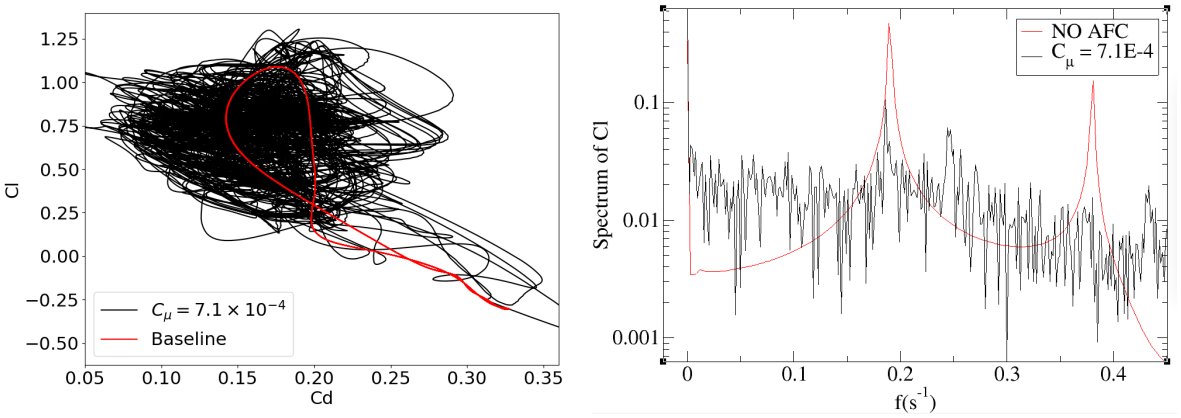

(a) Map of the aerodynamic forces

(b) Fourier transform of the lift coefficient

Figure 7.11: Analysis of the forces signal for $C_\mu = 7.1 \times 10^{-4}$ at $Re = 3750$ and $\tilde{f} = 1$

SUMMARY OF THE ACTUATION AT $\tilde{f} = 1$

By actuating at the natural vortex shedding frequency on the rear slant the performance of the body has been greatly modified. The drag coefficient has been reduced by up to a 40% and the lift coefficient has increased by up to 400%. This improvement, however is only observed when the actuation amplitude exceeds the threshold of $C_\mu > 2.3 \times 10^{-4}$. The effect quickly saturates, presenting similar drag reduction and lift increase for $C_\mu > 7.1 \times 10^{-3}$. This reduction is obtained by exciting the natural instability, the resonance of which reduces the vortex shedding amplitude. This can be observed in figure 7.13, in which the average Cl and Cd and the root mean square of the signals is presented. In the case of Cl, the RMS of the signal for successful actuation cases is reduced between 60% and 80% of the non-actuated baseline case RMS. On the Cd signal this reduction is smaller, but still represents between 20% and 30% of the baseline case RMS. This clearly indicates that the vortex shedding phenomenon has been substantially reduced. This seems to contradict what was described in the previous sections, as forcing the breakup of the shear layer by generating larger vortices over the slant was responsible for the drag reduction. The explanation for this phenomenon is simple: flow actuation has greatly reduced the strength of the rear base vortices by exciting the slant shear layer. The additional energy introduced in the top shear layer is smaller than the decrease of energy of the rear base vortex, effectively reducing the amplitude of the oscillation of the global forces.

It is also particularly interesting to analyze which regions of the vehicle contribute most to drag in each case. In the baseline case the pressure drag accounts for approximately 75% of the total drag and is the quantity that best represents the effect of flow control on the problem. Therefore it is possible to compare which part of the Ahmed body (rear base or slant) contributes most to the total pressure drag in each case. According to what was observed in the pressure fields, it is expected that for successful actuation the drag contribution of the slant is increased due to the new low pressure vortices, while the drag contribution of the rear base is reduced as the low pressure cores have been pushed away. Figure 7.14 shows a comparison of the drag contributions of three relevant cases (unsuccessful actuation, moderately successful actuation, and large drag reduction) with the baseline case. From the results it is clear that for the unsuccessful case the drag contributions of the different parts are almost identical both in percentage and total contributions to those of the baseline case. However, as the actuation amplitude increases the rear base drag contribution greatly decreases (approximately 50% of the baseline case) while the contribution of the slant increases (approximately 30% of the baseline case). Since the rear base is the surface that contributes most to total drag by far, the net effect on the body is a reduction of this quantity.

The study of average fields can also bring new interesting information on the wake topology. In particular the average pressure fields are very interesting as they show where the vortex cores spend most time and can be directly related to the total forces exerted on the vehicle. Figure 7.15 shows a comparison of the baseline case pressure distribution with a successfully actuated case. The base pressure has been greatly increased by generating a large depression on the rear slant that was not present in the baseline case. The high pressure of the rear base can be explained due to the fact that the vortex cores that are generated by the bottom vortex shedding are now being generated at a larger distance from the base, and are less energetic (smaller in size). The increase in the lift coefficient can be explained by two factors: on the one hand the slant average pressure

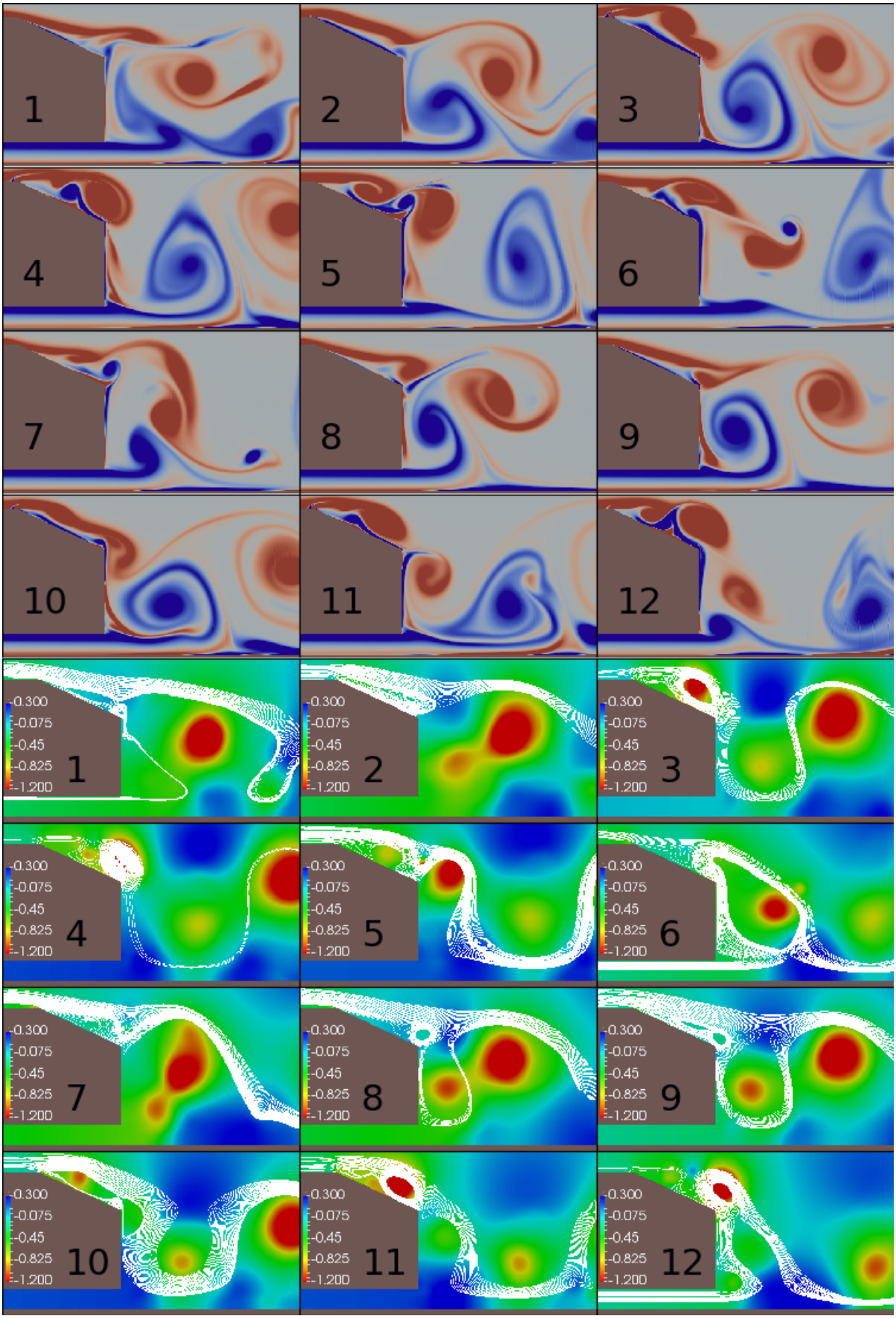

Figure 7.12: Wake temporal evolution for $\tilde{f} = 1$ and $C_\mu = 7.1 \times 10^{-4}$ at $Re = 3750$ (chaotic), snapshots are equally separated in time

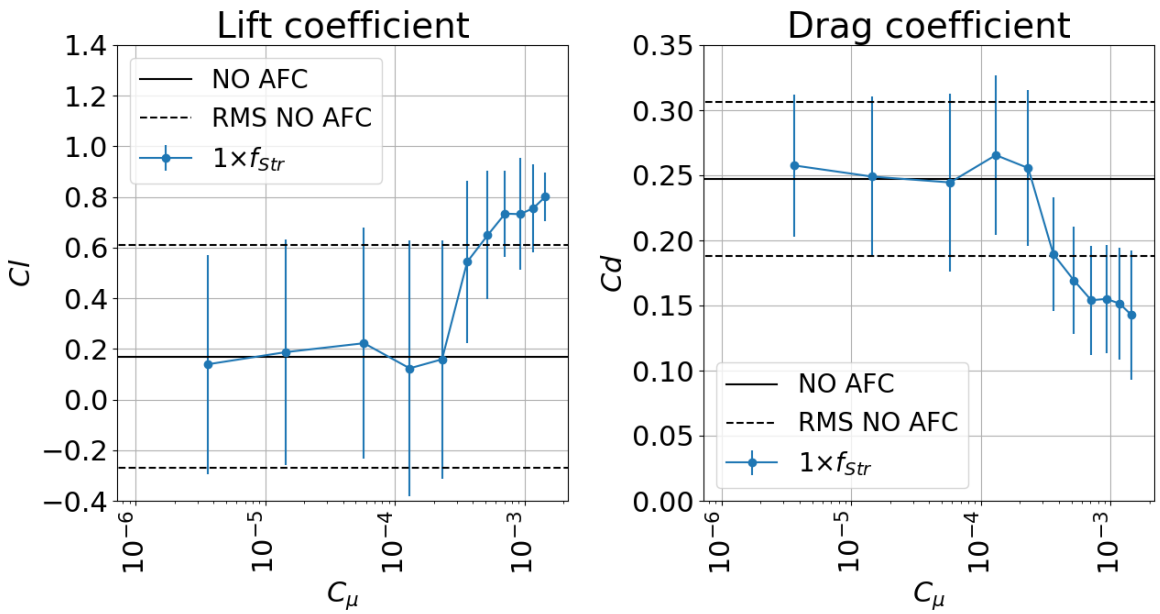

Figure 7.13: Lift and drag coefficients as a function of the jet momentum coefficient for $\tilde{f} = 1$ at $Re = 3750$, the error bars represent the RMS of the signal

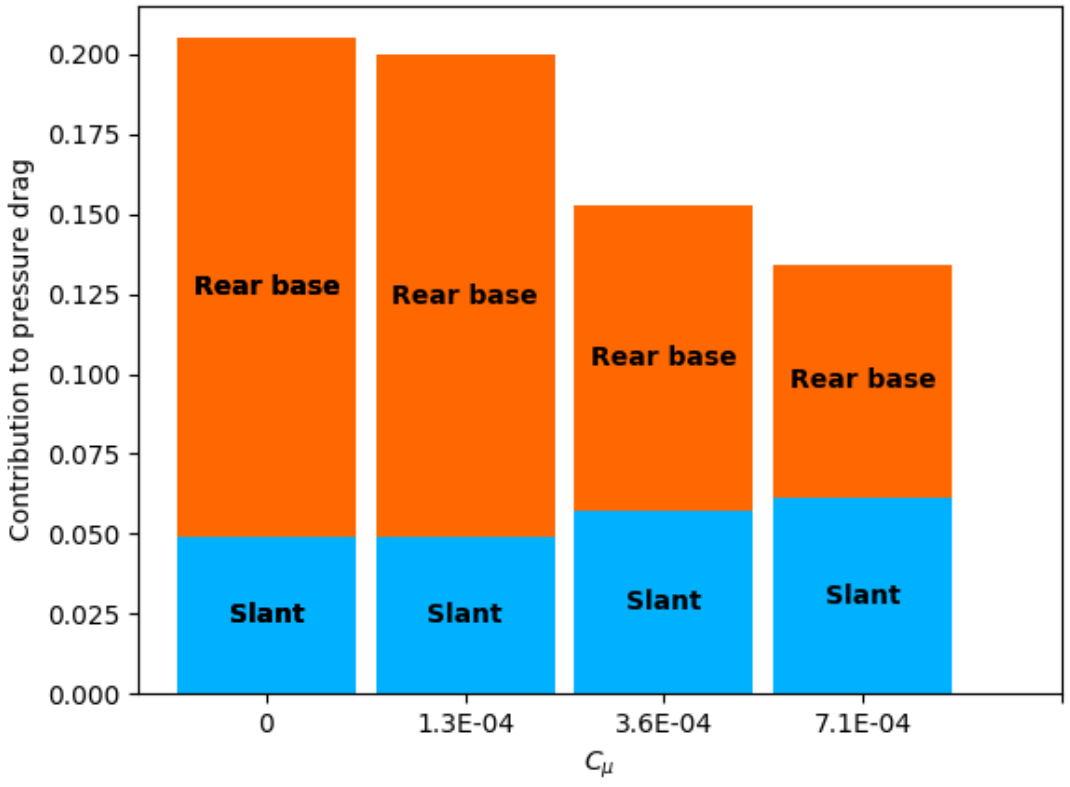

Figure 7.14: Contribution of the different parts of the body to the total drag as a function of the jet momentum coefficient for three relevant cases at $Re = 3750$ and $\tilde{f} = 1$

has been reduced. On the other hand the bottom surface pressure has been greatly increased as it is directly connected to the rear base pressure, which has also been greatly increased. This low pressure observed in the bottom region is usually known as ground effect. Therefore the conclusion of this section with regarding lift is that by increasing the base pressure the ground effect has been indirectly reduced. The average pressure fields confirm what was described in the instantaneous pressure fields.

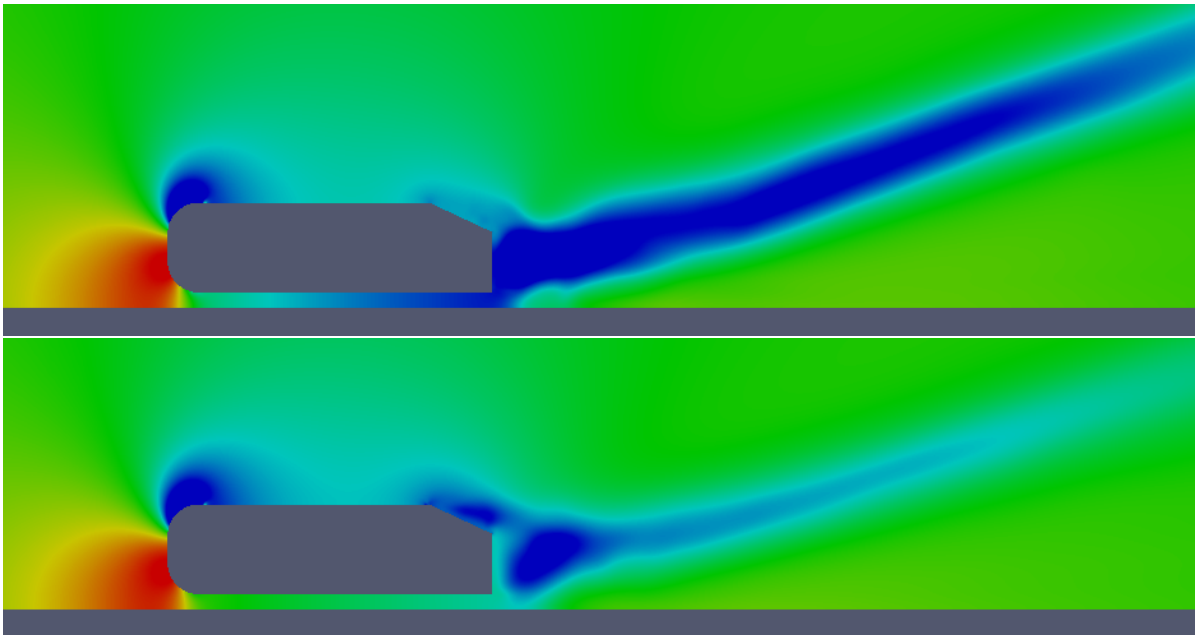

Figure 7.15: Qualitative comparison of the average pressure field for the baseline case (top) and a successfully actuated case (bottom) at $Re = 3750$ and $\tilde{f} = 1$ (dynamic ranges for C_P are set equal)

7.2.3. ACTUATION AT $\tilde{f} = 2$

Actuation at twice the natural vortex shedding frequency targets to excite the main instability of the flow. However instead of trying to resonate with it directly it tries to do so through the excitation of its first harmonic frequency. By introducing a perturbation right before the top shear layer, the goal is to change the way in which the top shear layer behaves. Actuation at this frequency is reported to be one of the most successful types of actuation at high Reynolds. This can be due to the fact that the active flow control resonates with the global instability of the flow, but in a more energetic way than simply actuating at the natural vortex shedding frequency. This type of actuation introduces one full perturbation every half cycle which is particularly interesting because the baseline case presents two clearly differentiated states: attached wake over the slant and separated wake over the slant. For this reason introducing one full perturbation during each flow state can have a large impact on the wake.

Actuation at twice the natural vortex shedding frequency is observed to produce 4 types of different solutions: 2 of which are periodic and the 2 other are chaotic. This frequency is observed to be the most interesting actuation frequency from both the qualitative point of view (two different stable states are observed) and the quantitative point of view (maximum drag reduction is obtained for low amplitudes, leading to maximum efficiency).

LOW ACTUATION AMPLITUDES ($C_\mu < 3.6 \times 10^{-4}$)

Differently to what occurs in the case of $\tilde{f} = 1$ the amplitude at which the flow responds to actuation is very low. Additionally, the response increases constantly with increasing C_μ. This is a completely different behavior to what was observed in the case of actuation at $\tilde{f} = 1$, where the average quantities abruptly shifted from one type of solution to the next when the periodic solution was observed. This behavior is similar to what has been observed experimentally at higher Reynolds. Qualitatively, the baseline solution destabilizes due to the AFC effect. This produces a series of chaotic solutions in which vortex shedding rapidly becomes affected by the blowing-suction actuation. Its effect on the flow fields is similar to what was observed in the case of $\tilde{f} = 1$

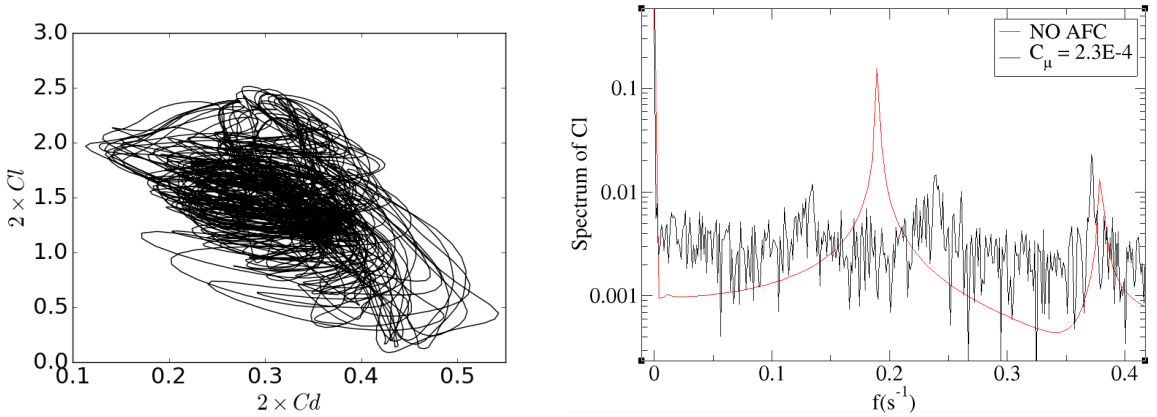

(a) Map of the aerodynamic forces

(b) Fourier transform of the lift coefficient

Figure 7.16: Analysis of the forces signal for $C_\mu = 2.3 \times 10^{-4}$ at $Re = 3750$ and $\tilde{f} = 2$

at high actuation amplitudes, and the vortex shedding of the top shear layer rapidly dominates the bottom shear layer.

In this section the chaotic behavior of the flow fields will not be described as depending on the actuation amplitude the flow resembles the baseline solution that was already described ($C_\mu < 1 \times 10^{-5}$) or it resembles the flow features of the solution for moderate amplitudes (which will be described in the following section). However, as an example the Cl-Cd map of the aerodynamic forces and the Fourier transform of the drag signal at $C_\mu = 2.3 \times 10^{-4}$ is shown in figure 7.16. An interesting effect of actuation at $\tilde{f} = 2$ is that the main vortex shedding frequency is increased and is now observed at $\tilde{f} \approx 1.2$ (see figure 7.16b). The second peak corresponds to the actuation frequency, which is approximately twice the original vortex shedding frequency and corresponds with the second peak of the baseline case in the Fourier transform diagram. It seems therefore that increasing the actuation frequency modifies the rear base vortex shedding phenomenon in such a way that it is accelerated. This will be further commented in the following sections.

MODERATE ACTUATION AMPLITUDES ($C_\mu = 3.6 \times 10^{-4}$)

For moderate actuation amplitudes a periodic solution with a period three times that of the actuation appears. This can be clearly observed in the Fourier transform diagram of the drag signal (figure 7.17b), which now presents three peaks of approximately the same energy. The top actuation completely controls the vortex shedding process as the top shear layer dominates the near wake over the bottom vortex. The result is that similarly to the case of $\tilde{f} = 1$ very little flow from the bottom region is introduced into the slant[2], and when this occurs it is shed into the flow in a short time interval, not allowing the rear vortex to grow as in the baseline case. Figure 7.18 shows the temporal evolution of the wake during one period. Close observation of the vorticity and pressure snapshots shows that during one period, three vortices of the top shear layer have been shed (one in frames 1 to 3, a second one in frames 4 to 7 and the last one in frames 8 to 12). During the same time period, however, only two have been shed from the bottom shear layer. This leads to a frequency locking of the solution of the type 2:3, and explains why the solution is periodic[3]. This indicates that now two phenomena are competing for the domination of the wake, at two different frequencies One period can be divided in three sub-periods that are clearly distinguishable according to the behavior of the top vortex: first the top vortex is shed directly into the wake, second the top vortex becomes trapped, and finally the vortex combines with the trapped vortex from the previous period. This is clearly distinguishable in the snapshots shown in figure 7.18. Snapshots 3 to 6 show the direct shedding of the vortex, 7 to 10 show how the vortex core becomes trapped, and 11 to 12 show how the two vortices combine. Regarding the bottom vortex it is interesting to note that the two vortices that are shed during one cycle are extremely different. One (frames 9-12) grows adjacent to the rear base (similarly to how it occurs in the baseline case) while the other one (frames 4-7) grows at a much greater distance. Both vortices are less energetic than those observed for the

[2] note that in figure 7.17 the top shear layer vortices are generated over the slant, not allowing the bottom ones to affect the slant region. Furthermore, the bottom vortices are now forced to shed faster by the influence of the top ones (see as an example frame 8). This clearly indicates that the top boundary layer dominates the wake dynamics.

[3] In the baseline case the vortices were frequency locked at a ratio of 1:1

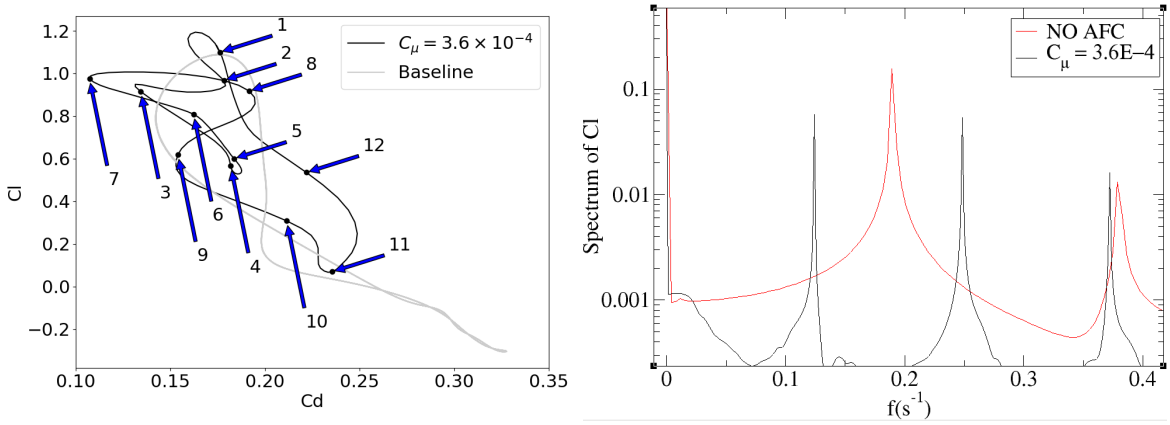

(a) Map of the aerodynamic forces

(b) Fourier transform of the lift coefficient

Figure 7.17: Analysis of the forces signal for $\tilde{f} = 2$ and $C_\mu = 3.6 \times 10^{-4}$ at $Re = 3750$

baseline case, explaining why drag is greatly reduced. However when the vortex is near the body the average drag is much larger that when it is further away from it. This is shown in figure 7.17a, which clearly shows that for snapshots 10 to 12 the drag of the vehicle is significantly larger than for snapshots 4 to 6. Furthermore it shows that the fast shedding of the bottom vortex has eliminated the highest drag section of the baseline case orbit, accounting for the large drag reduction.

The conclusion of the study of the flow fields is that (similarly to the case in which $\tilde{f} = 1$ and $C_\mu > 5 \times 10^{-4}$) forcing a dominating vortex on the top slant will reduce the rear base vortex, effectively moving the vortex generation towards the slant. This has the positive effect of greatly increasing the pressure on the rear base, but at the cost of moving the depression to the slant and increasing the underbody pressure, greatly increasing the average lift coefficient of the model. Furthermore drag reduction is not only achieved due to the reduction of the vortex intensity (and size), it is also achieved through the increase of the distance between the core and the body. This is consistent with what was described in section 1 as both vortex splitting and vortex pushing have been reported to produce significant drag reductions, however the increase in lift had not been reported, showing a limitation of the current model. The result is that average drag is reduced by approximately 30% with respect to the baseline case and that average lift is increased by approximately 400%.

It is interesting to note that changing the actuation frequency has had the effect of changing the synchronization of the vortices shed by the two shear layers, which now combine in such a way that the whole process repeats itself after three actuation periods. However, the vortex shedding frequency of the rear base has been altered and is now approximately $\tilde{f} = 4/3$. It seems therefore that the high actuation amplitude on the top shear layer precipitates the bottom vortex shedding. As explained for the case of smaller actuation amplitudes, if this state cannot be triggered (the actuation amplitude is not around 2.3×10^{-4}), the flow states tend to it. This seems to indicate that the stable solution behaves as an attractor for those cases in which periodic behavior cannot be obtained.

The conclusion of this section is that the vortex shedding process is now totally determined by the actuation on the top slant, which accelerates the rear base vortex shedding. When comparing with $\tilde{f} = 1$, it is worth mentioning that the momentum coefficient required to produce periodic solutions has been reduced. Furthermore in the case of $\tilde{f} = 1$ no impact on the global forces could be achieved in the case of periodic behavior, and only the high momentum coefficient actuations were observed to decrease drag. Therefore it is clear that forcing at twice the natural vortex shedding frequency is much more efficient than doing so at the natural vortex shedding frequency. Furthermore, the effect is gradual to the actuation momentum coefficient, which is considered desirable, as even if the desired amplitude is not achieved, a partial effect can still be obtained.

LARGE ACTUATION AMPLITUDES ($C_\mu = 1.4 \times 10^{-3}$)

When increasing the actuation amplitude, a series of new chaotic solutions is observed. The new solutions rapidly tend towards a new flow state which is periodic ($C_\mu = 1.4 \times 10^{-3}$). This periodic state recovers the natural actuation frequency of the baseline case and its period doubled solution. As in the previous case, the vortex shedding is under the control of the AFC, which forces the vortex shedding of the boundary layer to

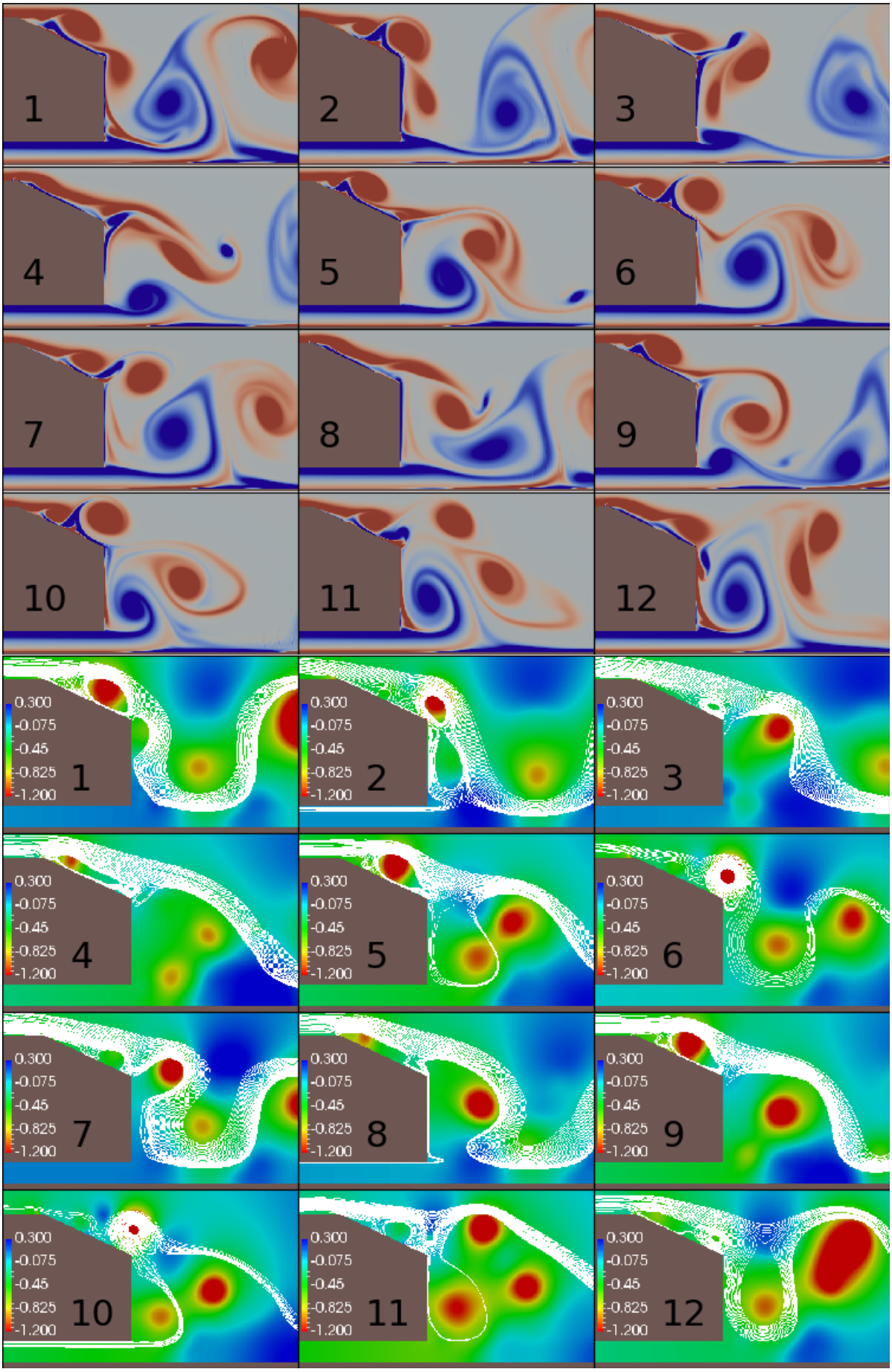

Figure 7.18: Wake temporal evolution for $\tilde{f} = 2$ and $C_\mu = 3.6 \times 10^{-4}$ at $Re = 3750$ (periodic), snapshots are equally separated in time

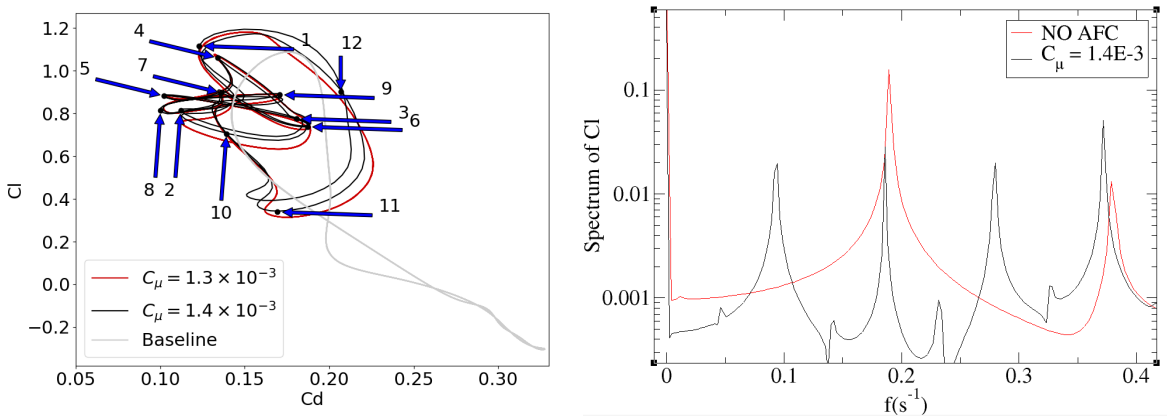

(a) Map of the aerodynamic forces

(b) Fourier transform of the lift coefficient

Figure 7.19: Analysis of the forces signal for $\tilde{f} = 2$ and $C_\mu = 1.4 \times 10^{-3}$ at $Re = 3750$

occur at the actuation frequency. The main difference is, again, how the two shear layer vortex shedding processes are synchronized: the frequency locking of the top and bottom shear layer shed vortices has changed to 3:4. In this case the flow of the wake is very similar to what was described in the previous successfully actuated cases. Similarly to what was observed for $C_\mu = 3.6 \times 10^{-4}$ and $\tilde{f} = 2$ the wake presents massive separation on the slant dominated by the AFC. It also features vortices that are shed directly into the wake and vortices that become trapped in the near wake. The difference is that now this occurs every four top shear layer vortices, and therefore there are two vortices that are directly shed into the wake, one that gets trapped, and one that combines with the trapped vortex when shed. Figure 7.19 shows the temporal evolution of this process: in frames 1 to 6 two top vortices are shed directly. Frames 7 to 9 show how that the top vortex is shed similarly to how it was before, but now the bottom shear layer vortex blocks its path. This allows for the vortex from the next period to reach it (frames 10-11), and they combine in frame 12.

Drag reduction as compared to the baseline case obtained in this case reaches approximately 40%, being clearly superior to the drag reduction of approximately 30% obtained at smaller actuation amplitudes. However the actuation amplitude has been increased from $C_\mu \approxeq 3.6 \times 10^{-4}$ to $C_\mu \approxeq 1.4 \times 10^{-3}$ which represents an increase of C_μ in a factor of approximately 3.5. Therefore, the efficiency of the flow control is decreased as the actuation amplitude is increased. This is consistent with what was explained in section 1 because it shows that drag reduction saturates with increasing actuation amplitude. The increase in lift coefficient is almost identical to that obtained for smaller actuation amplitudes. It is interesting to note that in this case the actuation frequency is the most energetic frequency in the flow. This was not observed for smaller amplitudes, where it was only the third most energetic peak of the drag spectra. This is due to the fact that now the vortex shedding frequency of the bottom shear layer is a subharmonic of the actuation frequency, so the actuation frequency is found in both shear layers. The Cl-Cd map presented in figure 7.19a shows a curve that has three branches of limited amplitude both in Cl and Cd, and a fourth branch that closes in a much wider fashion. This matches what was described in the flow fields, as also there three vortex shedding periods were described to be similar (represented in snapshots 1 to 10) while the last vortex shedding was found to be more energetic due to the combination of two vortices from successive periods (snapshots 10 to 12). This is relevant because this branch presents higher drag than the other branches, and points to the reason why the average drag is smaller than that of $C_\mu = 3.6 \times 10^{-4}$ and $\tilde{f} = 2$: Now only one vortex out of four combines, while before it was one out of three.

Figure 7.19a presents the Cl-Cd curves for both $C_\mu = 1.3 \times 10^{-3}$ and $C_\mu = 1.4 \times 10^{-3}$ to show the bifurcation scheme of the problem when C_μ is increased. In this case a period doubled solution is observed, pointing to a destabilization of the solutions by a period doubling cascade. This is similar to what was observed in the destabilization of the baseline solution, and seems to confirm that period doubling is the way in which the model destroys its stable solutions.

The summary of this section is that increasing the actuation amplitude forces the bottom vortex to shed its vortices faster, and a new synchronization of the wake is achieved of after every 4 actuation periods. The drag reduction and lift increase are greater than for smaller actuation amplitudes, but it seems that this effect is saturating, indicating that the efficiency of the flow control is smaller. Finally the destabilization of the orbit

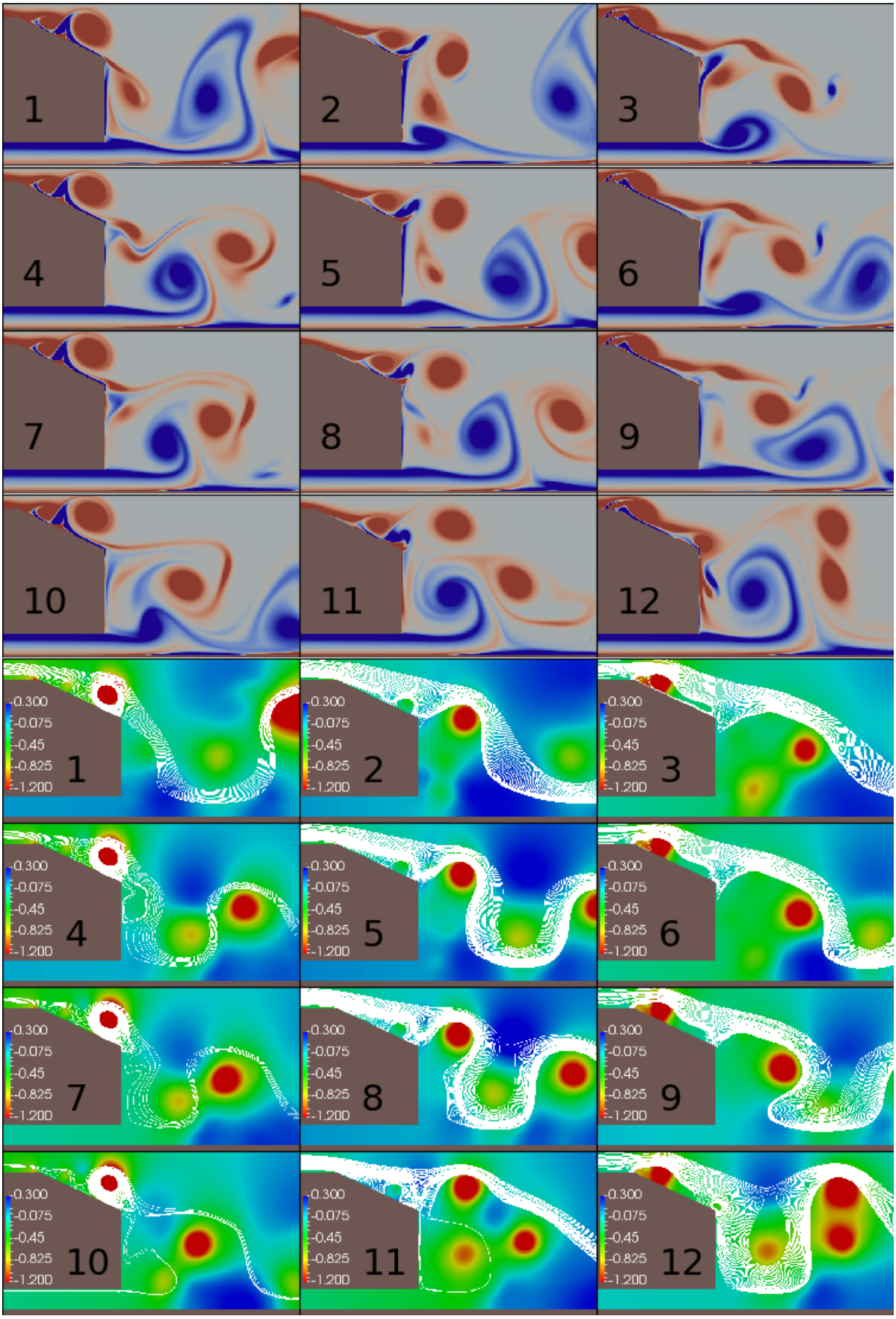

Figure 7.20: Wake temporal evolution for $\tilde{f} = 2$ and $C_\mu = 1.4 \times 10^{-3}$ at $Re = 3750$(periodic), snapshots are equally separated in time

has found to occur in a period doubling cascade bifurcation, which seems to be the most common way for the system to destroy stable orbits.

SUMMARY OF THE ACTUATION AT $f = 2 \times f_{Str}$

By actuating at twice the natural vortex shedding frequency on the rear slant the performance of the body has been greatly modified. The drag coefficient has been reduced by up to a 40% and the lift coefficient has increased by up to 400%. Increasing the actuation momentum coefficient has revealed that although the solutions are different qualitatively (some are chaotic, others periodic), the chaotic solutions seem to orbit around the underlying quasi-periodic solutions that eventually lock onto periodic. Two periodic frequency-locked solutions have been observed in the range study of C_μ. These solutions are only stable for small ranges of C_μ, and destabilize rapidly through what seem period doubling cascades. The chaotic states then start orbiting the next periodic solution, which is determined by the next frequency locking of the two shear layers. This is possible because increasing the actuation amplitude increases the vortex shedding frequency of the bottom vortex, which coexists with the one from top shear layer: if the actuation frequency[4] and the bottom base vortex shedding one are incommensurable, a chaotic solution is observed. However, for the particular cases in which they are not, a periodic behavior can be observed. In this case resonances of 2:3 and 3:4 of the vortex shedding of both shear layers are observed. This means that after three vortex shedding cycles of the top shear layer, two vortex shedding of the bottom shear layer have occurred and the solution repeats itself (similarly for 3:4). Note that this implies that for very low actuation amplitudes the bottom shear layer vortex shedding already occurs at $f > f_{Str}$. For moderate amplitudes occurs at $f \approx 2/3 \times f_{AFC}$. Finally for large amplitudes it occurs at $f \approx 3/4 \times f_{AFC}$. This clearly indicates that the bottom vortex shedding is being accelerated. A common fact of the periodic solutions is that after every period a large vortex is generated near the rear base which increases the average drag. This implies that those solutions that repeat after more cycles present a larger drag reduction than those that repeat more often. This justifies why a larger drag reduction is observed in the case of large actuation amplitudes, as the higher drag branch occurs every 4 cycles while for moderate amplitude it occurs every 3 cycles. An interesting feature of the Cd curve is that it presents peaks of larger drag for those actuation amplitudes that produce periodic solutions. It seems then that the synchronization of the two vortices is not a desirable feature, as very similar chaotic solutions produce lower drag. This seems to be related to the combination of the vortices in the near wake, as the chaotic solutions tend to produce less combined vortices than the periodic solutions.

Figure 7.21 presents the average Cl and Cd and the root mean square of the signals, compared to the baseline case. In the case of Cl, the RMS of the signal for successfully actuated cases is reduced between 60% and 70% of the non-actuated baseline case RMS. On the Cd signal this reduction represents between 50% and 55% of the baseline case RMS. This clearly indicates that the vortex shedding phenomenon has been substantially reduced. Similarly to what was explained in the previous section, the reason for this reduction is that flow actuation has greatly reduced the strength of the rear base vortices by exciting the slant shear layer. The additional energy introduced in the top shear layer is smaller than the decrease of energy of the rear base vortex, effectively reducing the oscillation amplitude of the global forces.

It is also particularly interesting to analyze which regions of the vehicle contribute most to drag in each case. Figure 7.22 shows a comparison of the drag contributions of the different types of solutions The results show that for the baseline case the rear base is the largest contributor to pressure drag (representing approximately 75% of the pressure drag). For moderate amplitudes the solution tends to the 2:3 resonance flow state, showing approximately the same drag for the slant region than for the rear base. Finally this tendency is shifted when the solution tends to the 3:4 resonance flow state showing a greater contribution to drag from the rear slant than from the rear base.

Figure 7.23 shows a comparison of the baseline case pressure distribution with a successfully actuated case. The base pressure has been greatly increased by generating a large depression on the rear slant that was not present in the baseline case. The high pressure of the rear base can be explained due to the fact that the vortex cores that are generated by the bottom vortex shedding are now being generated at a larger distance from the base, and are less energetic (smaller in size). The increase in the lift coefficient can be explained by two factors: on the one hand the slant average pressure has been reduced. On the other hand the underbody pressure has been greatly increased as it is directly connected to the rear base pressure, which has been greatly increased. The average pressure fields confirm what was described in the instantaneous pressure fields, and the result is similar to what was observed for $\tilde{f} = 1$, but now the required actuation momentum coefficient that is required is lower.

[4] Which coincides with the top shear layer vortex shedding

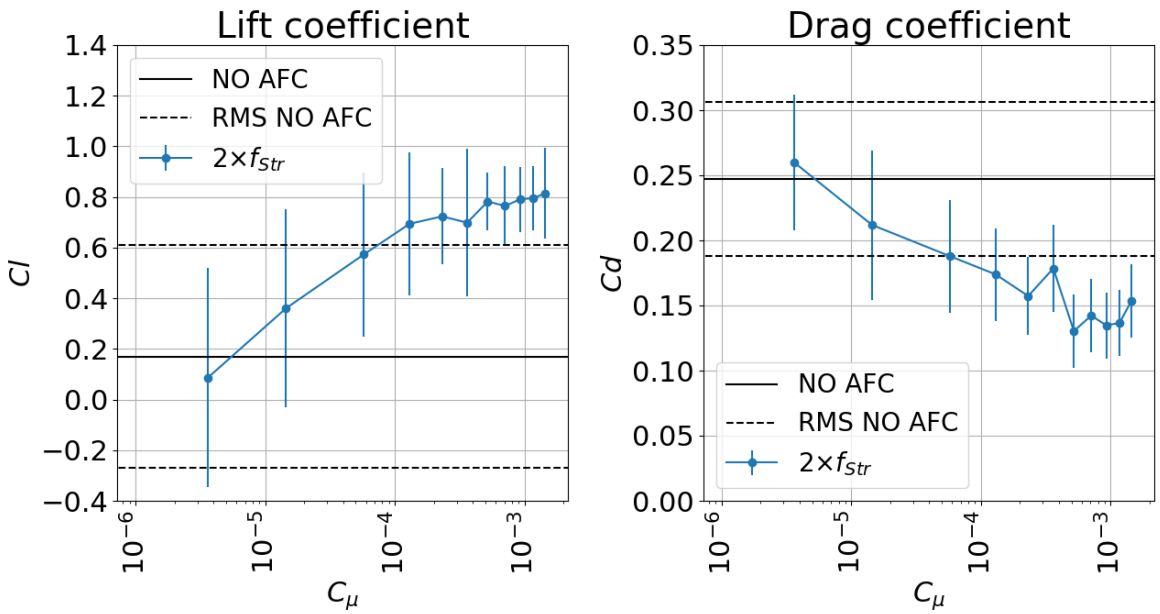

Figure 7.21: Lift and drag coefficients as a function of the jet momentum coefficient for $f = 2 \times f_{Str}$ at $Re = 3750$, the error bars represent the RMS of the signal

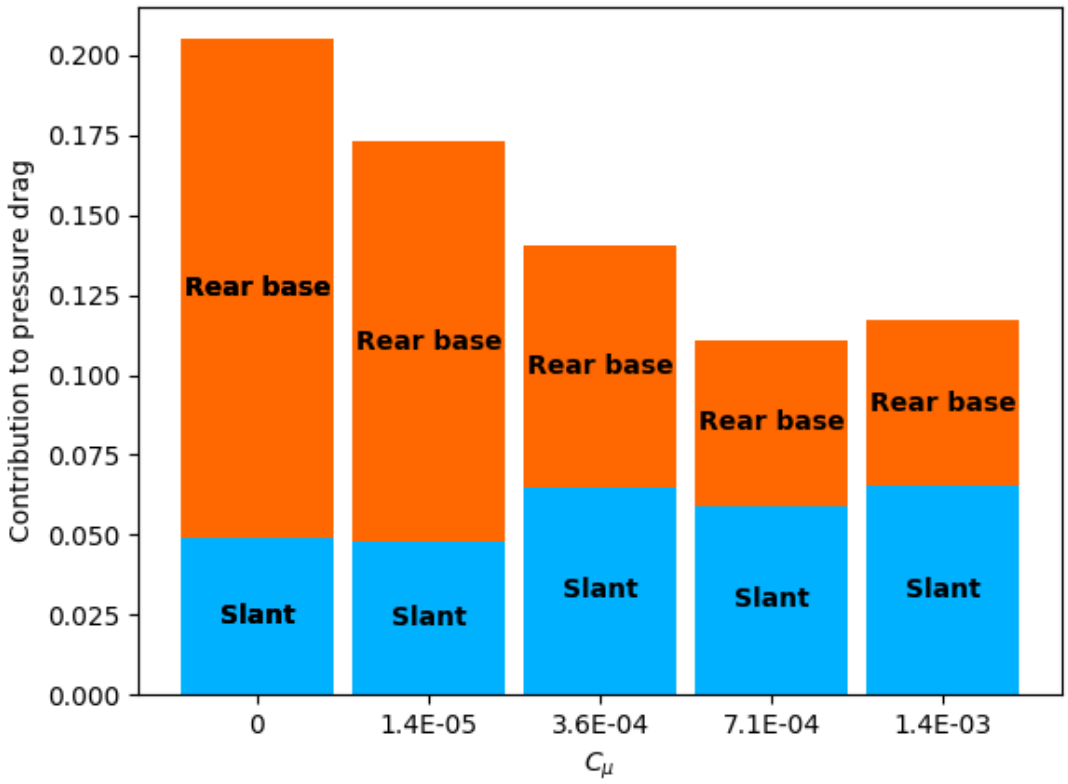

Figure 7.22: Contribution of the different parts of the body to the total drag as a function of the jet momentum coefficient at $Re = 3750$ and $\tilde{f} = 2$

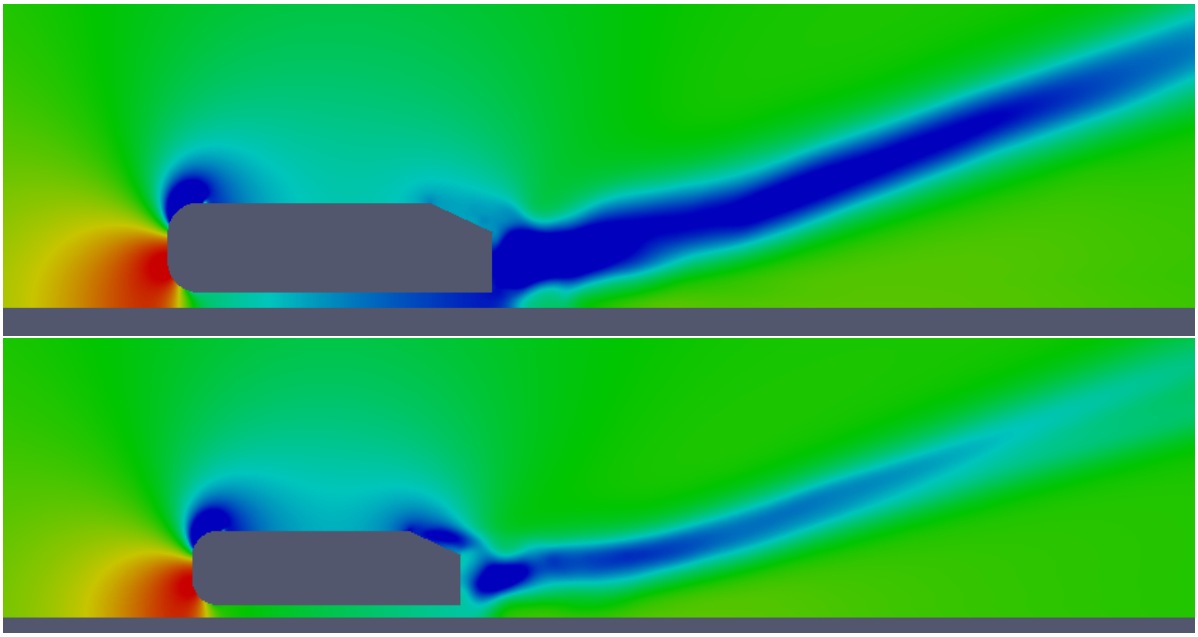

Figure 7.23: Qualitative comparison of the average pressure field for the baseline case (top) and a successfully actuated case (bottom) at $Re = 3750$ and $\tilde{f} = 2$ (dynamic ranges for C_P are set equal)

7.2.4. CONSTANT SUCTION

Several simulations were performed using a constant suction with the goal of comparing the results presented in this chapter. Constant suction is usually applied to suppress the separation of the boundary layer at the slant region, but presents the inconvenience of requiring a constant mass flux, which implies that in a real case it should be expelled elsewhere. However in a numerical simulation this is not required, and for this reason it is very simple to implement. Constant suction is interesting because by partially suppressing the separation region the wake dimensions are greatly reduced, and therefore the intensity of its vortices.

Differently from what is observed in the case of periodic actuation, the effect of constant suction does not change the stability of the periodic solution: independently of the actuation amplitude, a periodic solution is observed. This is presented in figure 7.24a. However, the effect of constant suction is observed as a change in the natural vortex shedding frequency, which is increased with increasing suction amplitudes. This effect is presented in figure 7.24b, where the Fourier transform of different actuation amplitudes is shown. At maximum actuation amplitude the change in natural frequency reaches approximately 50%. The Cl-Cd curve (figure 7.24a) shows two important trends: on the one hand drag is substantially reduced and lift increased;

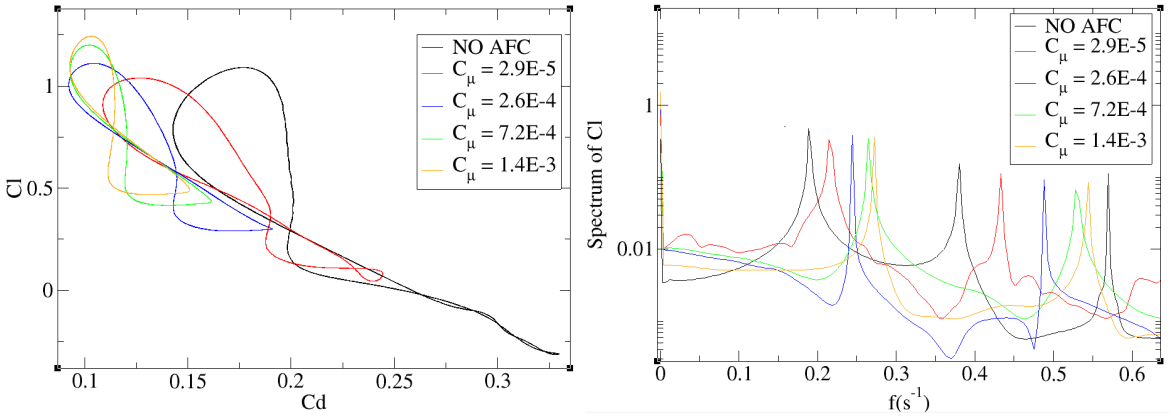

(a) Map of the aerodynamic forces

(b) Fourier transform of the lift coefficient

Figure 7.24: Analysis of the forces signal for $Re = 3750$

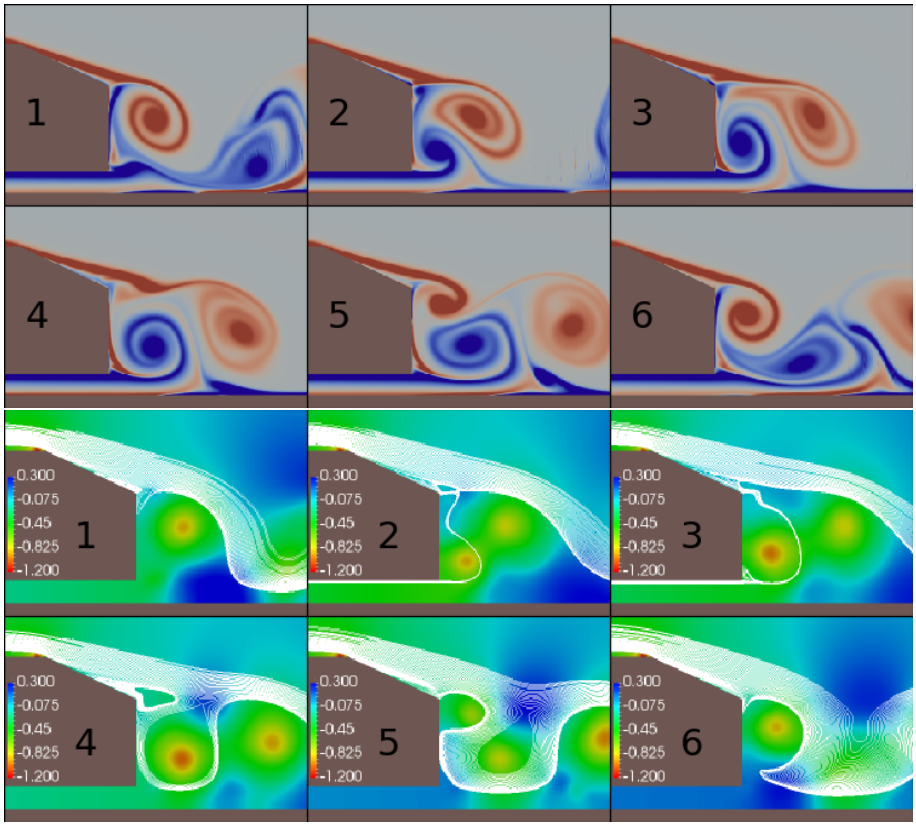

Figure 7.25: Wake temporal evolution for constant actuation for $Re = 3750$ and $C_\mu = 7.2 \times 10^{-4}$ (periodic), snapshots are equally separated in time

on the other hand, the amplitude of the curves is substantially reduced. This clearly indicates that the vortex shedding intensity has been reduced.

The analysis of the flow fields further confirm what has been described. Figure 7.25 shows one full period for $C_\mu = 7.2 \times 10^{-4}$. In this case the flow over the slant does not separate at the start of the slant. The separation point moves periodically along the slant, switching between totally attached flow (frame 6) and almost fully separated flow (frame 3). This is substantially different from the baseline case, where fully attached flow was not observed. The separated flow region over the slant has been reduced to a size that does not allow the rear base vortex to grow. Therefore the vortex reaches its maximum size faster, and is shed faster, leading to a higher bottom base natural frequency. This is consistent with the attached low drag scenario described in chapter 1, and, as expected produces larger drag reductions than the separated low drag scenarios triggered by the periodic actuations described in the previous sections.

7.3. CONCLUSIONS

The main conclusion of this section is that periodic actuation is successful in reducing the drag of the Ahmed body in the transitional regime. Additionally, it can also generate new types of periodic solutions, which appear in the form of frequency lockings of the top and bottom vortex generation processes. These solutions are destroyed through the advent of period doubling bifurcations. The main reason for drag reduction was found to be the acceleration of the rear base vortex shedding process by preventing it from growing in the slant region. The baseline case featured a flow field with the characteristics of the high drag scenario described in chapter 1. In this scenario the drag was high due to the flapping motion of the shear layer which presented both partial reattachment and fully separated wake over the slant. This was generating a time evolution in which large vortices were generated on the rear base which were interacting with the top shear layer and generating a large depression adjacent to the rear base. By introducing periodic perturbations into the top shear layer, however, it is possible to dominate the bottom vortex shedding process, and to reduce its effects and intensity. This is achieved by breaking the top shear layer and forcing it to generate vortices over the slant. Upon reaching the rear base these vortices reduce the space available for the rear base vortex to grow, and

greatly reduce the amount of flow that travels from the rear base to the slant region. This implies that the rear base vortex intensity is greatly reduced, generates at a greater distance from the rear base and is shed faster. This, however, comes at the cost of generating large vortices over the slant, and produces an unexpected effect: it greatly increases the pressure on the underbody of the vehicle (significantly reducing the ground effect present in the baseline case). The result of all these changes is that drag can be reduced up to 40% at the cost of increasing the lift of the body up to 400%.

The frequency of the periodic actuation is found to be the most relevant parameter in terms of efficiency of actuation. Figure 7.26 shows a comparison of all the cases that were studied with the constant blowing actuation, both in terms of drag and lift. The results show that actuation at frequencies that are lower than the natural vortex shedding frequency allow for smaller reductions in drag as the flow has enough time to destabilize on its own. For this reason no new types of solutions other than chaotic states (that resemble the baseline case) could be found, independently of the actuation amplitude, for $\tilde{f} = 1/2$. This was not achieved even at an actuation frequency which is naturally unstable for the problem and which had been selected precisely for this reason. The results show that for large amplitudes the drag coefficient can be reduced up to 20% using this type of actuation, however the drag reduction is not accompanied by a reduction in the intensity of the vortex shedding phenomena.

Actuation at the natural vortex shedding frequency proved to be more effective as it can alter significantly the type of solutions that can be obtained and the vortex shedding intensity. This type of actuation proved to be effective only when the amplitude exceeded the threshold of $C_\mu > 5 \times 10^{-4}$. Above this value the drag coefficient is reduced by between 30% and 40%, showing a behavior that could be described as on-off. Drag reduction is obtained by forcing the top shear layer to destabilize over the slant, instead of doing so adjacent to the rear base. The result is that the rear base vortex is shed faster and pushed away, increasing the base pressure, and therefore decreasing drag. The conclusion of this type of actuation is that when aiming to reduce the drag of the model, this can be obtained by preventing the rear base vortex from dominating the wake.

Actuation at $\tilde{f} = 2$ proved to be the most effective method to control the wake. First of all it is the type of actuation for which the largest drag reduction was obtained, and significant drag reductions can be obtained with relatively low momentum coefficients (compared to the other actuation frequencies). In this case at low actuation amplitudes the flow is already receptive to the perturbations, showing a reduction that increases C_μ. However as C_μ is increased the effect saturates, and for $C_\mu > 10^{-3}$ no further gain can be observed. Secondly, this type of actuation produced two different types of periodic solutions, allowing to determine how the control over the rear base vortex shedding is exerted. From the results it was concluded that the actuation at a higher frequency is accelerating the vortex shedding of the bottom shear layer. Since the two vortices are not shed at the same frequency, the solution is a complex combination of the two. However, in some cases the two frequencies are commensurable, leading to the two periodic solutions that have been presented. This is possibly the most interesting effect that is observed, as in general, when describing the effect of flow control on the wake, the focus is put on the study of the slant region. For this reason changes to the rear base vortex frequency were not found in literature. The results of this work, however, indicate that changes to the rear base vortex are the key to understanding the active flow control drag reductions.

Possibly the most interesting effect of the successful application of active flow control is that in all cases the bottom base vortex shedding frequency has been increased. This seems to indicate that drag reduction could be linked to this effect directly. This is confirmed both for periodic excitation and constant suction and explains why low frequency actuations have been unsuccessful. It also explains why $\tilde{f} = 2$ actuations produce almost the same effect as constant suction: the relevant parameter in determining the average forces seems to be the base vortex shedding frequency, and not the slant wake topology.

Finally, the study of the different types of solutions also confirmed that period doubling bifurcations are the natural mechanism by which the problem creates and destroys periodic solutions. This confirms what was observed in the study of the baseline case, as both by varying the Reynolds number (in the baseline case) and by varying the momentum coefficient (in the actuated case), period doubling cascades have been found to be the destabilization mechanism of the periodic solutions.

7.3.1. FLOW SIMILARITIES TO HIGHER REYNOLDS CASES

As explained in the introduction of this thesis, the study of AFC has been mostly centered in the turbulent regime. However, some similarities are observed, which can be interesting to discuss briefly. Comparison of the results to higher Reynolds 3D cases is difficult as two main obvious differences exist: Reynolds and three-dimensionality. For the baseline case the vortex shedding frequency was found to be very similar to

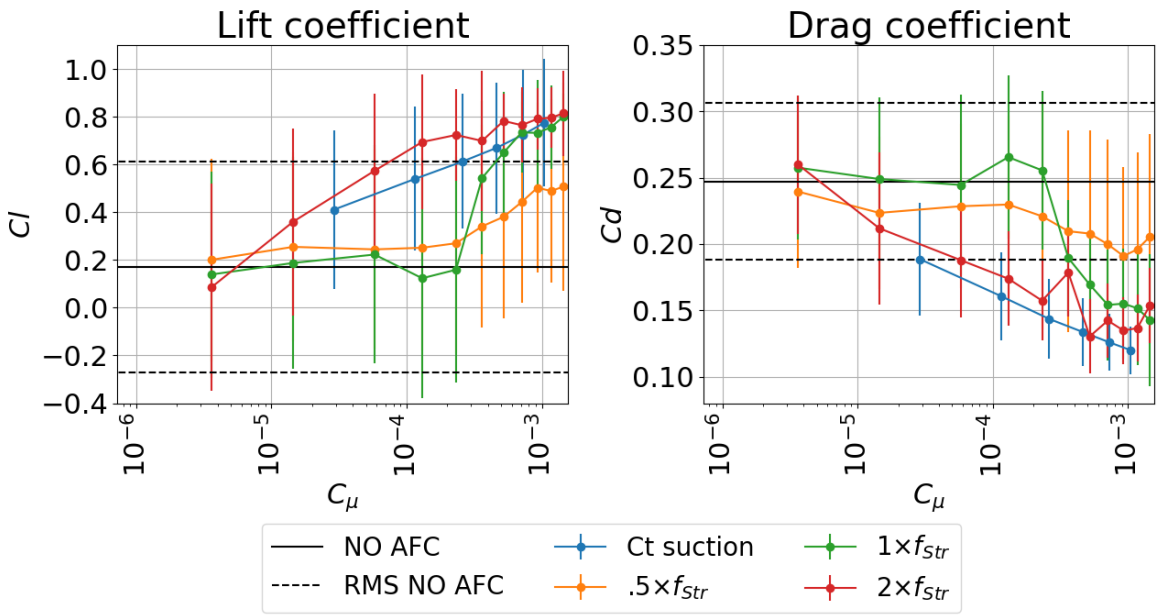

Figure 7.26: Lift and drag coefficients as a function of the jet momentum coefficient $\tilde{f} = 1/2$, $\tilde{f} = 1$ and $\tilde{f} = 2$ at $Re = 3750$, the error bars represent the RMS of the signal

3D slanted Ahmed body cases which feature no c-pillar vortices or square Ahmed body geometries. The accuracy is however lower when comparing to the fully 3D slanted geometry. in the case of active flow control it is interesting to mention that most of the results that were observed in the study of the transitional regime were found to match the trends of what was described in literature quite accurately in the case of drag. First of all, actuation at the natural vortex shedding and higher frequencies was found to be more effective than actuation at lower frequencies. Second, the drag mechanisms observed in this work coincide with what was described in literature: the baseline case was found to present a high drag flow field with partial reattachment and moderate separation. The actuated cases, however presented the attached low drag (ALD) scenario in the case of constant suction, and separated low drag (SLD) in the case of periodic excitation.

With respect to the total drag reduction it is worth mentioning that the drag reduction obtained is larger than those observed in literature for 3D cases and higher Reynolds. This could be anticipated as two factors are expected to produce this effect: on the one hand, as explained in section 1, for normal aspect ratios 2D flow is observed in approximately 80% of the slant. Therefore the results are not valid in the remaining %. Second, the effect of the c-pillar vortices consists in reducing the separation angle of the wake, and therefore the 2D baseline drag is probably larger than in an equivalent 3D case.

Finally, the results are not matching what was described in literature with respect to lift. As explained, the changes in rear base pressure have produced an increase in the under-body pressure that is responsible for a dramatic increase in lift. This was not described in literature, and can be related to the differences in Reynolds. Possibly, as the flow has less inertia, the impact of the wake low pressure is larger in the transitional regime than at higher Reynolds. Additionally the 2D constraint can have a large impact on the underbody pressure as in the 3D case flow can travel from the sides and reduce this depression. Overall, taking into account the limitations of the present simulations, the results show a reasonable agreement with the real main flow features.

8

CONCLUSIONS AND RECOMMENDATIONS

8.1. CONCLUSIONS

The goal of this work was to study the transitional regime of the 2D Ahmed body and to determine the effect of active flow control on the rear slant in this regime using Direct Numerical Simulation. In part 1, the study of the Ahmed body model was performed, and although it presented many interesting flow features, it did not share similar features with the Ahmed body flow at higher Reynolds. The different types of solutions are, however, very interesting from the stability analysis point of view. Periodic, quasi-periodic, period doubled and chaotic solutions were observed. Unfortunately the differences in flow features are too large to apply the same type of actuation directly in the transitional regime directly. The main difference that is observed is that flow separation takes place at the front region of the body, while at higher Reynolds it is observed at the beginning of the slant. The solution consisted in suppressing the point of separation by the use of constant suction at the front region of the roof, while keeping all other parameters constant. This way the boundary layer is forced to restart, generating a flow that shares a very good resemblance with the higher Reynolds number flow. The separation of the boundary layer is therefore moved to the slant region, where vortex shedding is observed. The new transitional regime occurs for this model at higher Reynolds, and only a period doubling bifurcation can be observed. This led to the conclusion that a period doubling cascade is the natural destabilization mechanism by which ordered solutions transition to chaotic behavior. Additionally the period doubled solutions present very similar lift and drag characteristics, so no clearly differentiable flow states were found in terms of drag and lift. The baseline case flow, however, was shown to present a high drag wake topology, making it interesting from the point of view of drag reduction.

The last part of this work consisted in the introduction of periodic actuation near the separation point of the top boundary layer. Different frequency and amplitude actuations were used, and the changes in the stability of the solutions were observed. The goal of this section was to determine whether the new types of solutions were interesting from the point of view of improving the performance of the body. The first actuation strategy was defined from the natural destabilization of the periodic vortex shedding solution. The philosophy behind this type of actuation consists in considering that perhaps resonance at this frequency could be achieved, creating new types of solutions. Unfortunately this hypothesis was proven incorrect, as the flow failed to resonate. Secondly, the natural vortex shedding frequency of the wake was tested. This was an obvious choice from the stability point of view (it is the most unstable mode of the flow), and had also been reported to produce a reduction in the global forces in literature. The results of this actuation showed that for $C_m u > 5 \times 10^{-4}$ the actuation on the shear layer is successful and the dynamics of the wake are dominated by the top shear layer destabilization imposed by the AFC. This generates chaotic solutions but also a new periodic solution. This new periodic solution does not show relevant changes in the global forces but shows the mechanism by which control of over the wake could be obtained: the breakup of the slant shear layer over the slant. Once the actuation control threshold is overcome, large drag reductions are achieved, reaching up to 40% of the baseline drag. For all successful actuations the frequency of the rear base vortices is increased by preventing it from growing into the slant region. This reduces the intensity of the shed vortices and pushes them away. This also greatly increases lift, an unexpected and probably unwanted effect.

Finally, actuation at twice the natural vortex shedding frequency was tested. This choice was also determined from literature, as it had been found to produce large drag reductions at high Reynolds. This actuation

frequency was found to be the most interesting case for two reasons. On the one hand, drag reductions equivalent to those observed for lower frequencies can be achieved for smaller actuation amplitudes. On the other hand, two new periodic solutions were observed, which are a consequence of the frequency locking of the top and bottom vortices. Actuation was found to force the vortex shedding frequency of the top shear layer directly, but also the bottom shear layer frequency indirectly. However, as the top shear layer vortex frequency remains fixed, the one from the bottom shear layer increases with increasing actuation amplitudes. The flow changes responsible for drag reduction were not observed to be significantly different from those described in the case of actuation at the natural vortex shedding frequency. However, the instabilities introduced by the AFC are clearly more efficient.

The comparison of these actuations with constant suction also showed that vortex shedding on the rear base occurs at a higher frequency as the flow separation is suppressed. The results presented in this work showed that although the wake topology is different, periodic actuation and constant suction present similar drag reductions and changes to the vortex shedding frequency. This further supports the idea that the vortex shedding frequency of the rear base is a key parameter in the drag of the model, independently of the wake topology.

The overall conclusions of this work are that by applying AFC new types of periodic solutions can be obtained in the transitional regime. These solutions are generated by frequency lockings of the vortex shedding phenomena and destroyed by period doubling cascades, which were found to be the natural destabilization mechanism of the problem. However these solutions cannot be obtained efficiently by triggering the natural instabilities of the problem, instead, artificial actuations of higher frequency should be used. In this way the vortex shedding process is accelerated, and drag is reduced. The new types of flow solutions were found to be very interesting from the point of view of drag reduction, however, they are accompanied by large lift increments, which are not desirable in general. Periodic solutions were also observed to be very delicate, as only very particular amplitudes at a certain frequency can maintain the periodic behavior in time. However, this is not important because the chaotic solutions are attracted by the underlying periodic orbits, and present similar average forces in wide range of actuation amplitudes. In fact, the periodic orbits were found to be more energetic and present slightly higher average forces. For this reason the actuated chaotic solutions present the most interesting characteristics in terms of drag, lift and vortex shedding intensity reductions, leading to maximum control efficiency. This efficiency is comparable (in the case of $\tilde{f} = 2$) to that of constant suction, and does not require a constant mass flow, presenting a large potential.

8.2. RECOMMENDATIONS AND FURTHER WORK

The most obvious limitation of the current model is that the simulations that have been performed are 2D. This has allowed to test the parameter space thoroughly, however it obviously introduces a large limitation on the validity of the results. For this reason, performing this study in a 3D model can potentially bring more relevant results, validating or contradicting what has been described in the present study. This however will require a large computational capacity, and possibly more time than the duration of this thesis.

A second interesting area of research is the application of actuation frequencies that are at least one order of magnitude larger than the vortex shedding frequency. In this work the application of active flow control at frequencies of the order of the natural vortex shedding was judged the most interesting area of study from the point of view of stability analysis. However it is not the only range of frequencies in which active flow control has been found to produce important drag reductions. Furthermore, the results show that high frequency vortex shedding is a desirable feature of the flow field in terms of resonating with the flow. For this reason, actuation at $\tilde{f} \approx 10$ can be proposed as interesting future work that can be performed on the proposed model.

Another interesting area of research can be to reproduce the current model at higher Reynolds numbers ($Re \approx 10^6$). This can be performed using RANS and turbulence models. This way, the similarities and differences in the flow features and the effect of the AFC can be assessed, allowing to better establish to which extent the study of the transitional regime can provide useful information in the study of AFC.

An additional interesting topic that can be proposed is the study of the implementation of active flow control on the rear base region. This approach has received much less interest in literature, and it has been mostly studied in the context of constant actuation. The bottom shear layer vortex was found to be the most relevant flow feature from the point of view of the global forces. Flow control on the top shear layer modified the bottom vortex shedding process indirectly, leading to large drag reductions. Therefore it can be interesting to directly actuate on the rear base flow, as it can potentially have a larger impact on the global forces.

BIBLIOGRAPHY

[1] I. Hucho, *Aerodynamics of Road Vehicles,* Annual Review of Fluid Mechanics **25**, 485 (1993).

[2] J. Venning, D. Lo Jacono, D. Burton, M. Thompson, and J. Sheridan, *The effect of aspect ratio on the wake of the Ahmed body,* Experiments in Fluids **56**, 1 (2015).

[3] S. R. Ahmed, *Influence of Base Slant on the Wake Structure and Drag of Road Vehicles,* Journal of Fluids Engineering **105**, 429 (1983).

[4] H. Lienhart, C. Stoots, and S. Becker, *Flow and Turbulence Structures in the Wake of a Simplified Car Model (Ahmed Modell),* in *New Results in Numerical and Experimental Fluid Mechanics III* (Springer Berlin Heidelberg, Berlin, Heidelberg, 2002) pp. 323–330.

[5] M. Pastoor, L. Henning, B. R. Noack, R. King, and G. Tadmor, *Feedback shear layer control for bluff body drag reduction,* Journal of Fluid Mechanics **608**, 161 (2008).

[6] G. Pujals, S. Depardon, and C. Cossu, *Drag reduction of a 3D bluff body using coherent streamwise streaks,* Experiments in Fluids **49**, 1085 (2010), arXiv:1301.7580 .

[7] S. Aubrun, J. McNally, F. Alvi, and A. Kourta, *Separation flow control on a generic ground vehicle using steady microjet arrays,* Experiments in Fluids **51**, 1177 (2011).

[8] N. Tounsi, R. Mestiri, L. Keirsbulck, H. Oualli, S. Hanchi, and F. Aloui, *Experimental Study of Flow Control on Bluff Body using Piezoelectric Actuators,* **9**, 827 (2016).

[9] D. L. Barsotti, E. A. Divo, and S. K. S. Boetcher, *Optimizing Jets for Active Control of Wake Refinement for Ground Vehicles,* Journal of Fluids Engineering **137**, 121108 (2015).

[10] J.-L. Aider, J.-F. Beaudoin, and J. E. Wesfreid, *Drag and lift reduction of a 3D bluff-body using active vortex generators,* Experiments in Fluids **48**, 771 (2010).

[11] J. F. Beaudoin and J. L. Aider, *Drag and lift reduction of a 3D bluff body using flaps,* Experiments in Fluids **44**, 491 (2008).

[12] A. Kourta and C. Leclerc, *Characterization of synthetic jet actuation with application to Ahmed body wake,* Sensors and Actuators, A: Physical **192**, 13 (2013).

[13] C.-H. Bruneau, E. Creusé, D. Depeyras, P. Gilliéron, and I. Mortazavi, *Active and passive flow control around simplified ground vehicles,* Journal of Applied Fluid Mechanics **5**, 89 (2012).

[14] P. Joseph, X. Amandolese, C. Edouard, and J. L. Aider, *Flow control using MEMS pulsed micro-jets on the Ahmed body,* Experiments in Fluids **54** (2013), 10.1007/s00348-012-1442-x.

[15] J. Meiss, *Dynamical systems,* Scholarpedia **2**, 1629 (2007).

[16] S. H. Strogatz, *Nonlinear Dynamics and Chaos: With Applications to Physics, Biology, Chemistry, and Engineering,* (1995).

[17] J. Guckenheimer, *Bifurcation,* Scholarpedia **2**, 1517 (2007).

[18] D. Ruelle and F. Takens, *On the nature of turbulence,* Communications in Mathematical Physics **20**, 167 (1971).

[19] S. Newhouse, D. Ruelle, and F. Takens, *Communications in Mathematical Physics*, Vol. 64 (Springer-Verlag Heidelberg, 1978) pp. 35–40.

[20] S. Wiggins, F. John, J. Marsden, L. Sirovich, M. Golubitsky, and W. J. Äger, *Texts in Applied Matehmatics* (1990) arXiv:arXiv:1011.1669v3 .

[21] R. M. May, *Simple mathematical models with very complicated dynamics,* Nature **261**, 459 (1976).

[22] R. Natarajan and A. Acrivos ', *The instability of the steady flow past spheres and disks,* J . Fluid Mech **254**, 323 (1993).

[23] D. Fabre, F. Auguste, and J. Magnaudet, *Bifurcations and symmetry breaking in the wake of axisymmetric bodies,* Physics of Fluids **20**, 051702 (2008).

[24] P. Meliga, J.-M. Chomaz, and D. Sipp, *Global mode interaction and pattern selection in the wake of a disk: a weakly nonlinear expansion,* Journal of Fluid Mechanics **633**, 159 (2009).

[25] Y. Bury and T. Jardin, *Transitions to chaos in the wake of an axisymmetric bluff body,* (2012).

[26] G. Rigas, A. S. Morgans, and J. F. Morrison, *Weakly nonlinear modelling of a forced turbulent axisymmetric wake,* Journal of Fluid Mechanics **814**, 570 (2017).

[27] P. Bohorquez, E. Sanmiguel-Rojas, A. Sevilla, J. I. Jiménez-González, and C. Martínez-Bazán, *Stability and dynamics of the laminar wake past a slender blunt-based axisymmetric body,* Journal of Fluid Mechanics **676**, 110 (2011).

[28] G. Rigas, A. Oxlade, A. Morgans, and J. Morrison, *Low-dimensional dynamics of a turbulent axisymmetric wake,* Journal of Fluid Mechanics **755**, R5 (2014).

[29] M. Grandemange, O. Cadot, and M. Gohlke, *Reflectional symmetry breaking of the separated flow over three-dimensional bluff bodies,* Physical Review E - Statistical, Nonlinear, and Soft Matter Physics **86**, 1 (2012).

[30] R. Li, D. Barros, J. Borée, O. Cadot, B. R. Noack, and L. Cordier, *Feedback control of bimodal wake dynamics,* Experiments in Fluids **57**, 1 (2016).

[31] R. Volpe, P. Devinant, and A. Kourta, *Experimental characterization of the unsteady natural wake of the full-scale square back Ahmed body: flow bi-stability and spectral analysis,* Experiments in Fluids **56**, 99 (2015).

[32] C.-H. Bruneau, E. Creusé, P. Gilliéron, and I. Mortazavi, *Effect of the vortex dynamics on the drag coefficient of a square back Ahmed body: Application to the flow control,* European Journal of Mechanics - B/Fluids **45**, 1 (2014).

[33] D. J. Parkin, M. C. Thompson, and J. Sheridan, *Numerical analysis of bluff body wakes under periodic open-loop control,* Journal of Fluid Mechanics **739**, 94 (2014).

[34] L. Henning, M. Pastoor, R. King, B. R. Noack, and G. Tadmor, *Feedback Control Applied to the Bluff Body Wake,* Active Flow Control, NNFM , 369 (2007).

[35] T. Tunay, B. Sahin, and V. Ozbolat, *Effects of rear slant angles on the flow characteristics of Ahmed body,* Experimental Thermal and Fluid Science **57**, 165 (2014).

[36] M. Grandemange, M. Gohlke, and O. Cadot, *Turbulent wake past a three-dimensional blunt body. Part 1. Global modes and bi-stability,* Journal of Fluid Mechanics **722**, 51 (2013).

[37] M. Grandemange, M. Gohlke, and O. Cadot, *Bi-stability in the turbulent wake past parallelepiped bodies with various aspect ratios and wall effects,* Physics of Fluids **25**, 095103 (2013).

[38] M. Grandemange, O. Cadot, A. Courbois, V. Herbert, D. Ricot, T. Ruiz, and R. Vigneron, *A study of wake effects on the drag of Ahmed's squareback model at the industrial scale,* Journal of Wind Engineering and Industrial Aerodynamics **145**, 282 (2015).

[39] E. G. Duell and A. R. George, *Experimental Study of a Ground Vehicle Body Unsteady Near Wake,* (Society of Automobile Engineers, 1999).

[40] E. Varon, Y. Eulalie, S. Edwige, P. Gilotte, and J.-L. Aider, *Chaotic dynamics of large-scale structures in a turbulent wake,* Physical Review Fluids **2**, 034604 (2017).

[41] E. N. Lorenz, *Deterministic Nonperiodic Flow,* (1963).

[42] V. Gentile, F. F. J. Schrijer, B. W. Van Oudheusden, and F. Scarano, *Low-frequency behavior of the turbulent axisymmetric near-wake,* Physics of Fluids **28** (2016), 10.1063/1.4953150.

[43] A. Thacker, S. Aubrun, A. Leroy, and P. Devinant, *Experimental characterization of flow unsteadiness in the centerline plane of an Ahmed body rear slant,* Experiments in Fluids **54** (2013), 10.1007/s00348-013-1479-5.

[44] S. Dong, *A convective-like energy-stable open boundary condition for simulations of incompressible flows,* Journal of Computational Physics **302**, 300 (2015), arXiv:arXiv:1506.01320v1 .